N° d'ordre NNT: 2021LYSEC22

THÈSE de DOCTORAT DE L'ECOLE CENTRALE DE LYON
membre de l'universitè de Lyon

École Doctorale N° 160
Electronique Electrotechnique Automatique

Spécialité/discipline de doctorat :
Electronique, Micro et Nanoélectronique, Optique et Laser

Soutenue publiquement le 25/06/2021, par :

Eirini Sarelli

Nanophotonic structures for controlling the emission of nano-phosphors for LED applications

Devant le jury composé de :

Fabrice Gourbilleau	*Directeur de recherche CNRS, ENSICAEN, CIMAP*	Rapporteur
Juan Martinez Pastor	*Professeur, Universitat de València*	Rapporteur
Agnès Trassoudaine	*Professeur, Université Clermont Auvergne, Institut Pascal*	Examinatrice
Christian Seassal	*Directeur de recherche CNRS, ECL, INL*	Directeur de thèse
Gilles Le Blevennec	*Ingénieur, CEA-Leti*	Encadrant de thèse
Emmanuel Drouard	*Maître de Conférences, ECL*	Membre invité

Thèse préparée au sein de l'INL UMR 5270 et du CEA-LETI

Acknowledgements

Three and a half years of research arrived to an end. Reflecting back, this doctoral thesis was far from a solitary endeavor and would not have been successful without the help and support of several people. In the next few lines, I would like to express my gratitude to all of them who in one way or another contributed to this work.

First and foremost, I would like to thank my thesis director Christian Seassal who trusted me with this work. His mentoring influenced deeply my personal and professional growth and guided me throughout my thesis. I hope I did my best to prove to him that I was the right choice for this project. From INL, I would also like to thank Emmanuel Drouard for his remarks and feedback regarding my results especially on the simulations part and for setting straight the interpretations based on the theoretical background of optics and photonics. Of course, I could not finish this paragraph without mentioning Hai Son Nguyen whose characterization expertise helped me understand and analyze the results, while his cheerful temperament and thirst for research motivated me to never ever give up. I am deeply grateful for the enthousiasm and the continuous support of my main supervisor at CEA LETI Gilles de Blevennec. Thank you for all the discussions and the knowledge you shared with me during these years and for showing me the multi-dimensional approach of a topic. Last but not least, I would like to express my thanks to Badhise Ben Bakir who co-supervised my thesis at LETI for his insight on my work and his useful comments and discussions.

I wish to extend my special thanks to Stephanie Le Calvez and Stephanie Gaugiran who welcomed me at their teams at LETI and were always there, very reactive and understanding, although they had to sign a bit too many fiche de mission for me to go to Lyon.

The assistance provided from the Nanolyon platform and especially from Radoslaw Mazurczyk and Pierre Cremillieu for the fabrication and from Aziz Benamrouche for the AFM characterization was greatly appreciated. Same for Sonia Nobre and Anas Benayad from LITEN and especially for Christophe Licitra and Nevine Rochat from LETI/PNCF where I spent so much time characterizing my samples.

I wish to show my appreciation to the fellow PhD students at LETI and INL for the moments we spend together supporting each other throughout the years. Events like the organization of the PhD days and the creation of the Lyon Optics Student Chapter at INL stand out as unique experiences of willingness and collaboration.

I am extremely grateful for all the discussions and informal chats I had with the members of both teams at INL and LETI that helped me develop my ideas and progress on my topic.

I would like to thank my thesis jury members, Fabrice Gourbilleau, Juan Martinez Pastor and Agnès Trassoudaine who accepted to review and examine my work.

At the end, I would also like to thank my friends, my family and Ali for their support, their patience especially during the writing of my thesis report and their encouragement at every step of the way. I am so very grateful about everything.

Eirini

Table of contents

General introduction

After the digital revolution, which began in the latter half of the 20th century, we saw the invention of the semiconductor, the personal computer and the internet to fundamentally change the society as a whole. Since then, digital technology is merging more and more in humans' lives. New ecosystems based on the continuous distribution and exchange of information shape the economy, science, education and our lifestyles.

As the most essential information acquisition medium of our time, displays have been developing faster than ever. From the bulky cathode ray tube (CRT) to compact flat panels such as liquid crystal display (LCD) and organic light-emitting diode (OLED), the display technologies have been greatly evolved to cope up with the human needs.

Nowadays, the next-generation displays address the interaction between the users and their environment, experience that, a short time ago, could only be found in the imagination of sci-fi writers. The great potential of virtual reality (VR) and augmented reality (AR) displays not only in the field of entertainment but also in the fields of health care, education, engineering design etc. has made this type of applications very attractive to the professionals, industries and the general public as well.

The VR and AR headsets contain an advanced level of optical technology. Merging into a virtual environment or just overlaying information on real world elements, the ultimate goal is the high resolution of the depiction combined with an exceptional color rendering. The challenge in this case is the miniaturization of the display dimensions and the decrease in the power consumption with a simultaneous performance enhancement.

OLED technology has been leading since several years the industry of small screens like smartphones and smartwatches. However, they are not able to offer the very high brightness that is needed for the microdisplays contained in the AR and VR headsets.

The only candidate that can meet the needs for pixel pitch smaller than 5 µm is the micro-LED. Micro-LEDs use extremely small LEDs that combine red, green, and blue subpixels to reproduce a color and just like the OLEDs are self-emissive.

Several decades before it was awarded the Nobel Prize in Physics in 2014, the GaN based blue LED had already paved the way for a low consumption, bright lighting.

These qualities made this material later attractive for microdisplay applications. GaN-based micro-LED combined with multicolor quantum dots (QDs) is a key candidate for the realization of microdisplay applications. However the advantages, the interaction between the blue LED and the QDs has been facing several challenges.

The aim is to understand the conditions that affect the near field coupling in the context of the InGaN/GaN-QDs configuration. The main focus is to study the impact of the photonic environment and the distance of the two components on their interaction as a means to improve the color conversion efficiency for the realization of compact, low consumption RGB micro-LED.

This PhD thesis is the result of the collaboration between the Laboratory of Emissive Components (LCEM) at CEA-Leti in Grenoble and the i-lum team of the Institute of Nanotechnology in Lyon (INL).

Chapter I - Towards highly efficient multicolor GaN-based micro-LED

I.1 Introduction

The micro-LED (light emitting diode) industry targeting a variety of applications from wearables such as augmented (AR), virtual (VR) and mixed reality (MR) headsets and smart watches, to automotive head up (HUD) and head mounted (HMD) displays and projectors, outdoor display boards etc., has already gained an important part of the microelectronics market.

Concerning microdisplay applications, the GaN based micro-LED is at the moment at the center of attention as it can fulfill the demands for a high quality depiction with a pixel pitch of less than 10 µm x 10 µm. At the same time, the technology for synthesizing semiconductor colloidal nanocrystals matures. Therefore, the design of a GaN LED nanocrystals has become a promising candidate as it permits an efficient multicolor lighting via color conversion. InGaN/GaN quantum wells (QW) combined with quantum dots (QDs) is one of the basic strategies towards the realization of an RGB microdisplay.

In such a configuration, it is essential to engineer the conditions for an optimal light coupling between the QW and the QDs. By taking into account the nanometric thickness of the blue of ultraviolet emitting QWs, their coupling with QDs can use more than one channel, including the non-radiative energy transfer (NRET).

The latter is an emitionless dipole-dipole interaction that takes place under specific conditions. This has been the topic of a large number of papers, investigating its dependence on the donor-acceptor distance, their mutual dipole orientation and on the photonic environment of the donor in the form of the local density of states (LDOS).

The goal of this chapter is to introduce the theory of NRET, the advantages of this coupling mechanism and how an adapted configuration can lead to a micro-LED design.

I.2 Towards the next generation microdisplays

The microdisplays are display units with screen sizes and resolution in the micrometer range. The pixel size depends on the application but is usually smaller than 10 µm with a diagonal of less than 1 inch as the example of FIG. I.1. In a variety of applications like in AR or VR HUD the microdisplays are combined with magnifying optics, which is necessary for the human eye to see the image. That means that this kind of screen must be able to display an image of similar quality to that of standard screens, especially in terms of definition.

Nowadays, these extremely small displays are found at the core of the hi-tech market, being a basic feature in a variety of applications which are presented in the schematic of FIG. I.2.

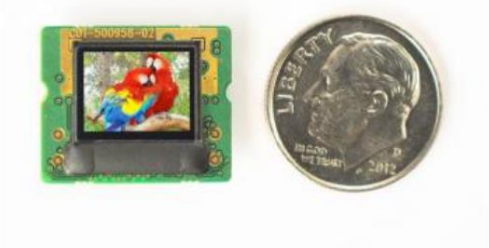

FIG. I.1. An example of an OLED multicolor microdisplay compared to a 10 cents of an American dollar coin (diameter around 18 mm).

Indeed, the miniaturization of the displays is a necessity for the future devices to be developed for gaming, military, industrial or medical applications.

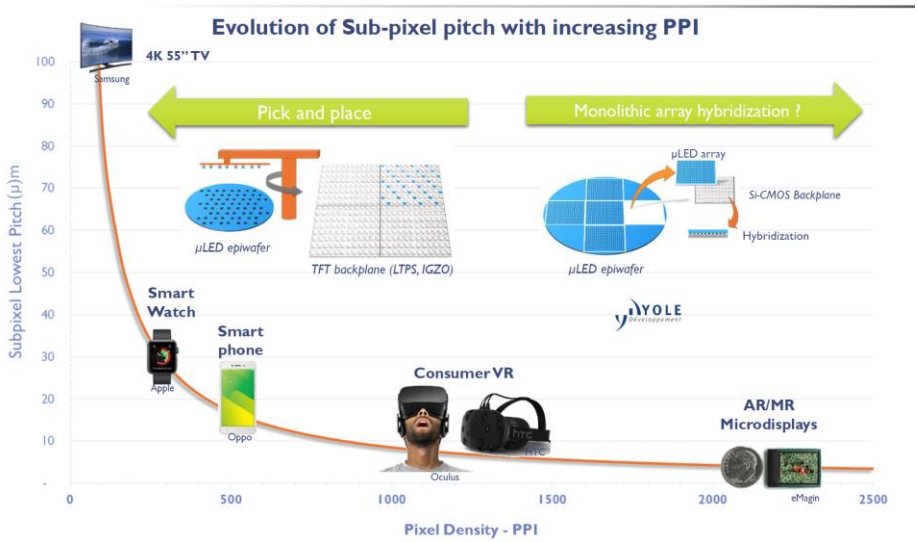

FIG. I.2. Relation between pixel pitch and pixel density needed for the various display applications (Eric Virey, Yole development, 2017).

It is common knowledge in the display area that the quality of a (micro)display is reflected to its high resolution and at the same time its low power consumption. When it comes to the micrometer scale though, the need for scaling down the pixel size and at the same time increase the pixel density is a complicated matter with several challenges involved apart from the goal for a high-resolution depiction. Power consumption, compactness and luminance are all new technological challenges to be met.

I.3 The emerging technology of micro-LED: pixel pitch < 5 μm for AR/VR

Nowadays, the mainstream near-to-eye or head-mounted displays devoted to AR/MR/VR applications, are mostly based on the liquid-crystal (LCD) or organic light emitting diode (OLED) technology[1]. The LCDs, the oldest screen type, have a slow response speed, poor conversion efficiency and low color saturation as they need backlighting. Because of these drawbacks, they are gradually being replaced by the self-emissive OLED displays that have the advantages of wide viewing angles, high contrast, low power consumption, fast response speeds and an excellent material flexibility and transparency. However, the organic materials of their light emitting layer have shown drawbacks such as rapid aging, short life span and low color purity along with the fact that they need specific approaches for encapsulation[2],[3]. Another limitation is that they do not show a very bright emission in the blue. From the above, it became clear that due the technical limitations, LCD and OLED are not adapted to the demanding display performance of AR//MR and VR applications.

A micro-LED is a GaN based self-emissive microscopic LED that corresponds to an individual pixel element. More specifically, the main reason it is preferred for AR//MR and VR applications is that it can provide the highest brightness (along with the highest contrast)[4] than any other display technology and a low power consumption[5]. Additionally, micro-LEDs are more compact than LCDs and OLEDs, as there is no need for complex encapsulation or polarizer as presented at the schematic of FIG. I.3.

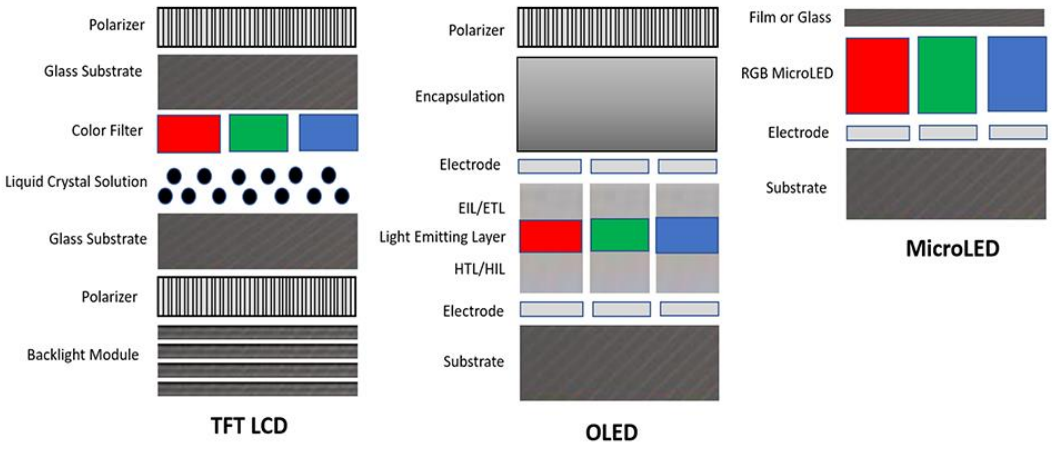

FIG. I.3. A comparison of the main features of TFT-LCD, OLED and micro-LED displays.

Their innate properties are even attractive for TV and other large-scale applications as they have the potential to match or exceed today's widely applied OLED displays[6]. This is because

micro-LED technology is capable of providing all the advantages of an OLED microdisplay with the added values of very high brightness level and a wide color Gamut.

According to Research and Markets, the global micro-LED display market is predicted to soar from USD 0.6 billion in 2019 to USD 20.5 billion in 2025, with a compound annual growth rate of about 80%[7]. According to Yole's optimistic estimate, the market of micro-LED display will reach 330 million units by 2025, depicted in the graph below[3].

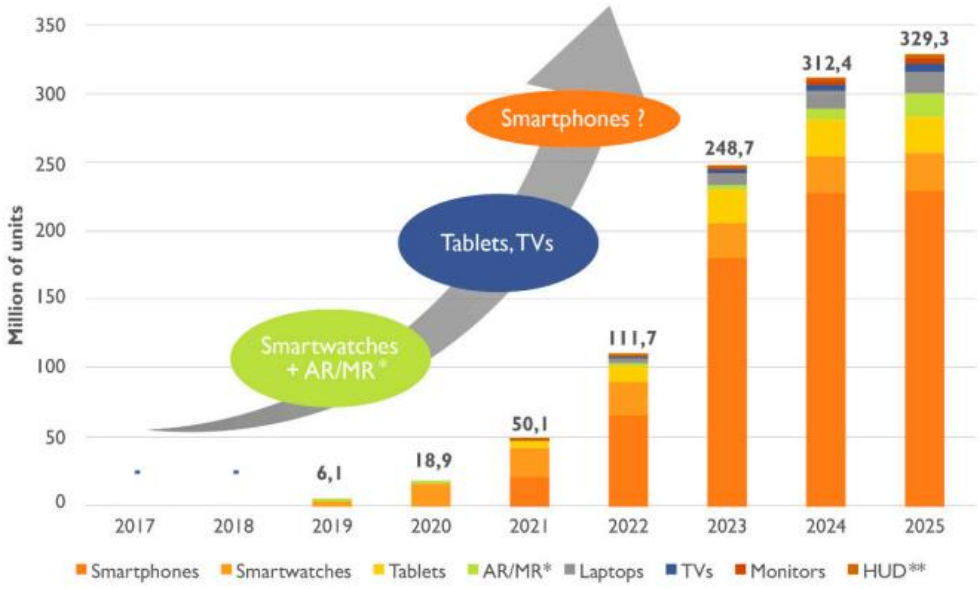

FIG. I.4. Forecast of micro-LED displays[3].

In the final analysis though, the main reason for the above-described market outbreak is the sharp increase in demand for brighter and more energy-efficient display panels.

Although the micro-LED display fabrication has not matured yet and faces several challenges that prevent the commercialization of micro-LED displays, they are still considered the future of microdisplay applications. The two main technical problems of this technology are the mass transfer of LED chips[8] and the production of a full-color display[9]. In this work we will focus on the second aspect.

I.4 GaN based micro-LED for Full-Color microdisplays

Since the invention of the blue LED in the early 1990's[10], the fabrication of the first micro-LED, which had a diameter of 12 μm, was reported back in 2000 from the team of H. X. Jiang's group[11], while the first blue microdisplays fabricated from InGaN/GaN QW with a dimension of 0.5×0.5 mm2 consisting of 10 x 10 pixels soon followed one year later[12].

However, for the display applications it is necessary to obtain the three primary colors: red, green and blue (RGB). The final color (nuance) of the pitch is adjusted by the CMOS current ratio among the three colors.

The realization of full color is one of the main difficulties of the micro-LED displays. The main approaches[3],[13] that are used to improve the RGB rendering are analysed below. They include RGB micro-LED integration through transfer printing, direct growth of multicolor micro-LEDs on the same substrate and the addition of a color conversion layer.

I.4.1 Transfer printing

The fabrication method that has been the most widely used so far for large scale displays is the transfer printing. It is based on the pick-up of each micro-LED color separately from a donor wafer and their subsequent deposition onto a receiver (display) substrate as only single-color micro-LED can be developed on the same substrate. This method was also applied for microdisplays[14],[15] but it was proven to be too challenging in the microscale[16]. The bottleneck of this time-consuming method is the transfer and current control of 25 million micro-LED with placement of accuracy of 1μm.

I.4.2 Growth methods for monolithic integration

Various growth approaches have been introduced to enable the monolithic integration of multi-color micro-LED pixels on the same chip. That would mean that one material should have the capability to span from the blue to the red spectrum. Although the idea seems promising, fabricating this kind of structures still faces difficulties on the full-color front.

The most common method is controlling and varying the indium composition using selective area epitaxy. InGaN/GaN can theoretically achieve that, by adjusting the indium percentage in the InGaN alloy. In reality though, a high indium percentage causes an important lattice mismatch in the epilayers, which leads to a poorly efficient red InGaN micro-LED. On that front, an innovative substrate called InGaNOS that can handle the problem of the lattice mismatch has been proposed[17]. Other methods including selective carrier injection into multiple quantum wells of different indium compositions[18],[19] and generating and controlling colors using local strain engineering[20],[21] have as well been presented.

Nanowires have been also studied for a potential use in full-color micro-LED displays[22],[23],[24]. In this case, the modulation of their emission wavelength is possible by changing their composition, diameter, and injection current. Their advantages over the

conventional InGaN/GaN LEDs are the reduction of the dislocation density and hence the polarization field in the active region, improving the light extraction efficiency with low cost and large-area silicon substrates[25]. Nevertheless, their growth conditions are not yet fully controllable, which means that the growth distribution is not 100% uniform. In addition, the defects on the surfaces of the nanowires cause non-radiative recombination of the carriers, a limitation which leads to reduced internal quantum efficiencies.

I.4.3 Color conversion

A widely developed approach consists in using a monochrome GaN-based LED, typically emitting in the blue, and down-converting a part of the light to red and green. The role of the down-conversion layer deposited on a LED surface is to absorb the high-energy photons that are electrically generated in the LED and to subsequently reemit lower-energy photons. The color conversion is a well-studied technique that apart from the LED has other applications including the conversion that facilitates the light absorption in classical solar cells[26],[27].So, in order to achieve the full-color display, the micro-LED is used as the excitation source to stimulate the emission of color-conversion materials such as nanophosphors[28], QDs[29], QW and lately perovskites[30],[31].

Phosphors are composed of wide band gap materials (such as oxides, nitrides, and sulfides) and a small number of doping ions (transition metals or rare earth). Although phosphors have mature preparation technology, high thermal and chemical stability, and a good quantum yield[32], particle size reduction is highly needed for micro-LED display applications[33]. With micron level dimensions[34], it is not possible to uniformly coat micro-LED pixels of the same size. Therefore, they are not able to provide sufficient luminance and yield to support high-resolution displays as the LED chip size shrinks to below 20 μm.

On the other hand, QDs are nanometric semiconductor particles (in the range of 1–10 nm[35]) with a high quantum yield, a broad absorption and a narrow emission spectrum. Their emission wavelength is related to their size, shape, and composition and thus, it can be respectively adjusted to realize a full color micro-LED display[36],[37],[38]. The main methods to deposit QDs include spin coating[39], aerosol printing technology[40], photolithography technology[41], inkjet printing[42],[43], and the pulse spraying method[44]. In addition, due to their narrow emission linewidth, they can lead to a good color purity. Therefore, the above properties show that at the moment QDs are more suitable for full-color micro-LED displays than classical phosphors.

Their advantages can lead to an easy microdisplay manufacturing with a wider color gamut and good color purity.

The QD based full-color micro-LED display has an unparalleled color expression potential as a it combines the narrow and continuous emission spectrum of QDs with the robustness of the LED. According to the Recommendation BT.2020 published by The International Telecommunication Union Radiocommunication Sector (ITU-R), QD micro-LED displays are in the leading position with their 83% color purity, while OLED displays can only reach 75% at most[16]. Nevertheless, the stability and conversion efficiency of the QDs present limitations.

First, the stability of QDs will directly affect the reliability and life of color micro-LED displays. Former studies have shown that QD stability can be improved by methods such as ion doping, engineering the design of the QD ligand surface, and encapsulation of the QDs with polymers or oxide materials. Furthermore, research is done on the replacement of the toxic heavy metals that the QDs contain with other materials and at the same time maintain their advantageous properties.

I.5 Color conversion InGaN/GaN-QD LED

Despite the aforementioned bottlenecks, QDs are undoubtedly the most popular color conversion medium; which makes the InGaN/GaN-QD configuration the most common color conversion method for RGB micro-LED[45],[46],[47]. However, the limitations concerning the conversion efficiency of the QDs affect the power consumption and life of QD displays and thus, their improvement is of paramount importance.

In this configuration, potential optical losses may lead to a low radiative transfer. Because of several energy-loss steps, i.e., waveguided leaky modes, light-scattering from the QDs and the reduced absorption capability of the QD layer. the efficiency of radiative transfer is relatively low[48], <10%.

I.6 NRET based micro-LED

M. Achermann et al.[49] experimentally proved the theoretical work of Basko et al. [50],[51] regarding the excitation of QDs via non-radiative energy transfer (NRET) from a InGaN QW in close proximity. This process is the consequence of dipole-dipole interactions associated with the QW-QD coupling.

NRET involves the transport of an excited electron-hole pair from an emitter (donor) to an absorbing medium (acceptor). The coupling is mediated by near field interactions without the emission of photons and can be understood as the quenching of the donor dipole in the presence of a lossy medium[52]. This alternative path for indirect injection of electron-hole pairs into QDs is characterized by the extremely fast intraband relaxation in colloidal QDs (subpicosecond time scales). As the schematic in FIG. I.5 shows, the NRET is fundamentally different from the standard down conversion scheme. The advantage of NRET is its emitionless nature that eliminates the energy losses of the intermediate steps involved in the down conversion and hence leads to an efficiency increase. But at the same time, there are strong requirements in order to promote this effect, including a very close proximity between the donor and the acceptor, as we will introduce later.

A micro-LED advanced configuration can be possible by taking advantage the QD properties and their increased absorption capability when excited via NRET. However, it is important to note that in this frame, the radiative and the non-radiative energy transfer would coexist.

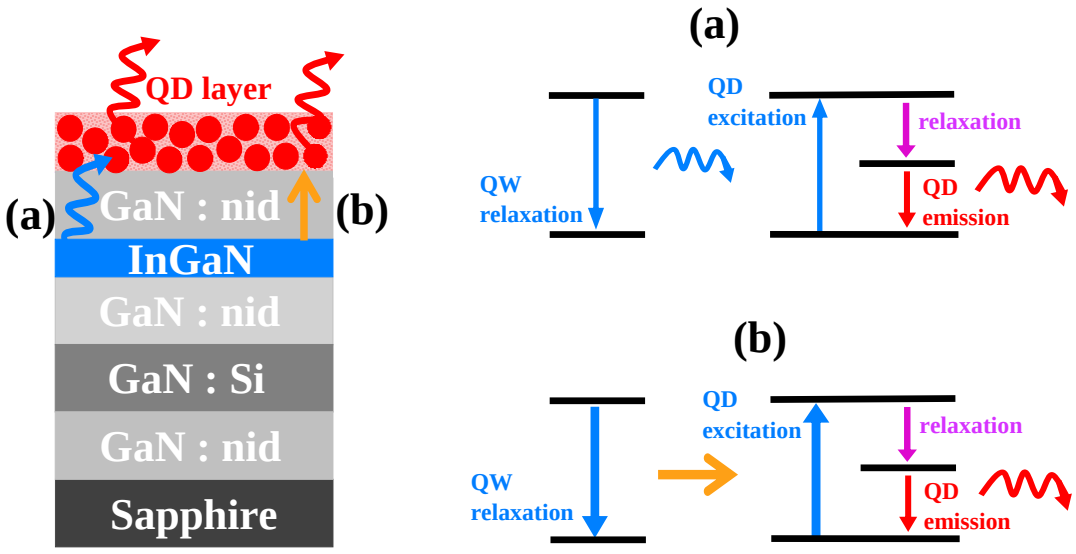

FIG. I.5. The InGaN-QD layer structure with the QW in nanometric distance from the QD. The QW (donor) and QD (acceptor) are characterized by a set of discrete energy levels. (a) The standard color conversion process where the QW's blue photon will be absorbed by the red QD. The latter will then relax to its ground state and emit a red photon. (b)During NRET the energy from the excited state of the donor (QW) is directly transmitted to the excited state of the acceptor (QD). There it will relax to the ground state with the simultaneous emission of a red photon.

I.6.1 Theoretical background

The non-radiative energy transfer is based on the pioneering work of Förster, who analysed the principle of the energy transfer between a fluorophore to another dye molecule[53]. It is also known as Förster resonant energy transfer (FRET).

The dipole-dipole approximation is employed for electronic coupling between donor (D) and acceptor (A). It is considered that the relaxation after electronic excitation of donor takes place on a much faster time-scale as compared to the energy transfer itself. As it is presented in FIG. I.6, the energy transfer is the Coulomb (electrostatic) interaction between the charge distributions of a D and an A particle.

With this in mind and under specific conditions that will be later discussed, during FRET the energy will be transferred from the excited state of the donor directly to the excited state of the acceptor, without the emission and absorption of photon. In the schematic, μ_D and μ_A are the transition dipole moments of the donor and the acceptor respectively. Then, the D-A separation is characterised by the vector R, while n_D and n_A are the corresponding unit vectors respectively. Initially, the donor is in its excited state whereas the acceptor is in its ground state.

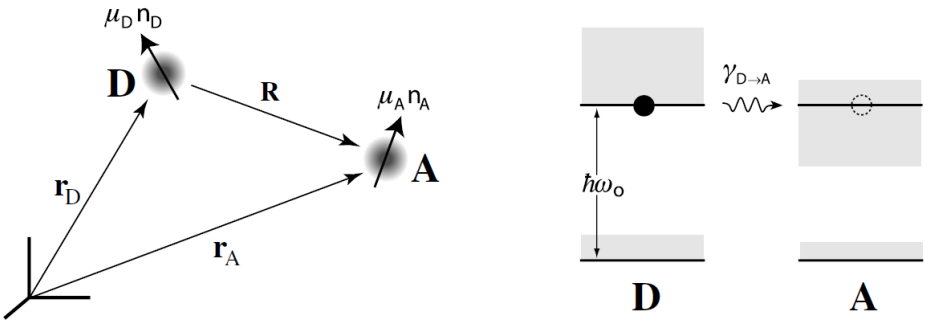

FIG. I.6. The Donor- acceptor scheme involved in the energy transfer. Classically, the donor is a dipole radiating at the frequency ω_0 while the acceptor dipole absorbs in the same frequency. Both systems are embedded in a medium with the same refractive index $n(\omega)$.

In this section, we are interested in calculating energy transfer rate $\gamma_{D\to A}$ from the donor to the acceptor. In order to do that, we will use the theoretical approach within the quasi-classical framework developed by Novotny and Hecht[54]. Starting from the equation that aligns the quantum mechanics with the classical approach:

$$\frac{\gamma_{D\to A}}{\gamma_0} = \frac{P_{D\to A}}{P_0} \tag{I.1}$$

, where γ_0 is the donor's decay rate in the absence of the acceptor, $P_{D\to A}$ is the donor's energy per unit time absorbed by the acceptor, and P_0 is the energy per unit time released from the donor in the absence of the acceptor, which are respectively given by the following equations:

$$\gamma_0 = q_i \frac{1}{4\pi\varepsilon_0} \frac{2q^2\omega_0^2}{3mc^3} \tag{I.2}$$

$$P_0 = \frac{\left|\mu_D\right|^2 n(\omega_0)}{12\pi\varepsilon_0 c^3} {\omega_0}^2 \tag{I.3}$$

$$P = \frac{\left|\mu\right|^2}{4\pi\varepsilon_0\varepsilon} \frac{n^3\omega^4}{3c^3} \Rightarrow P_{D\to A} = \frac{\omega_0}{2} \mathrm{Im}\{\alpha_A\} \left|n_A \cdot E_D(r_A)\right|^2 \tag{I.4}$$

We see that γ_0 depends on the oscillation frequency (ω_0) and the particle's mass (m) and charge (q). P_0 reflects the energy that carries the transition dipole moment of the donor (μ_D), the frequency and the refractive index of the medium $n(\omega_0)$. The calculation of the power transferred from donor to acceptor from the general left-hand side of the equation 1.4, taking into account the Poynting's theorem and the dipole approximation, ends up at the right-hand side that involves the electric field generated by the donor $E_D(r_A)$ at the origin of the acceptor and the imaginary part of the acceptor's polarizability vector $Im\{\alpha_A\}$. Here it is important to note that the acceptor's dipole moment is not permanent, but induced by the donor's electric field.

Now, by expressing the polarizability in terms of the absorption cross section (σ) and introducing the free-space Green's function for the description of the donor's electric field, we obtain the result:

$$\frac{\gamma_{D\to A}}{\gamma_0} = \frac{9c^4}{8\pi R^6} \int_0^\infty \frac{f_D(\omega)\sigma_A(\omega)}{n^4(\omega)\omega^4} T(\omega) d\omega \tag{I.5}$$

The donor-acceptor transfer rate requires the spectral overlap of the donor's normalized emission spectrum with the acceptor's absorption cross-section. $T(\omega)$ corresponds to a function

that takes into account the orientation dependence and the distance dependence of the transfer rate and it is expressed with the help of the free-space Green's function $\overleftrightarrow{G}$ as follows:

$$T(\omega_0) = 16\pi^2 k^4 R^6 \left| n_A \cdot \overleftrightarrow{G}(r_D, r_A) n_D \right|^2 \tag{I.6}$$

Before moving on, we have to first evaluate the impact of the $T(\omega)$ on $\gamma_{D\to A}$. In FIG. I.7 the function $T(\omega)$ is plotted versus the normalized distance for the three mutual dipole orientations of the donor and the acceptor (arrows).

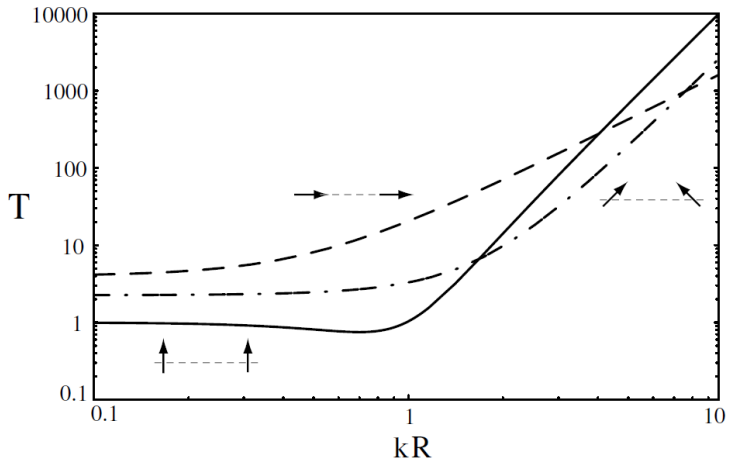

FIG. I.7. $T(\omega)$ versus the normalized distance for the three mutual dipole orientations of the donor and the acceptor (arrows)[54].

For $kR \ll 1$, the short-distance transfer scales as R^{-6} as $T(\omega)$ is constant. For $kR \gg 1$, the long-distance transfer depends on the relative or mutual orientation of the donor-acceptor dipoles. For aligned dipoles, $T(\omega) \sim (kR)^2$ and thus $\gamma_{D\to A} \sim R^{-4}$. For not aligned dipoles there is a $T(\omega) \sim (kR)^4$ dependence and $\gamma_{D\to A} \sim R^{-2}$.

Now, taking into account the situation that the single donor–acceptor pair is subject to random rotational diffusion in the same way that the dipole orientations are not known and the transfer rate has to be determined by a statistical average over many donor–acceptor pairs, equation I.6 will be modified by inserting the free-space dyadic Green's function and by replacing $T(\omega)$ by its orientational average):

$$\langle T(\omega) \rangle = \frac{2}{3} + \frac{2}{9} k^2 R^2 + \frac{2}{9} k^4 R^4, \; k = \frac{2\pi n(\omega)}{\lambda} \tag{I.7}$$

It is obvious that the transfer rate decays very rapidly with distance R. Consequently, only distances where $R \ll 1/k$ are experimentally significant, while the terms $\sim R^2$ and $\sim R^4$can be neglected. In this limit, and the transfer rate becomes:

$$\gamma_{D\to A} = \gamma_0 \cdot \left(\frac{R_0}{R}\right)^6, \; R_0{}^6 = \frac{9c^4\kappa^2}{8\pi}\int_0^\infty \frac{f_D(\omega)\sigma_A(\omega)}{n^4(\omega)\omega^4}d\omega \tag{I.8}$$

, where R_0 is the so called Förster radius and its value is typically in the range of 2-9 nm[55]. It is defined as the energy transfer efficiency between donor and acceptor and when $R = R_0$ the transfer rate is equal to the decay rate of the donor in the absence of the acceptor.

Therefore, the energy transfer rate depends on a number of factors including the separation between the donor and the acceptor, the relative orientation of the transition dipole moments and the emission rate of the donor, the spectral overlap between the emission of the donor and absorption of the acceptor, and the dimensionality of the donor and acceptor[56],[57].

Energy transfer between particles is a photophysical process encountered in various systems. It is known that single-molecule FRET is a versatile tool for studying biomolecules in a quantitative manner. Because the efficiency of NRET is very sensitive to the separation between the donor and acceptor, it is used to measure distances in biological systems[58] and in nanoscale sensors with high specificity and low detection limits[59]. Engineering the spectral overlap between the donor and acceptor offers another way to control the NRET rate[60]. The complex environments in photosynthetic systems require a greater understanding of the role of dielectric screening in tuning dipole-dipole coupling and the rate of energy transfer[61],[62].

I.6.1.1 State of the art: InGaN-QD structures for micro-LEDs based on NRET

With the implementation of QDs on LEDs, the energy transfer process has been considered as a means to solve existing problems that mainly have to do with radiative optical losses. NRET is an alternative method that could achieve increased color conversion efficiency.

For an efficient non-radiative energy transfer, it is necessary for the donor and the acceptor to be in sufficiently close proximity. The latter gave rise to several original geometrical configurations such as holes, pillars and rings[63], examples of which we can see in FIG. I.8. In all the cases, the time decay of the donor was faster while there was also a decrease at its emission combined with a simultaneous increase of the acceptor's emission after coating the LED with QDs. Very promising InGaN/GaN-QD architectures are composed of vertically

etched patterns that allow the positioning of the nano-emitters very close to the QW[64]; that permits a NRET rate of around 82% and a color conversion efficiency of 20%. In a recent study[65] the reported NRET efficiency for a InGaN/GaN-QD LED patterned structure was measured to be 88% Another research team that fabricated blue InGaN/GaN nanohole light-emitting diodes filled with CdSe/ZnS core/shell nanocrystals as color conversion media came to the conclusion that the color conversion efficiency and effective quantum yield of the nanohole light-emitting diodes were nearly twice as much as those of standard planar light-emitting diodes[66].

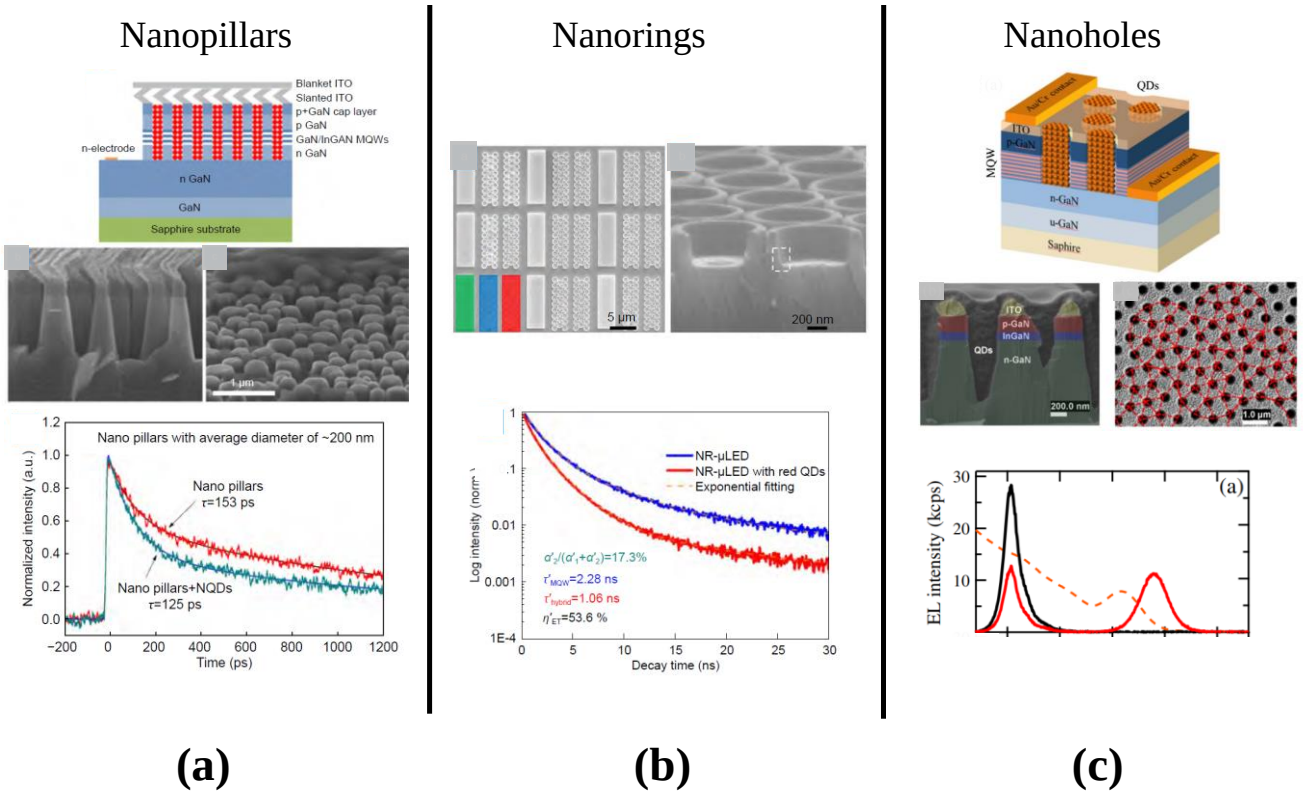

FIG. I.8. (a) Schematic of the nano-pillar LED, followed by the SEM images of the cross-section and a tilted view of the QD-coated nanopillars. The graph at the bottom corresponds to the time-resolved photoluminescence decay curves of a nano-pillar LED sample with and without QD-coating[67]. (b) SEM image of RGB pixel array composed of nanorings on the top left and next to it a tilted image of the nanorings. At the bottom the TRPL curves of nano-ring micro-LED with and without red QDs[68]. (c) Schematic representation, cross-sectional, and top SEM images of a photonic quasicrystal LED hybridized with QD color converters. At the bottom is the ectroluminescence spectra of the LED before (black solid line) and after hybridization (red solid line)[69].

I.6.1.2 The relation between NRET rate and LDOS at donor emission: a debate

Since the pioneering works of Purcell[70] and Drexhage[71], it is well established that the photonic environment of a single emitter has the ability to modify its luminescence properties through the local density of states, what is known as Purcell effect[54],[72]. This concept was successfully demonstrated in different configurations including cavity quantum electrodynamics[73], photonic band gap materials[74] and plasmonic nanoantennas[75],[76].

Now in the case of a dipole-dipole interaction where two emitters are involved, the influence of the photonic mode density on the non-radiative energy transfer remains an unresolved debate. This is because there is no clear quantitative experimental evidence that the photonic environment can purely control the NRET between the donor-acceptor pair. The main reasons behind that rely on the competition of the NRET with the donor's direct emission and the donor's losses to its environment. In this way, it is very hard to distinguish and thus properly quantify the NRET impact on the overall emission. In addition, in several cases the experimental procedure is only focused on the radiation of the donor, therefore all the essential information that is contained in the emission of the acceptor is not evaluated whatsoever.

Meanwhile the NRET has significant applications mainly in the field of single-molecule biophysics. Given that, the role of the photonic mode density near interfaces in the context of the NRET has since long ago been the focus of many experimental and theoretical studies. The groundbreaking work of Hopmeier et al.[77] and Andrew and Barnes[78] which later followed by others[79],[80] showed that in resonant microcavities the energy transfer rate depends linearly on the donor decay rate, and thus on the LDOS at the donor emission frequency. Later, experimental studies in different configurations involving dispersing and absorbing media[81] and media with a resonance effect such as plasmonic antennas[82],[83],[84],[85],[86], optical microcavities[87], plasmonic nanoapertures[88],[89], plasmonic nanoparticle arrays[90],[91] and waveguides[92],[93] were also proposed to support the LDOS dependence on the NRET by significantly enhancing the NRET rate. At the same time, several theoretical works that presented the possibility to control the NRET parameters in complex environments[94], via plasmon-assisted amplification of electric fields[95],[96] via a static magnetic field in a nanostructured environment[97], microresonators[98],[99], and even at the vicinity of a glass/water interface[100] resulted in an enhanced dependence on the mode density as well.

This subject became controversial as instead of a linear, other studies suggested a quadratic dependence[101] or even no dependence at all between the LDOS and the NRET. More

specifically the NRET rate constant was shown to be barely affected by mirrors[102],[103], dielectric nanoparticles[104] and the refractive index[105], possibly because this kind of weakly dispersive photonic environments do not provide enough field confinement. In FIG. I.9 examples that employ dispersive and non-dispersive media in order to approach the LDOS impact on the NRET are presented. In order to assess the impact of LDOS on NRET, it would be then appropriate to make use of a highly dispersive medium, leading to strong modifications of LDOS, i.e., photonic crystals, which will be introduced in the next section.

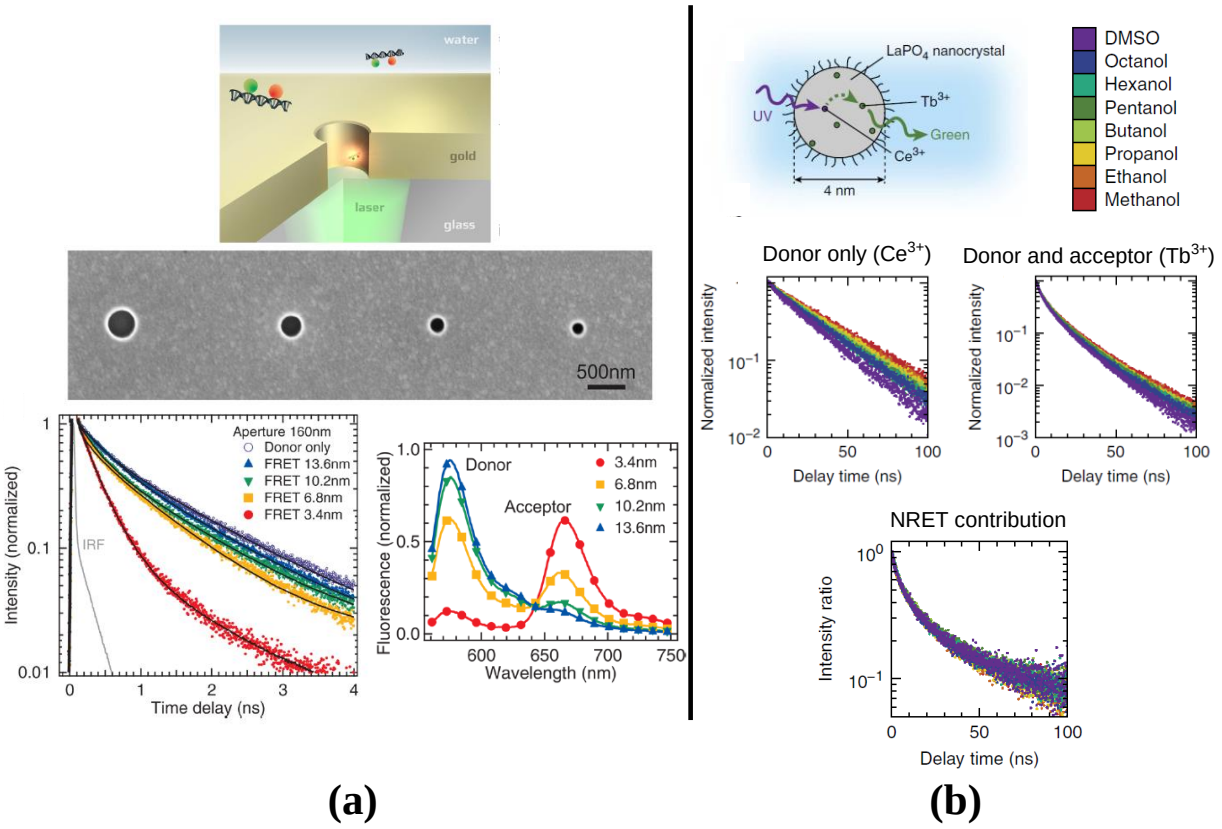

FIG. I.9. An example of a case of the LDOS impact on the energy transfer in the case of the environment change because of (a) a nanoaperture[88] and of (b) the refractive index[105]. More precisely in the schematic at (a) the configuration includes a donor-acceptor pair on a DNA molecule diffusing inside and around a single gold nanoaperture which we can see at the SEM image just below it. Then the TRPL measurements show a faster decay for the smallest diameter along with an increased acceptor intensity compared to the rest. On the contrary, in (b) the change of the refractive index of the solvent does not affect the NRET between donor and acceptor molecules as the TRPL ratio at the bottom shows.

I.6.2 Photonic Crystals: patterning for controlling the LDOS

Patterning surfaces and thin layers at the wavelength scale leads to the possibility to tailor their photonic environment, and therefore the LDOS. Hence, it has been considered as a key approach so as to manipulate the non-radiative energy including in dielectric[106],[107] and porous silicon[108] photonic crystals, but also hyperbolic metamaterial comprised of an array of gold nanorods[109] etc. Concerning our configuration, by designing a NRET based InGaN/GaN multi QW structure with QDs embedded in a photonic crystal pattern Krishnan *et al*. showed a color conversion effective yield of 123%[69].

A photonic crystal (PC) is a periodic dielectric medium with a lattice constant of the order of the operation wavelength[110],[111],[112]. The PC can be periodic in one, two and three dimensions. However, in the field of nano-optics and photonics, the most commonly used types are the 2D PC lattice due to their compatibility with standard lithography and etching processes already developed for semiconductor materials.

A key characteristic of a PC is its band structure, displaying the photon frequencies as a function of the in-plane projection of the wave vector $k_{||}$ in a given direction, as in Fig.I.10 in the case of a 2D PC. Such a component of the wave vector is given by:

$$|k| = \sqrt{k_{||}^2 + k_{\perp}^2} \tag{I.9}$$

The band structure shows the eigen-states in terms of eigen-frequencies (resonant frequency) of the periodic structure, which illustrates how light propagation takes place in such an optical medium. Photons can propagate inside the structure only within allowed frequencies.

In case a PC is illuminated from the outside radiative continuum, light can be coupled into the structure at certain conditions related to symmetry matching between the incident wave and the PC optical mode. The origin of the photonic band diagram of PC can be explained via the Bloch theorem, very similar to the electronic band diagram of solid states crystal. Therefore, in a periodic PC pattern, the optical modes are called photonic Bloch modes and are characteristic of a particular lattice, as their behavior is determined by the properties of the lattice including the refractive index distribution for optical waves.

Now given an $\omega - k$ diagram like the one of FIG. I.10, the kinetic information of the light propagation can be derived. The first derivative of the value of the frequency (ω) along the y-axis to the value of the wavevector (k) along the x-axis, gives the so called group velocity:

$$\upsilon_g = \frac{\partial \omega}{\partial k} \tag{I.10}$$

, which can be evaluated by the slope of the photonic bands, through which the two basic confinement schemes of the PC structures can be interpreted.

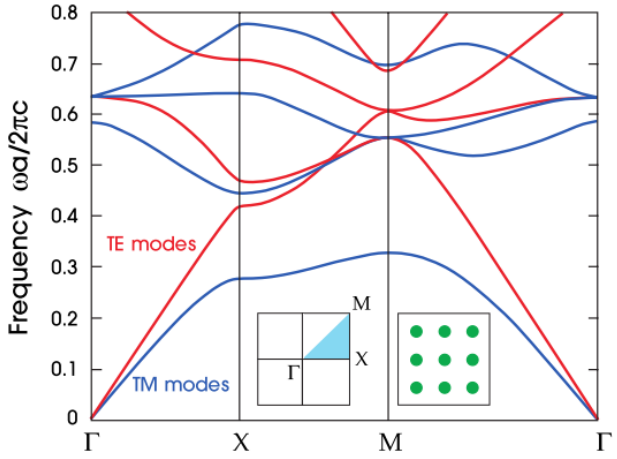

FIG. I.10. Example of the band structure of a 2D PC lattice. The first Brillouin zone of the square lattice of dielectric rods is shown in the inset. Γ corresponds to the k point $(0,0)$, X denotes $(0,\ p/a)$, and M denotes $(p/a\ p/a)$,. Both TE and TM modes are depicted with a photonic bandgap for the TM only[111].

Firstly, if a photonic crystal operates around an extremum of the dispersion characteristic (see FIG. I.11), the group velocity is equal to zero. Such slow light modes can be used in order to promote incident light trapping. In order to efficiently confine the photons in all the directions or angles, it useful to design a PC displaying extrema with a very small band slope.

Moreover, as in the case of the semiconductors' electronic bandgap, the photonic bandgap refers to the energy or frequency range where the light propagation is prohibited inside the PC. However, if a defect is introduced in the strictly periodic structure of the PC, new eigen-state appears inside the bandgap with energy that corresponds to the eigen-frequency of the defect. Thus, only the radiation within the defect frequency will be confined inside the structure. In other words, in PC the equivalent of the semiconductor dopant, is the creation of a defect that according to the Bloch-Floquet theorem is able to confine the light and localize it.

Both approaches could be used in such a way to control the energy transfer between a donor and an acceptor by locally increasing the LDOS in their surrounding medium.

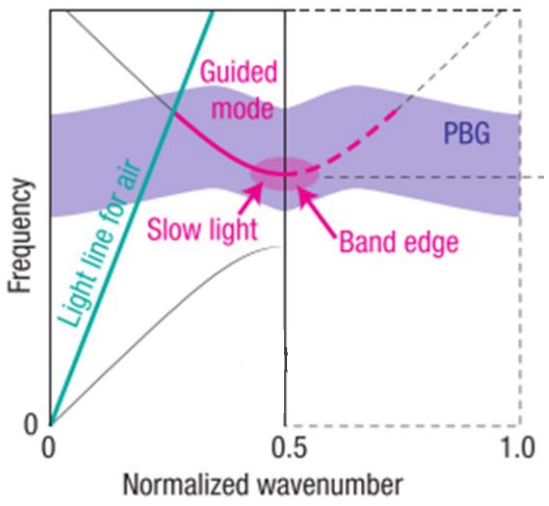

FIG. I.11. Example of a band dispersion of a 2D PC waveguide where is demonstrated the slow light region[113].

I.7 Thesis objective

The main goal of this PhD thesis is to realize a thorough study on the conditions that affect the NRET in the context of the InGaN/GaN-QDs interaction as a means to improve the color conversion efficiency for RGB micro-LED applications.

Our motivation is based on the fact, that despite the recently accumulated knowledge on the topic, the quantification of the basic parameters that affect the energy transfer across a heterogeneous interface remain weakly explored. Facing a non-classical situation, in the sense of an alternative manner to couple the light, its investigation is important both in terms of fundamental science as well as in order to optimize the efficiency of NRET-based excitation schemes in applied devices.

The thesis work is focused on the theoretical and experimental study of the three main parameters that affect the NRET rate: the dipole orientation of the donor, the donor-acceptor spacing and the LDOS.

In Chapter II, we investigate the dipole orientation and the polarization in a single InGaN QW by using the Maxwell's theory. By varying the GaN cap layer thickness on top of the QW, we aim at controlling the dipole electromagnetic environment and observe the impact on its orientation.

Then Chapter III is devoted to the InGaN-QD coupling efficiency. As a non-homogeneous configuration, the theoretical predictions on the energy transfer are evaluated by addressing the limits of the donor-acceptor distance.

Lastly, Chapter IV addresses the impact of LDOS. With the implementation of TiO_2 photonic crystal structures with resonances in the red or in the green, we aim at creating suitable conditions that may give rise to the energy transfer between green and red QDs.

Towards the same quest, preliminary studies concerning the impact of the local photonic density of states supported by an InGaN/GaN circular grating on its coupling with QDs have been performed. This will be briefly addressed in the last Chapter.

Chapter II - Study of the dipole orientation and polarized emission of a single InGaN/GaN QW near the top interface

II.1 Introduction

In the case of LEDs for micro display applications, two of the main goals in the optoelectronics and photonics research are the emission rate enhancement and the precise control of the wavefront of the emitted light. The control of the polarization is a parameter of primal importance for the enhancement of the LED efficiency and in our case, we can achieve that by taking advantage of the NRET coupling properties. The non-radiative energy transfer in an InGaN/GaN quantum well (QW)-quantum dots (QDs) configuration is a dipole-dipole interaction. In the NRET theory, the QW and QDs can be described as donor and acceptor dipoles respectively. Although the QDs are intrinsically non-polarized, their polarization is induced by the electric field of the donor[114]. That means that the QW is responsible for the possible polarization combinations between the donor and the acceptor that can enhance or inhibit the coupling and therefore the emission rate. A uniform dipole orientation in the QW can be the source of a polarized emission from the QDs and thus, it is crucial to know and control the orientation of the dipole in the QW.

In this chapter, we investigate the impact of the single InGaN/GaN QW localization first on its dipole orientation and then on its polarized emission. The thickness of the GaN top layer (or cap layer) was chosen to be 5, 8 and 12 nm. This choice was based on the non-radiative energy transfer theory, which calculates the optimal distance between the donor and the acceptor dipoles to be 10 nm for a maximized NRET emission rate (at least for homogeneous media). That means that in our case, the QW should be localized close to the GaN/air interface.

In a first step, we examine the orientation of the dipoles in the QW. Based on the mathematical calculation of the spontaneous decay rate that is derived from the Maxwell equations, by using the calculations of Novotny[114],[115] and Hecht[116] we can describe the radiation of an arbitrary oriented dipole near a planar interface (here a GaN/air interface). The simulated results can be directly associated with experimental data since the decay rate is the inverse of the lifetime. Moreover, we show that by making use of a simple model based on time resolved photoluminescence measurements, we can actually estimate the percentage of the dipoles that have a vertical orientation with respect to the substrate for the three cap layer thicknesses, in the spontaneous emission regime.

Now as it is not possible to directly measure the dipole orientation in the QW, observing the polarization of the active zone's emission can give an additional insight to this matter. By making use of a rotational polarizer and with the help of a confocal microscope, we are able to measure the perpendicular and in plane -with respect to the substrate- QW emission and

evaluate the polarization ratio in the spontaneous emission regime. This experimental study constitutes the second part of this chapter.

II.2 Dipole orientation and polarization in LED structures

It has been proven that the non-isotropic emitter orientation in OLEDs is a key factor that, if carefully studied, can enhance its EQE and should be taken into account[117],[118]. Then, we see that effort is being put to the enhancement of the emission efficiency and the simultaneous EQE droop effect in GaN based LED with the coupling of the dipoles from the active region to surface plasmons[119],[120],[121]. Sei-Yong Kim et al.[122] demonstrated that the emitters in an OLED structure have a preferential orientation with a ratio of 0.77:0.23 parallel to the stacking plane to vertical dipoles while an EQE of 40% can be achieved in that case.

Now, in the literature it is generally considered, that the dipoles in InGaN are in the plane of the QW[123],[124]. The reason behind that is that this kind of stacks of III-V nitrides exhibit a high spontaneous and piezoelectric polarization charge that induces a large compressive strain in the QW along the 0001 direction. The result of this strain is the creation of an electrostatic field in the InGaN layer. Since 2000, many studies on nonpolar and semipolar oriented nitride materials and device structures have established that the dipole emitter in c-oriented GaN LED lies in the plane of the QWs[125],[123],[124]. This polarization anisotropy can be measured by electroluminescence[126] or photoluminescence[127],[128].

Up to this point and to the best of our knowledge, there has been no equivalent study that analyses both experimentally and theoretically the material and physical properties of a single InGaN/GaN QW grown in c-axis, that correlate its dipole orientation with the polarized emission.

II.3 The impact of the photonic environment on the dipole orientation

The thickness of the cap layer (hc) is a factor that alters the electromagnetic environment of the dipole in the InGaN QW and affects its spontaneous decay rate. This is possible if we consider that an atom in a cavity can be equivalent to a dipole emitter[129]. On that basis, the environment around the dipole can strongly affect its radiative properties, thus, the spontaneous decay probability can be enhanced or inhibited. This means that the spontaneous emission is not an intrinsic property of a luminescent material but the product of the interaction between the material and its local electromagnetic environment. Therefore, a change in the emitter's

environment can alter its emission rate and lifetime as it is described in the paper of Pelton[130]. This phenomenon, known as the Purcell effect[131], has been widely studied for c-oriented InGaN structures mainly via plasmonic effects[12],[13], with the use of metallic mirrors[133] or surface structuration[134]. The modification and control of the spontaneous decay has been studied in various photonic environments like photonic crystals[135], optical cavities[136] and nanowires[137] for several types of applications like semiconductor lasers[138], single photon sources[139] etc. Moreover, Drexhage showed in 1970 that the transition dipole moment can affect the decay rate of the dipole towards a planar interface[140].

Simulations from H. Chen et al.[119] on InGaN/GaN QW coupled with a metallic grating structure showed that the plasmonic coupling has a strong impact on the polarized emission, strongly associated with the LED performance in terms of modulation speed. On the theoretical side several approaches have been developed since Lukosz[114],[115],[141],[142],[143],[144].

II.3.1 Computational method for the calculation of the normalized spontaneous lifetime

In this section, we present our theoretical approach on the dipole orientation in a single QW (SQW) structure based on the spontaneous lifetime calculations near a planar interface of Novotny[115],[114] and Hecht[116]. We only take into account the optical properties of the GaN (cap layer)/air interface at the emission wavelength of the QW at 460 nm where the refractive indices are 2.4668 and 1 respectively.

Here, we will demonstrate that the variation of the emissive layer, i.e., the distance between the SQW and the top interface corresponds to different values of spontaneous lifetime (τ_{sp}). We assume that the harmonically oscillating dipole emitters are localized in the QW and that all their energy is converted into radiation. We also consider that the doping and the extremely small thickness of the InGaN/GaN QW are properties that do not affect the light propagation.

The way to mathematically describe the system[116] is derived from the electromagnetic theory of Maxwell. Having that in mind, the expression of the spontaneous decay rate near a planar interface follows:

$$\frac{P}{P_0} = 1 + \frac{\mu_x^2 + \mu_y^2}{\mu^2}\frac{3}{4}\int_0^{\infty} \mathrm{Re}\left\{\frac{s}{s_z}\left[r^s - s_z^2 r^p\right]\exp(2ik_1 z_0 s_z)\right\} ds + \frac{\mu_z^2}{\mu^2}\frac{3}{2}\int_0^{\infty} \mathrm{Re}\left\{\frac{s^3}{s_z} r^p \exp(2ik_1 z_0 s_z)\right\} ds \quad \text{(II.1)}$$

$$s = \frac{k_\rho}{k_1} \quad \text{(II.2)}$$

$$where: k_{\rho} = \frac{k_x}{\cos\varphi} \tag{II.3}$$

$$and\ \sqrt{1-s^2} = \frac{k_{z1}}{k_1} = s_z \tag{II.4}$$

Therein P/P_0 is the normalized energy dissipation rate of a radiating dipole caused by potential coupling with phonon, surface or waveguide modes over the initial radiative. Here, we take into account the dipole moments in the three directions: μ_x, μ_y, μ_z and r^s and r^p are the reflection coefficients that correspond to the s and p light polarization expressed as functions of a variable *s*. The latter is defined in equations (II.2) and (II.3) as the ratio of the wavenumber in cylindrical coordinates and the wavenumber that satisfies the dyadic Green's function's vector potential in a homogeneous, linear and isotropic medium (k_1) while k_{z1} in Eq. (II.4) corresponds to the longitudinal component respectively.

More specifically, in order to obtain the above Eq. (II.1), starting from the Maxwell's equations, the dyadic Green's functions are first used to describe a radiating single point source. Then, the angular spectrum representation of the dipole's field comes to expand the Green functions in plane and evanescent waves respectively in a cylindrical system. Now based on the above formula, this calculation can be applied to the interface of an InGaN/GaN SQW and air as it is presented in FIG. II.1. The simulation was performed by integrating over the 3-D space while the QW structure was considered 1-D as it is common in similar cases[144]. This means that only the direction vertical to the interface was taken into account, while the structure was assumed to be infinite in the other directions.

For an inhomogeneous environment, corresponding in our case to the QW, the energy dissipation of the dipole up to the interface with respect to the substrate [Eq. (II.1)] according to Novotny & Hecht is directly linked to its normalized spontaneous lifetime as:

$$\frac{\tau_{sp}}{\tau_0} = \frac{P_0}{P_{sp}} \tag{II.5}$$

, where τ_0 corresponds to the lifetime if the distance between the substrate and the interface is infinite. A similar approach has been also adopted recently by Mazuz-Harpaz *et al.*[145] for the study of excitons in double QWs.

II.3 - The impact of the photonic environment on the dipole orientation

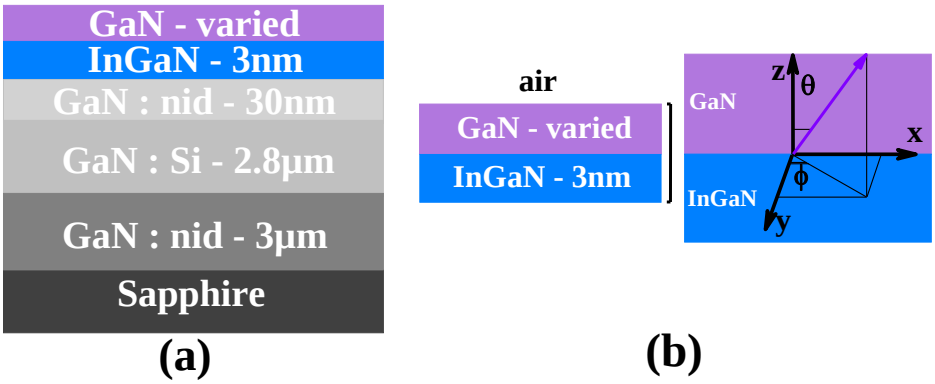

FIG. II.1. (a) Schematic cross section of the grown epitaxial structure. Where GaN:nid corresponds to non-intentionally doped layer with an electron concentration to be $n=1x10^{16}$ cm^{-3}. The equivalent one for GaN:Si is $n=3x10^{18}$ cm^{-3}. (b) The cylindrical coordinates (angle φ) that were used for the computation of the expansion of the plane and evanescent waves in the xy plane. Angle θ defines the angle of polarization. The refractive indices of GaN and air were taken into account for light emission at 460 nm.

In FIG. II.2 is depicted the graph that corresponds to the simulated normalized spontaneous lifetime values versus the distance of the QW from the interface for both the perpendicular and parallel polarization of the dipole (lines). It directly becomes clear that there is almost no variation of the lifetime with the distance from the interface when the dipole is in the plane of the InGaN/GaN QW.

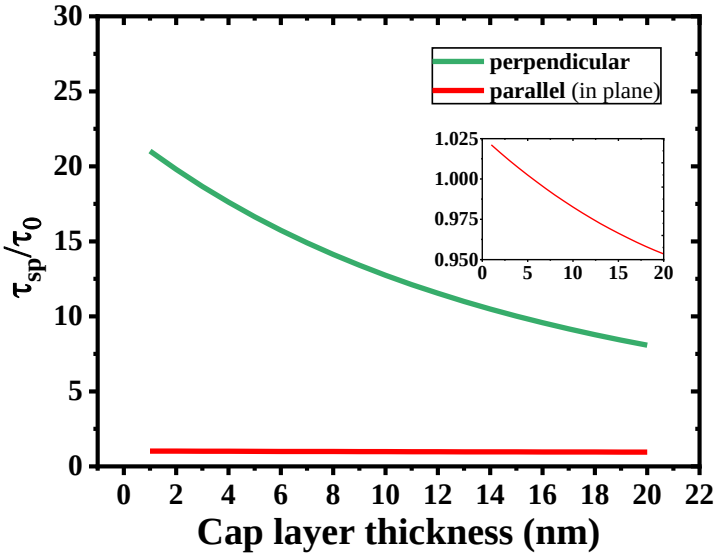

FIG. II.2. The simulated values of the normalized τ_{sp} as a function of the QW depth for the two options, dipoles placed vertically or horizontally with respect to the substrate. The inset is a close up of the parallel-in plane polarization.

On the contrary, when the dipole is normal to the QW, the spontaneous lifetime variation becomes significant and it increases with the decreasing thickness of the cap layer. For 5 nm, 8 nm and 12 nm cap layers, the simulated normalized τsp values were 16.64, 14.13 and 11.54 respectively for vertically polarized dipoles. In addition, it is worth mentioning that with a distance of 1 nm, the lifetime value that corresponds to the vertically polarized dipoles was calculated to be 20 times higher than the one for the horizontally oriented.

II.3.2 Experimental method for the extraction of the normalized spontaneous lifetime

In order to experimentally investigate the anisotropy of the dipole orientation in a single InGaN/GaN QW structure, we measured the decay time after optical excitation with a pulsed laser. The lifetime measurements were performed using a picosecond laser diode head (LDH Series, Picoquant). The wavelength of excitation was 375 nm, the duration of the pulse was 50 ps with a repetition rate of 5 MHz for the pulsed operation. The maximum value of the optical power was measured to be 55 μW with a laser spot of 1μm diameter. The solid state photon counting detector (PDM series, Picoquant) had a peak photon detection efficiency of 49% at 550 nm and generated a TTL output pulse per detected photon. Its photon timing resolution FWHM was 70 ps. The laser pumping (PL and TRPL) took place from the top of the sample.

The measurements were performed on the three samples (at the same spot on each sample) at 295 K and at different optical excitation power values. Then, the time resolved photoluminescence data were fitted as a mono-exponential decay using the following formula: $I(t) = I_0 + e^{-t/\tau}$, where I corresponds to the number of photon counts, I_0 is a constant and τ the lifetime value.

The mono-exponential decays from which the lifetime values were calculated are depicted at the left-hand side of FIG. II.3 in logarithmic scale. The total duration for the acquisition was 120 s. The data treatment was performed with the Origin software and the mono-exponential equation that was used was the: $y = A_1 e^{\left(-\frac{x}{t1}\right)} + y_0$. To be noted here that bi and tri-exponential fits were also tested to ensure that the most accurate case is the mono-exponential.

The next step is the extraction of the spontaneous lifetime, which is basically the lifetime value at zero excitation power. For this purpose, for each sample we measured the lifetimes at four different power values: 5.5 μW, 13.75 μW, 27.5 μW and 55 μW (taking into account the limitations of our set-up) and then by just extrapolating the data at zero energy[146] we can obtain the spontaneous lifetime.

II.3 - The impact of the photonic environment on the dipole orientation

The formula that we used for the extrapolation was $y = Intercept + B_1 x + B_2 x^2$ where, the spontaneous lifetime is the value of the intercept i.e., the point of intersection of the polynomial curve with the lifetime axis, see FIG. II.3. (d-f). A similar method has been used elsewhere for the same purpose[146]. We preferred to use the square law instead of the linear as it follows better the experimental data (good error evaluation). The lifetimes from the time decay measurements at the four excitation powers and the spontaneous lifetimes calculated from the polynomial fitting as described above for the InGaN/GaN of 5, 8 and 12 nm are listed in Table. II.1.

Based on Eq. (II.5), we have to define the τ_0 value, which is the limit when the QW depth becomes infinite. In order to do that, we approximate the curve that is formed by the three values of the spontaneous emission for each QW depth after extrapolation. The mono-exponential decay fit is depicted in FIG. II.4 and the value of the spontaneous lifetime limit τ_0, is 6.74 ± 0.39 ns. Now the calculation of the normalized spontaneous lifetime τ_{sp}/τ_0 is straightforward, as we have all the parameters that we need.

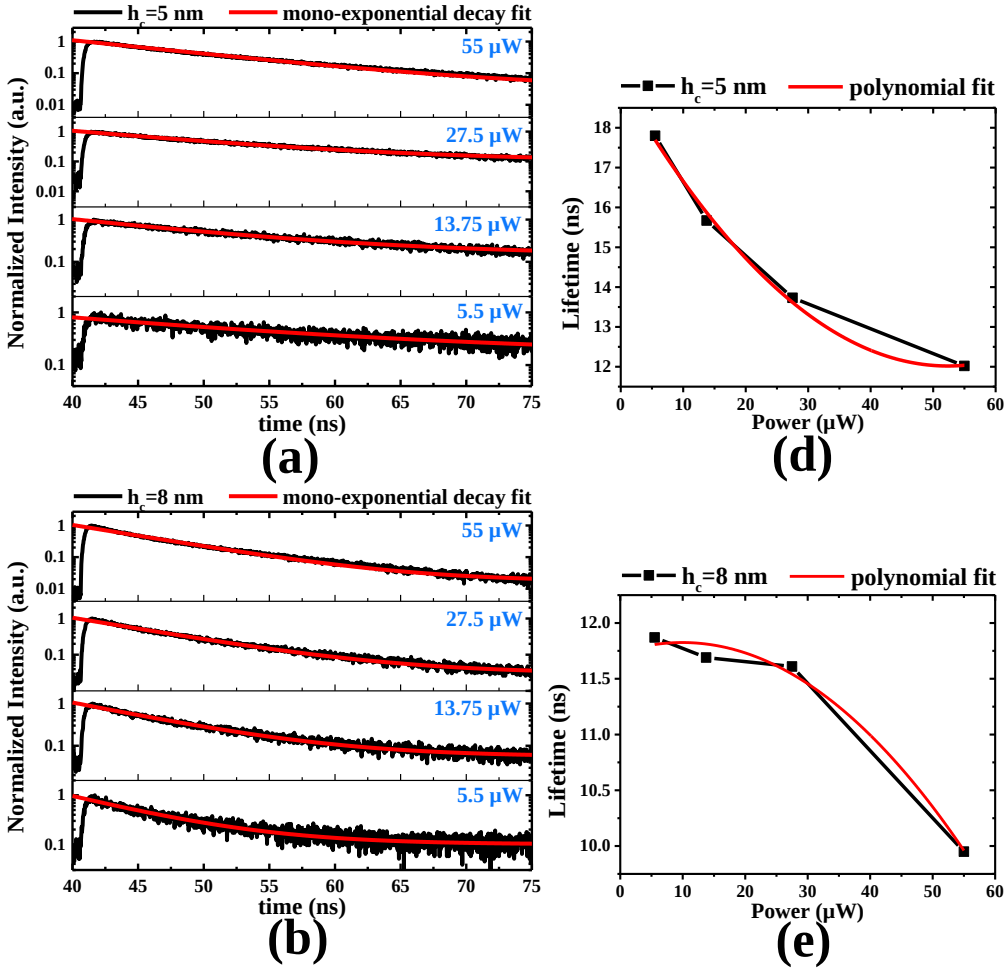

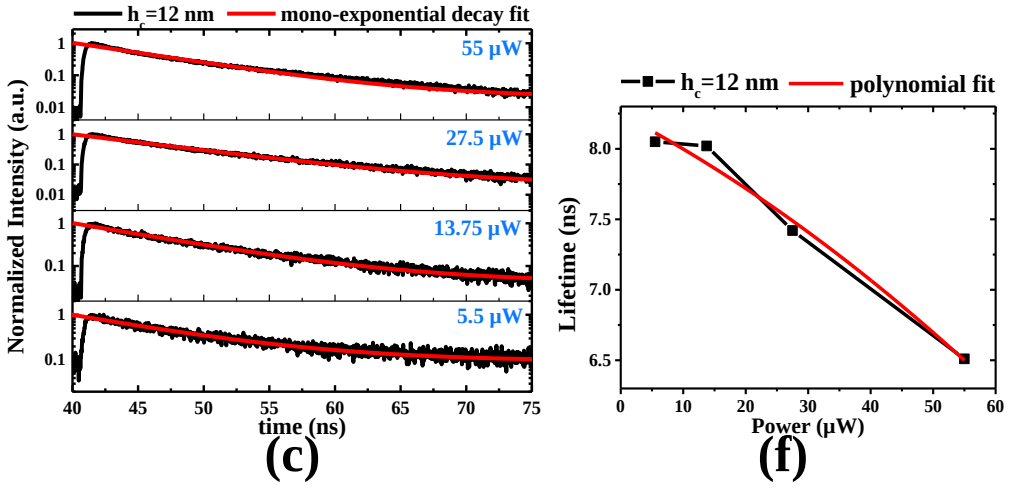

FIG. II.3. The logarithmic depiction of the time decay signal along with the mono-exponential fit for the InGaN/GaN SQW sample with (a) 5 nm (b) 8 nm and (c) 12 nm capping layer, for the various values of the excitation powers. On the right-hand side we see the polynomial fitting of the extracted lifetimes, from a, b and c, where the intercept corresponds to the value of the spontaneous lifetime. The measurements were realized at room temperature.

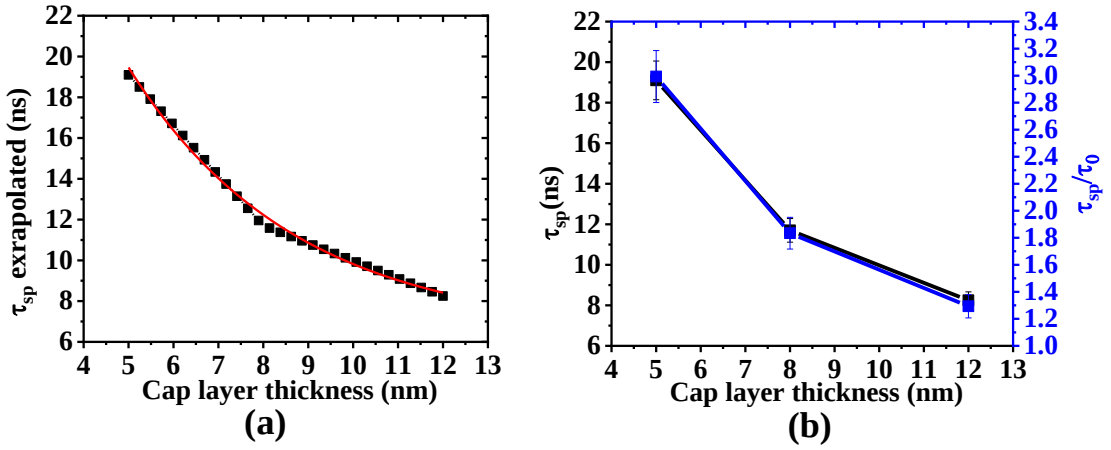

FIG. II.4. (a) The mono-exponential decay fit (red line) and (b) the spontaneous (τ_{sp}) and normalized spontaneous (τ_{sp}/τ_0) lifetime values for all the three InGaN/GaN capping layers.

h_c (nm)	5		8		12	
Power (μW)	**τ (ns)**	δ_τ (ns)	**τ (ns)**	δ_τ (ns)	**τ (ns)**	δ_τ (ns)
5.5	**17.8**	0.19	**11.87**	0.1	**8.05**	0.05
13.75	**15.67**	0.05	**11.69**	0.04	**8.02**	0.02
27.5	**13.73**	0.03	**11.61**	0.03	**7.42**	0.02
55	**12.02**	0.02	**9.95**	0.02	**6.51**	0.02
τ_{sp}	**19.1**	0.37	**11.7**	0.22	**8.25**	0.22
τ_{sp}/τ_0	**2.83**	0.19	**1.74**	0.12	**1.22**	0.09

Table II.1. The values of the lifetimes, the spontaneous lifetimes and the normalized spontaneous lifetimes for the three cap layers.

It is observed that the spontaneous lifetime strongly varies with the position of the QW. Similar to what we obtained from the simulations in the case of vertical dipoles, the highest values of spontaneous lifetime correspond to the structures with thin cap layer. Both results are presented in FIG. II.5. In average, the lifetime difference is more than twice as much in the case of the 5 nm compared to the 12 nm QW depth. This is of the same order, and even higher than the variation observed on the simulation curve corresponding to vertical dipoles, where the normalized lifetime varies from 16.64 to 11.54 for 5 nm and 12 nm QW depths, which gives a ratio of 1.44. This shows the substantial impact of the top interface on the carrier recombination dynamics, and the relative importance of the vertical dipole's population in the case of the thinnest cap layers. The difference in the values of the normalized spontaneous lifetimes between the simulation and the experiment can be explained by the fact that both the perpendicular and parallel components are represented in the same curve for the latter. The experimental results of the normalized spontaneous lifetime are presented in FIG. II.5 (squares).

II.3.3 Percentage of vertical dipoles in the InGaN /GaN: the α coefficient

Penninck *et al.* have presented a method to determine the degree of orientation of emitters by measuring the luminescent decay signal[147]. Their method is based on the dependency of the exciton decay rate on the optical environment and the orientation of the dipole transition moment. In summary, the total decay rate Γ_{tot} of the dipoles is the sum of the radiative and the

non-radiative decay rates. The radiative decay rate is given by Fermi's golden rule, which depends on the operators of the transition dipole moment and the electric field. Now, as it was analysed above, we can do the transition to the classical electromagnetic theory as the decay rate is proportional to the normalized power. And if we describe the power emitted by dipole antennas of different orientations in a microcavity as plane waves is possible to extract the percentage of the dipoles that are aligned vertically with respect to the substrate.

In this case, the constant α expresses the percentage of vertical dipoles in the QW and can be calculated by the following equation taking into account simulated and experimental data:

$$\Gamma_{tot} = [\alpha F_{ver} + (1 - a)F_{hor}]\Gamma_{r0} + \Gamma_{nr} \quad \text{(II.6)}$$

, where the rest of the variables carry information associated to the three different QW depths studied here. More specifically Γ_{tot} corresponds to the total decay rate of spontaneous lifetime, Γ_{r0} is the limit for an infinitively thick cap layer and Γ_{nr} expresses the contribution of the non-radiative decay that in our case is considered to be negligible. That means, that Γ_{tot} and Γ_{r0} are equal to the inverse of τ_{sp} and τ_0 respectively, while the value of Γ_{nr} is zero. Then, F_{ver} and F_{hor} are based on the simulated results for the values of the normalized power emitted by the electrical dipoles in the two directions for the three cap layers (FIG. II.2). Therefore, we can then easily proceed to the calculation of the $\boldsymbol{\alpha}$ coefficient from the above equation. The results can be found at Table. II.2 that follows.

$\mathbf{h_c}$ (nm)	α
5	0.69
8	0.46
12	0.22

Table II.2. The values of the $\boldsymbol{\alpha}$ coefficient for the three QW depth values: 5, 8 and 12 nm.

II.3.4 Discussion

Using the above model (Eq. II.6), we see below in FIG. II.5 the impact of the cap layer thickness on the dipole orientation in the QW. It appears that there is a preferred orientation depending on the separation between the QW and the interface. Therefore, when the latter is 5 nm, the majority of the dipoles, at a percentage of 69% at room temperature, are aligned vertically with respect to the substrate. That percentage appears to strongly decline with the

increase of the QW depth. As a comparison, for the cap layer of 12 nm this value drops down to 22%. According to our calculations, a cap layer larger than 7.5 nm implies that the majority of the dipoles in the QW are horizontally aligned. As a conclusion, in the 5 nm cap layer structure, the majority of the dipoles are perpendicular to the substrate, which corresponds to longer lifetimes compared to the case of the 12 nm or even the 8 nm cap layer, where the majority of the dipoles are aligned parallel with much shorter lifetimes. More experiments at low temperature - which is more representative of radiative recombination - confirmed the tendency we observed for the normalized spontaneous lifetime and the α coefficient is similar at 5 and 100 K. The equivalent graphs FIG. A.1 can be found in the Appendix at the end of the manuscript.

The experimental points in FIG. II.5 show a tendency that at least qualitatively is described by both perpendicular and parallel polarizations. This means that the increased normalized spontaneous lifetime is therefore possibly affected by the higher number of vertical dipoles (in comparison with the horizontal ones) lying in the QW when the cap layer is thin enough.

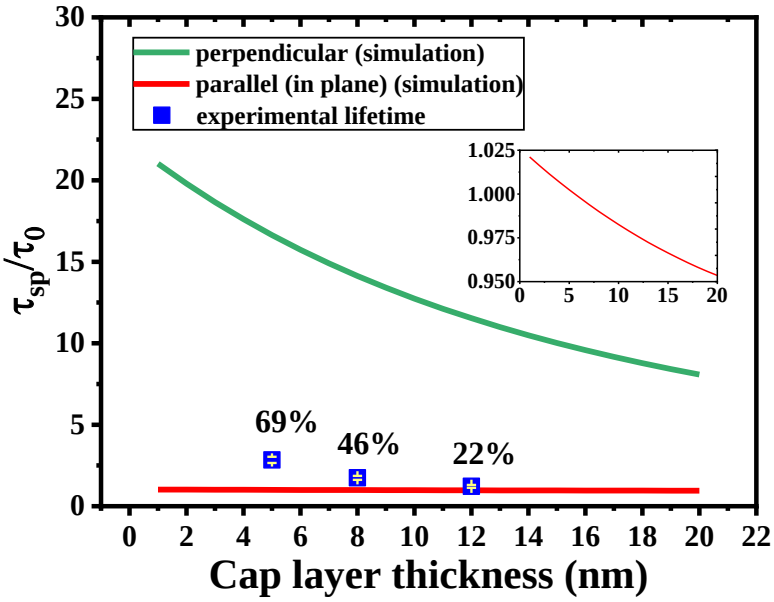

FIG. II.5. The simulated (lines) and experimentally obtained (squares) normalized spontaneous lifetime values variation for 1-20 nm cap layer thickness. Above the experimental spontaneous lifetimes, the percentages of vertical dipoles have been noted (α coefficient). The inset is a close up of the parallel (in plane) polarization.

As it was mentioned in a previous section, in the frame of QW-QD interaction the QDs are polarized correspondingly to the polarization of the QW emission. Then, as a matter of fact the

coupling efficiency and subsequently the color conversion efficiency strongly depend on the QW dipole orientation.

II.4 Detection of polarized light emission from the sidewalls

Previously we tried to understand the effect of the GaN/air interface when the InGaN/GaN SQW is situated at a nanometric vicinity on the dipole orientation. This is a special case and thus, our results are opposed to the general assumption that the dipoles in an InGaN QW configuration (where the QW are grown deeper from the GaN/air interface) lie parallel to the substrate.

Masui *et al.* in 2008 managed to measure the light emission from the sidewalls of polar InGaN based LED[148]. He showed that for sidewall emission in blue and green LED, the emitted light is highly polarized with ratios that can reach a value of 0.9 in the plane of the quantum well in agreement with other works on the same topic[149],[150],[151].

Using the approach of Masui *et al.*[148], in our recently published work[152] we studied the light emission from the sidewalls of our three samples with GaN cap layer of 5, 8 ad 12 nm in terms of polarization. In other words, the goal of this work was the characterization of the polarized light that is emitted by a QW located near the top surface of a GaN LED. In order to compare with Masui's work, we afterwards used a multi-QW (MQW) reference sample where the MQW are deeply buried at 300 nm below the top surface. Although he did not specify the quantum well positioning relatively to the surface in their publication, these values were found to be around 150 and 200 nm in other references from the same author[149], [151]. Considering this result, the agreement with the other studies[149],[150],[151] and the fact that it was a commercial LED, we will suppose that the QW were deeply buried at depth values from 150 nm to 200 nm, or maybe more.

For our experiment we use a confocal microscope associated with a rotational polarizer to measure the emitted sidewall light with the only difference that instead of electroluminescence, we use photoluminescence (or confocal fluorescence) to excite the active region. The equipment that was used was a WITEC - Alpha 300 confocal microscope. The wavelength of the laser excitation was at 405 nm. The maximum power was measured to be 120 mW with a laser spot of 500 nm diameter. The excitation power was calibrated with a power meter and ranged from 2 to 16 µW. The emitted light was detected by an Avalanche Photo Diode (SPCM-AQR Perkin Elmer) through the confocal microscope. All the measurements were performed at room temperature.

FIG. II.6. (a) presents a 3-D schematic of the system's configuration. The measurements were performed with the polarizer to be placed either parallel to the quantum well or perpendicular, at 5 μm depth under the sidewall surface. In addition to that, the confocal detection at this distance from the sidewall ensured that the emitters which are localized inside the QW were mainly influenced by the GaN/air interface, rather than that of the sidewall.

Then, at FIG. II.6.(b) we can see an image of our structure's sidewall - the view of the confocal microscope. The excitation laser spot with a diameter of 500 nm near the GaN/air (top) interface, the blue global luminescence generated by the laser pump and the blue emission trace scattered mainly in the sapphire can be also clearly distinguished.

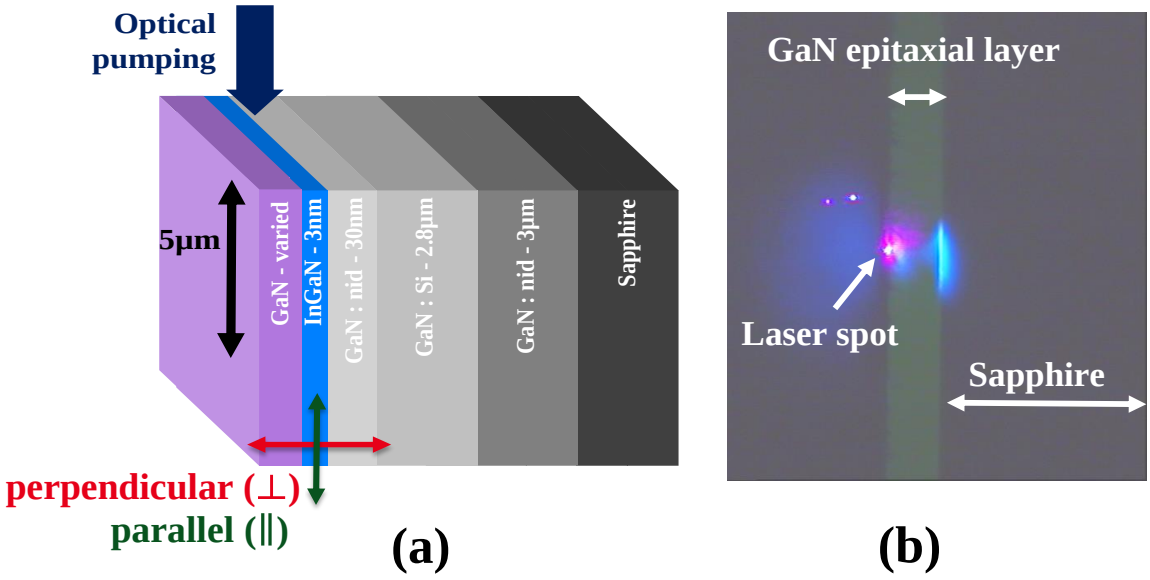

FIG. II.6. (a) The experimental configuration of the sidewall pumping at 5 μm depth and (b) picture of the sidewall where we can clearly see the laser spot close to the GaN/air (top) interface. The measurement is performed along the current point of a 1 cm long sample.

II.4.1 Emission spectra and polarization ratios in the spontaneous regime

As a first step, polarized emission spectra and polarization ratios were evaluated at decreasing excitation power from 16 to 2 μW. We can see from the emission spectra for decreasing excitation powers below in FIG. II.7 that the polarized emission is not the same in the two directions. It is clear that the emission parallel to the QW is always higher that the perpendicular one. Therefore, we can only conclude that the polarization of the total emission that is detected is basically the polarization parallel to the quantum well plane.

II.4 - Detection of polarized light emission from the sidewalls

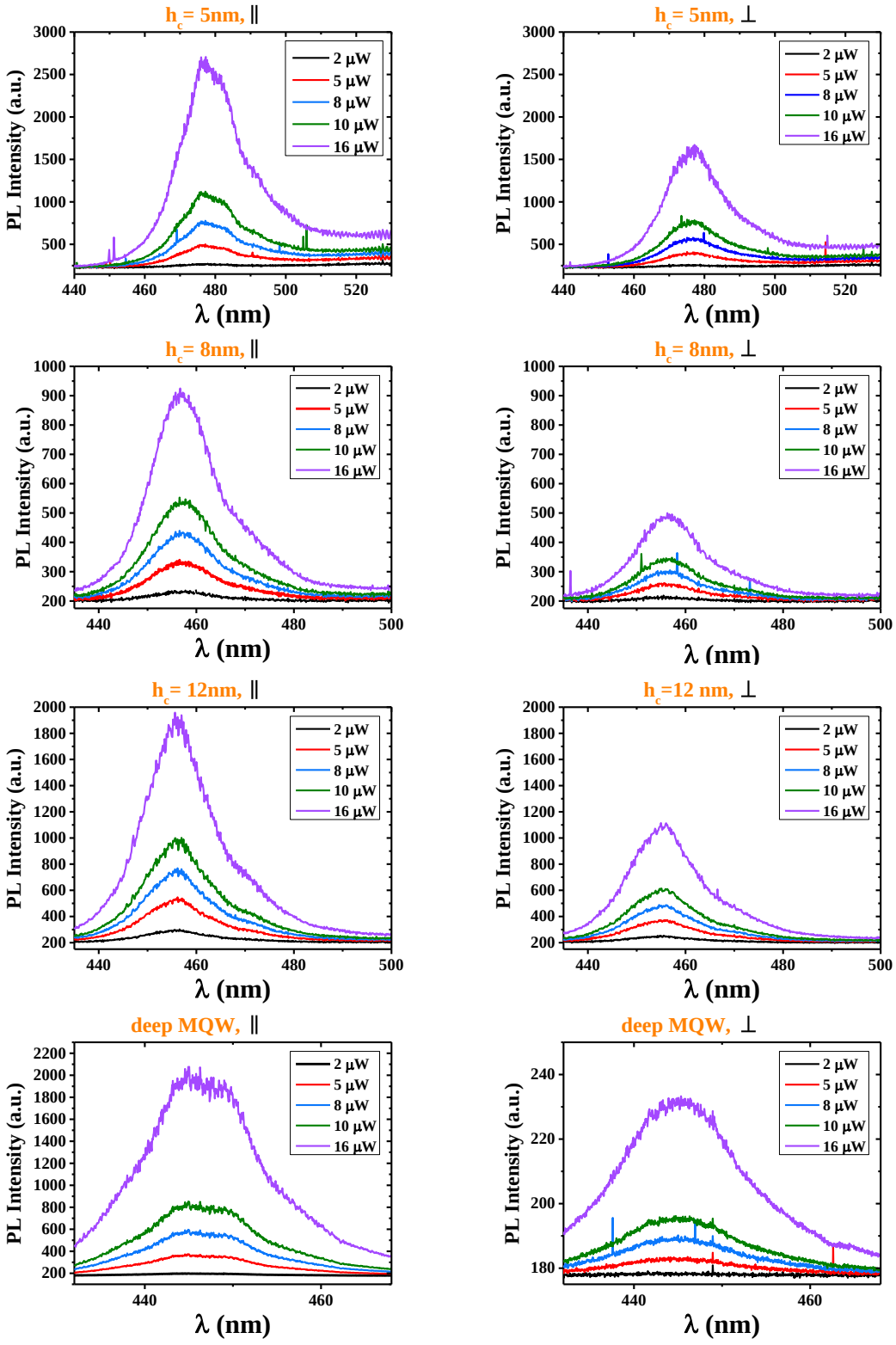

FIG. II.7. Fluorescence emission spectra for the three SQW samples with h_c of 5, 8, 12 nm and the reference deep MQW at various excitation powers with polarizer parallel (||) and polarizer perpendicular (⊥).

II.4 - Detection of polarized light emission from the sidewalls

Now, we can calculate the polarization difference ratio in two different polarization directions, which is defined by the following formula[148]:

$$\rho = \frac{I_{\max} - I_{\min}}{I_{\max} + I_{\min}} \tag{II.7}$$

, where the parameter ρ is commonly used to characterize the degree of optical linear polarization while, I_{max} and I_{min} correspond to the maximum and minimum detection intensities respectively. In our case, we obtain the maximum intensity when we place the polarizer parallel to the QW plane and the minimum when we place it perpendicular to it. The polarization ratios versus the excitation power are presented in FIG. II.8.

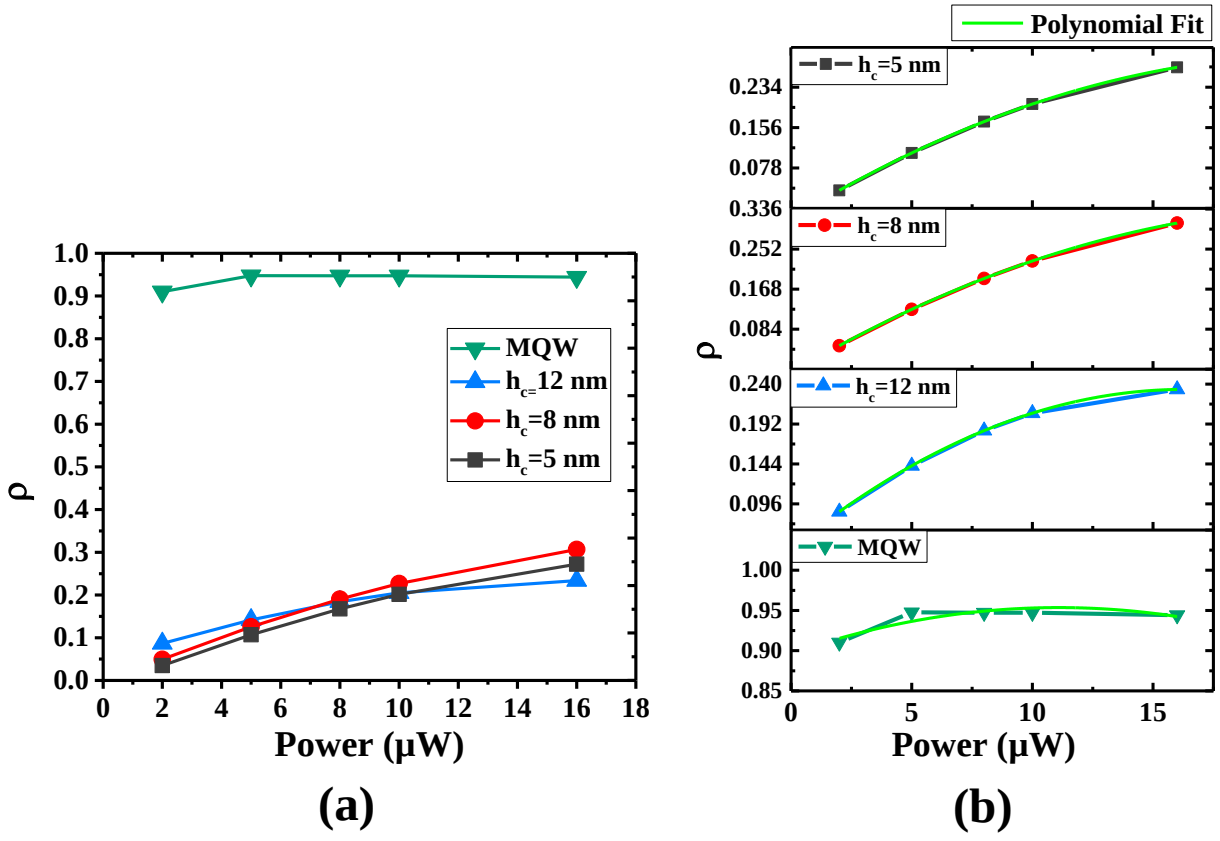

FIG. II.8. (a) The polarization ratios versus the excitation power for the four samples of 5, 8, and 12 SQW and the MQW along with (b) the polynomial fit.

In FIG. II.8. the calculation of ρ clarifies and quantifies the relation between the intensities that is not easy to do from the simple comparison of the spectra at FIG. II.7. The measurement of the reference sample (300 nm cap layer) returns the value obtained by Masui to around 0.9. Moreover, this value does not change when the excitation energy decreases. The polarization

ratios that correspond to the three SQW samples decrease from around 0.25 to 0.05 with decreasing excitation power. Moreover, the order for the three samples is different for low and high energy excitations. It is interesting that at low energy excitation, we obtain polarization ratios that are inversely proportional to the quantum barrier value.

In order to obtain information that is more fundamental, we once again explored the emission at very low excitation power. By extrapolating the experimental values at zero excitation power - similarly to the procedure we followed in the section II.3.2 - we are able to determine the polarization regime in spontaneous emission ρ_{sp}. We present the polynomial fit of the four curves at FIG. II 8 and the values of the spontaneous polarization ratio in Table. II.3. The excitation power was the lowest possible so that we have an acceptable signal to noise ratio. As we study the spontaneous emission, we should be as close as possible to zero excitation power.

$\mathbf{h_c}$ (nm)	ρ_{sp}
300	0.896
12	0.0426
8	-0.0078
5	-0.0198

Table II.3. The values of the polarization ratios calculated for the spontaneous regime.

The values of the ρ_{sp} are very low, while they even become negative for very thin quantum barriers (5 and 8 nm) in the spontaneous regime. There is no preponderance of parallel polarization in this configuration. At $\rho = 0$, the emission could be considered isotropic, in the focal plane. Even more, in spontaneous emission for the extrapolated negative values, it suggests that the polarization could be perpendicular in majority.

II.4.2 Discussion

As Masui *et al.*, we obtained complete spectra for each one of the four samples and the dependence on the polarizer orientation for a variety of excitation powers. Our results expressed in polarization ratios show, that near dielectric interface the polarization ratios are lower than 0.1 at low power excitations meaning a quasi-isotropic polarization of the emitters. Moreover, it appears that the proximity of the top surface of the LED with the SQW at a few nanometers affected the polarization ratios in a fundamental way.

In terms of experimental methods, our observation is based on pure confocal fluorescence which can be considered less perturbed by guided modes than the electroluminescence used by Masui. In fact, the emission is localized at the intersection of two perpendicular planes, the focal plane (thickness around 500 nm) and the SQW (thickness 3 nm). On the contrary, the electroluminescence activates light overall dye surface (350x350 μm) and in several quantum wells, creating multi reflections and guided modes. In this connection, we can notice that the electric power used by Masui is in the same range, voltage of 2 or 3 V and electrical current of 1 mA, meaning 0.002-0.003 mW, similar to our pumping power. A part of these modes can be detected through the pinhole of the device fact that affects the polarization of the detected light. In our case, the emission is created in a very small zone around the single QW and because we have less parasitic light, we can estimate that our polarization ratio is more representative of the dipole emitter orientation, acknowledging in parallel the probability of the dependency of the dipole emission on the density of states.

II.5 Conclusion

Both the theoretical approach and the performed measurements point out the strong impact of the nanometric interface proximity on the polarization ratio and consequently on the orientation of the emitting dipoles in an InGaN/GaN SQW. The thickness of the cap layer creates the conditions that define the direction of the polarization and it forms a connection between the normalized spontaneous lifetime and the dipoles' alignment in the QW. Then, from our results, we can suggest that the perpendicular polarization of the carriers in the QW can be correlated to the dipole orientation of the emitter. We also demonstrated that, this orientation phenomenon is inversely proportional to the QW distance from the interface. This outcome suggests that the position of the QW near the interface can strongly affect the energy transfer mechanism as it modifies the orientation of the donor - the role of the InGaN QW in the near field coupling. Having in mind that the polarization of the donor induces the same type of polarization at the acceptor we have two cases: the QW-QD dipoles are either parallel or collinear to each other and according to the NRET theory that can affect their coupling distance. This is a factor that should be taken into account when the QW is placed near the top surface of the color conversion LED to enhance the non-radiative energy transfer as the donor-acceptor configuration deeply modifies the polarization of the light emission. This leads to the conclusion that the polarization is a physical parameter of great importance that should be taken into account when it comes to the design of the devices that can produce high performance

RGB InGaN based micro-LEDs. As an extension, this effect can be considered in the case of QWs interacting with any other active medium placed on the top surface and in close proximity.

Chapter III - Study of the long range NRET between a single InGaN/GaN QW and CdSe QDs

III.1 Introduction

The purpose of this chapter is the study of the interaction between a single InGaN/GaN QW and colloidal red quantum dots in the near field for color conversion applications. Based on the FRET (or NRET) theory for isotropic media, we try with this work to decipher the nature of this kind of interaction by investigating the limits of the near field coupling in a non-isotropic configuration. For that reason, the main parameter that we consider here is the donor-acceptor physical distance.

At first, we have already seen that the non-radiative energy transfer rate decays rapidly ($\sim R^6$) with the donor-acceptor distance. Moreover, as it was analyzed in the general introduction, the theoretical calculations state that the so-called Förster distance (R_0) of the pair of donor and acceptor, i.e., the distance at which the energy transfer efficiency is 50%, is 10 nm for homogeneous media.

For this reason, we initially chose the QW-QD separation to be 5, 8 and 12 nm in terms of GaN cap layer thickness. Nevertheless, since the media involved are inhomogeneous and non-isotropic, after the first set of experiments, a SiO_2 spacer (25, 50, 75 and 100 nm) was deposited above the GaN cap layer in order to increase the distance between the QW and the QDs. Therefore, along with the search for the optimal distance that will maximize the NRET efficiency, we simultaneously investigate the performance of the energy transfer in the long-range coupling. The NRET efficiency is calculated from experimental data based on photoluminescence excitation power and time decay measurements.

The final objective will be to estimate the performance of a GaN based LED, fabricated to operate in the near field, which uses QDs as the color conversion layer.

III.2 Long-range NRET across heterogenous interfaces

The parameters that can affect the NRET across heterogeneous interfaces are yet not well known, and the effects of the various material and structural characteristics remain weakly - or not at all - explored. In the bibliography, one can find several results concerning the NRET long-range coupling in inorganic systems very different from ours. The NRET from excitonic donors to metallic acceptors has been studied extensively, and always results in efficient long-range quenching of fluorescence because of the very large plasmon resonance of the acceptor dipole[153],[154],[140]. Long-range NRET can also occur between molecules (or QDs) and two-dimensional material acceptors, such as graphene or TMDC monolayers. Experimental results have revealed a weaker distance dependence compared to the conventional point-dipole

Förster transfer, owing to the large oscillator strength and delocalization of the electronic excitation[155],[156],[157].

III.3 Designs for short and long-range NRET between InGaN/GaN QW and CdSe QDs

One of the major goals of this work and at the same time, the main purpose of this chapter is the investigation of the InGaN / GaN-QD NRET based excitation configuration. The necessity of a nanometric donor-acceptor distance for NRET in order to manifest can lead to an alternative micro-LED design.

The distance between the donor QW and the acceptor QD - or in other words the GaN cap layer - is varied among 5, 8 and 12 nm, see FIG. III.1.(a). These values seem to fit well the theory of the near field coupling, where the optimal distance in the case of homogeneous media was calculated to be 10 nm.

Now, in this work red CdSe QDs play the role of the down converter. The QDs are mixed with PMMA, anisole and toluene in a chemical solution, whose composition is confidential. The red emission of the QDs can be seen in the picture of FIG. III.2.

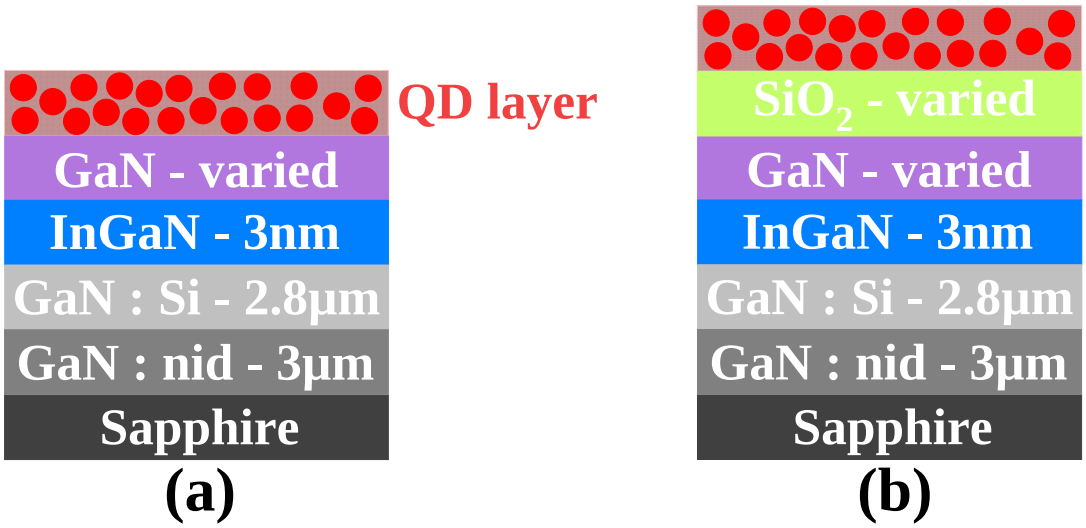

FIG. III.1. The two structures that were used for the study of the (a) short-range QW-QD coupling where the QD layer is deposited on the GaN cap layer and (b) long-range coupling where a SiO2 spacer mediates between the GaN cap layer and the QDs in order to study the long range coupling and at the same time maintaining the same dipole orientation in the QW.

The deposition of the colloidal QDs was performed with inkjet printing (Dimatrix inkjet printer) and then it was let dry in air. Nevertheless, the thickness obtained was not fully

reproducible and the layers were not homogeneous, as the solution was not optimized for such a deposition as we can see in FIG. III.2.(b). In former studies it was demonstrated that it is the separation between the QDs and their size that directly affect the NRET, rather than the thickness of the layer they form[158],[159] as the electronic energy transfer in QDs arises from nearest-neighbor dipole-dipole interactions. In our case, we consider that the interaction between the QDs that are contained in the acceptor's layer is a secondary feature and in our case will be neglected[160].

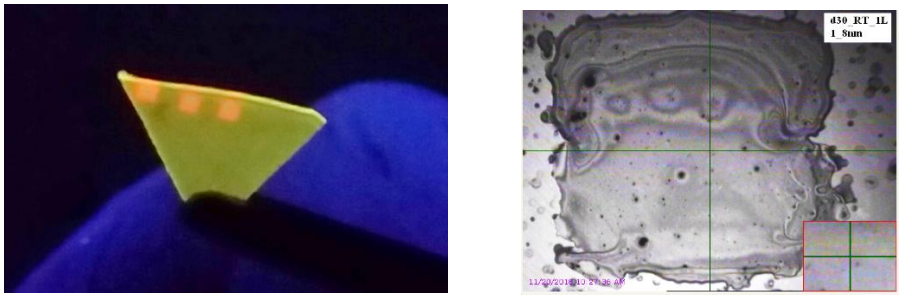

(a) (b)

FIG. III.2. The emission from the QD structures (squares) deposited on the InGaN/GaN structure as it is described in FIG.III.1. (a) when placed under the UV lamp and (b) the optical microscope's view of the deposited squares.

Now in order to study the long range NRET, a layer of SiO2, transparent in the blue range (where the InGaN QW emits) was deposited by plasma enhanced chemical vapor deposition (PECVD) on the top of the structure with thicknesses that again vary: 25, 50, 75 and 100 nm, see FIG. III.1.(b). Our PL experiment on the InGaN QW/ SiO2 spacer samples showed that the PL signal remained in the same spectral position compared to the PL of the bare QW. In addition, it is essential to point out the importance of the SiO2 spacer instead of simply having a thicker GaN cap layer made by MOCVD in the three layered structure. An inserted wide-bandgap spacer layer suppresses exciton quenching by direct charge transfer at the interface, whereas long-range energy transfer across the transparent spacer layer is still possible[161].

III.4 Optical properties of the structure

Photoexcited electrons and holes are strongly bound by Coulomb interactions (i.e., excitons) in planar QWs. This is due to a strong quantum confinement effect[162] that gives rise to a large exciton binding energy in InGaN quantum wells[163]. In our case, the InGaN thickness of only 3 nm (the Bohr radius is 3.4) can guarantee an excellent carrier confinement.

Time-resolved studies in hybrid quantum well heterostructures have demonstrated the effect of an extra decay channel in the quantum well emission (donor)[164],[165],[166]. However, as it is underlined in reference[167], this alone cannot be taken as evidence of energy transfer to the acceptor sites because the deposition of an overlayer (in our case the QDs in polymer layer), separating donor and acceptor sites could lead to modification of its surface states, which would itself modify the decay dynamics. Any changes in the photoluminescence decay of a quantum well in a hybrid structure can only be conclusively attributed to non-radiative energy transfer to the acceptor site if the effect of energy transfer is also observed directly in the emission properties of the acceptor. Thus, the evaluation of an effective NRET is achieved by monitoring the donor-acceptor emission intensity interplay or more specifically, the elevated intensity of the acceptor with the simultaneous decrease in the emission of the donor.

The optical measurements were performed in order to investigate the QW-QD coupling considering the two cases of the short-range near field coupling (up to12 nm) and long-range (up to 112 nm) coupling for the two structures described in FIG. III.1. In total the optical properties of 15 samples were investigated for temperatures varying between 10 and 300 K at 13.5 μW excitation power. The description of the PL and TRPL set-up can be found in section II.3.2. The PL and TRPL measurements took place at the same point for each sample. As in the previous chapter, the excitation also takes place from the top of the sample. In this case, the laser is not totally absorbed by the QW so only a part of the excitation will lead to the PL of the QDs.

III.4.1 Photoluminescence (PL)

The spectra of all our samples present the blue light emission of the InGaN QW and the red emission from CdSe QDs. The PL signal is displayed with interferences from the layers below. An example can be seen at FIG. III.3.(a). The Fourier transform (FT) processing of the photoluminescence spectrum is a very important tool as it allows us to correctly select the wavelength positions for the time resolved measurements (peak values).

III.4.1.1 Short range coupling (QW-QD)

In FIG. III. 3.(b) is presented the comparison of the PL spectra between the bare InGaN/GaN structure and the hybrid InGaN/GaN QDs, as a function of temperature. As an example, we used the type of structure in FIG. II.1.(a) with a cap layer of 8 nm. Indeed, with the deposition of the QD layer, the blue emission from the QDs quenches and at the same time the QDs emit

in the red. This phenomenon has already been discussed thoroughly in the literature in the frame of the energy transfer coupling[168],[169].

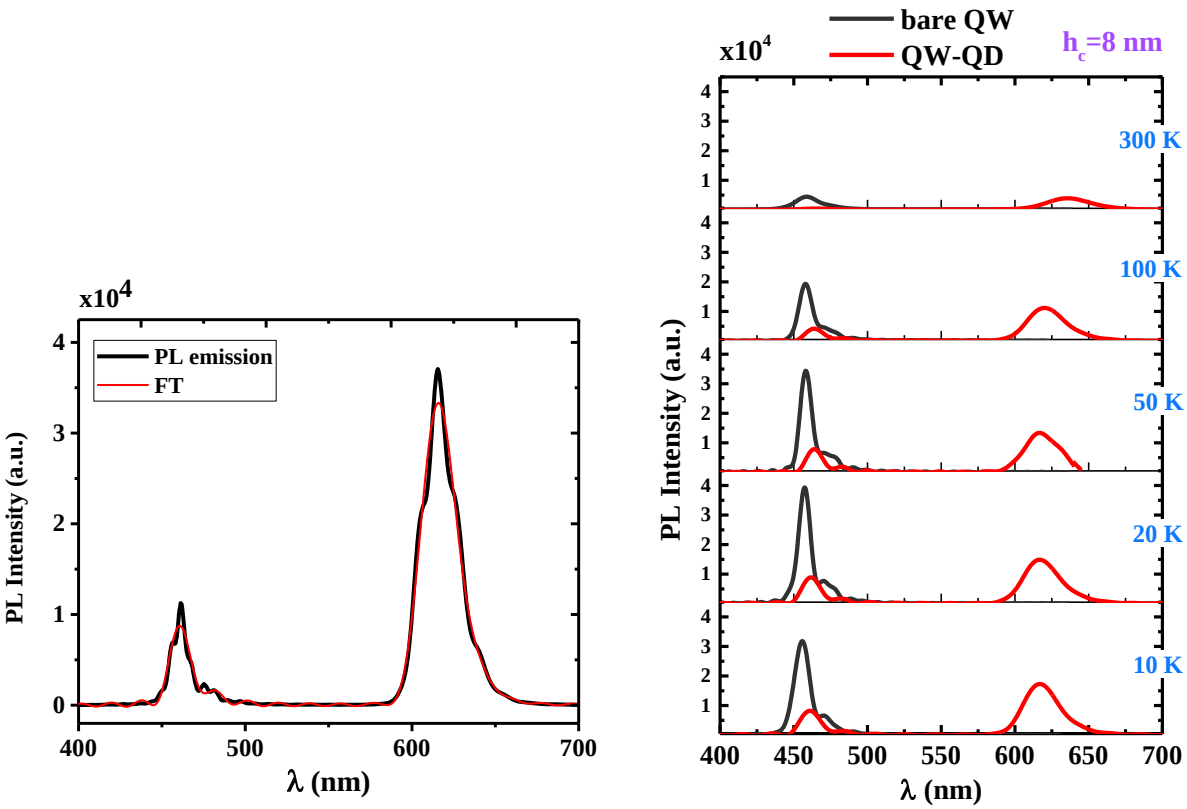

FIG. III.3. (a) An example of the emission spectrum of the InGaN QW and the QDs at 10 K and 55 μW excitation power. In black is the raw signal and in red the FFT fit. (b) A presentation of the evolution of the PL signal before and after the deposition of the QD layer for the sample of the 8 nm cap layer at temperatures that vary between 10 and 300 K and 55 μW excitation power.

III.4.1.2 Long range coupling (QW-spacer-QD)

In this chapter though, our main focus is the long-range QW-QD interaction and thus the impact of the SiO2 spacers thicknesses (25, 50, 75 and 100 nm) that increase the donor-acceptor separation. In FIG. III.4 are presented the PL intensity spectra that correspond to the (a) 5 nm, (b) 8 nm and (c) 12 nm cap layer InGaN-QD samples at 13.75 μW excitation power for temperatures varying between 10 to 200 K.

The signal is clearer for the sample with h_c=5 nm. Looking at FIG. III.4.(a), we can see that the intensity signal of the red emission (630 nm wavelength) when the thickness of the SiO2 spacer is h_s=75 nm obtains its highest value at all the temperatures. It is the decrease of the QW intensity along with the simultaneous increase of the QD emission that signifies that the NRET takes place and it is more productive with the 75 nm spacer than at the rest of the cases. For the

5 nm cap layer, this is happening at all temperatures. A clear comparison among the different spacers can be found in FIG.III.4 (d).

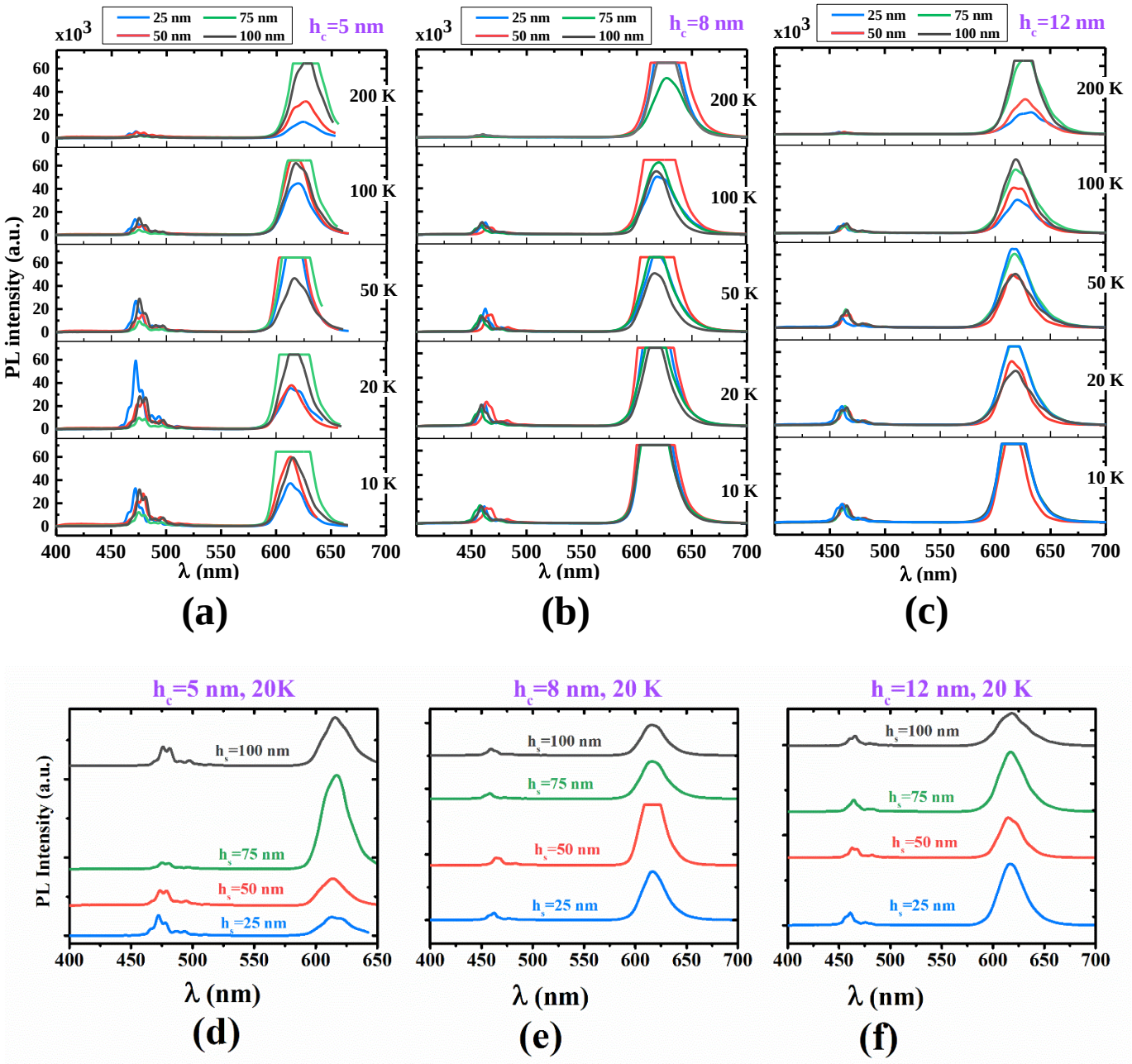

FIG. III.4. The PL intensity spectra that correspond to the (a) 5 nm, (b) 8 nm and (c) 12 nm cap layer InGaN-QD samples. The four thicknesses of SiO_2 spacers (25, 50, 75 and 100 nm) that were used to increase the QW-QD distance are presented in different colors for a variety of temperatures. The excitation power is at 13.75 μW. The PL intensity signal gets saturated above 60 x10^3 counts. As a close-up, the PL intensities at (d) 20 K for the 5 nm, (e) the 8 nm and (f) the 12 nm cap layer are presented.

For the case of 8 nm cap layer, the PL intensity signal at 630 nm is always higher for the 50 nm spacer. Nevertheless, the QW signal is really weak and therefore we cannot clearly observe the simultaneous increase/decrease of the QD/QW in the PL intensity at 20 K (FIG. III.4.(e) as in the h_c of 5 nm. Similarly, the PL intensity from the 12 nm cap layer (FIG. III.4.(f) appears higher when the spacer is 25 nm (mainly at 10-50 K). But again, it is difficult to evaluate the situation as the emission in the blue gets very weak. Although we can't comment on every single case separately, there is strong indication of NRET. Similar results were obtained in the rest of the cases where the excitation power is in the range of 5.5-55 μW.

It is worth to be noted that although the significant signal saturation in several cases in (FIG. III.4.a-c), we finally chose to present the results that correspond to the excitation power of 13.5 μW. The reason behind that is our intention to show coherent results as the TRPL was obtained under the same pumping conditions. We have also measured PL spectra at lower excitation power (5.5 μW). In that case, there is much less saturation compared to the PL measurements that are presented above but as a consequence, the donor's signal is much weaker which makes it difficult to conclude. The graphs can be found in the Appendix FIG. A.2.

III.4.2 Time resolved photoluminescence (TRPL)

In order to evaluate the coupling efficiency between the QW and the QDs, is important to distinguish and quantify the radiative and the non-radiative components. Indeed, both processes take part in the coupling with a certain probability.

For this purpose, we perform time-resolved PL (TRPL) experiments in the blue (emission wavelength of the QW~460 nm). As we saw in the previous chapter, the fit of the TRPL curves of the InGaN QW alone is mono-exponential. Now, when the QD layer is added, the decay in the blue is faster and the curve can be fitted with a double exponential. Consequently, the two lifetimes that correspond to the radiative coupling and the non-radiative processes[170] can be easily extracted. An example of two time decay curves before and after the deposition of QDs is depicted in FIG. III.5.(a) where we consider the case at 10 K and 55 μW excitation power of a sample with a 8 nm cap layer.

In the frame of the near field interaction, the double exponential fit provides a sufficiently good description of the QW decay dynamics in the presence of a QDs-in-polymer layer, similarly to the case of this study[171]. The decays are characterized by a short and a much longer time constant. More precisely, according to the reference[172] the QW decay in the presence of the conversion layer contains a fast exponential term and a non-exponential tail at longer times that contributes weakly on the average lifetime. From physical point of view, only

a transfer from the QW to the QDs takes place and the inverse situation is not possible when the structure is pumped. These two terms correspond to two lifetimes: a fast non-radiative and to a much longer radiative contribution $y = y_0 + A_{rad}e^{(-t/\tau_{rad})} + A_{NRET}e^{(-t/\tau_{NRET})}$. An indication of the probability or the weight of each of the two coupling mechanisms is the coefficient of the respective exponential (A_{rad} and A_{NRET}). In other works[173],[167] we see that the extraction of the efficiency is done in a different way, by separately taking into account the emission of the bare QW. Contrary to our case, the two values of the fitting coefficients of their bi-exponential fit are in a different range, which means that they consider only one of them in their evaluation of the energy transfer. However, in our case the values of the fitting coefficients are much closer, fact that makes it impossible to use the above method. This is why, apart from the extraction of the efficiency, we present as well the ratio of the fitting coefficients, in order to better support our arguments.

Moreover, in FIG. III.5.(b) is displayed the TRPL for the emission in the red, when the QD layer is deposited on the InGaN/GaN sample and on glass. The faster emission on GaN is an indication of an additional decay channel.

III.4.2.1 Short range coupling (QW-QD)

The TRPL measurements and their exponential fit for the short-range coupling are depicted in FIG. III.5. (c). The τ_{rad} and τ_{NRET} as a product of the bi-exponential are depicted versus the QW-QD distance for temperature values 5-300 K. We observe the product of the bi-exponential decay with the short non-radiative and long radiative lifetimes. The non-radiative lifetimes corresponding to the hc of 5 nm were calculated to be shorter than those of the 8 nm and the 12 nm cases although the difference is not very high. The table A.1 is added at the Appendix part at the end of the manuscript with the exact lifetime values (and uncertainties).

We can also see that the values tend to decrease with the increase of the temperature. The radiative recombination rate was calculated to reduce faster with temperature than the NRET rate so that the transfer rate becomes increasingly effective as the temperature is raised. This trend that was theoretically predicted for energy transfer from a InGaN QW to a colloidal quantum dot overlayer and attributed to a temperature-dependent competition between the transfer rate and the radiative rate in the InGaN QWs[173]. In addition to that, it is noted that, almost independent of temperature, the energy transfer rate is always higher than the radiative transition rate in the QW.

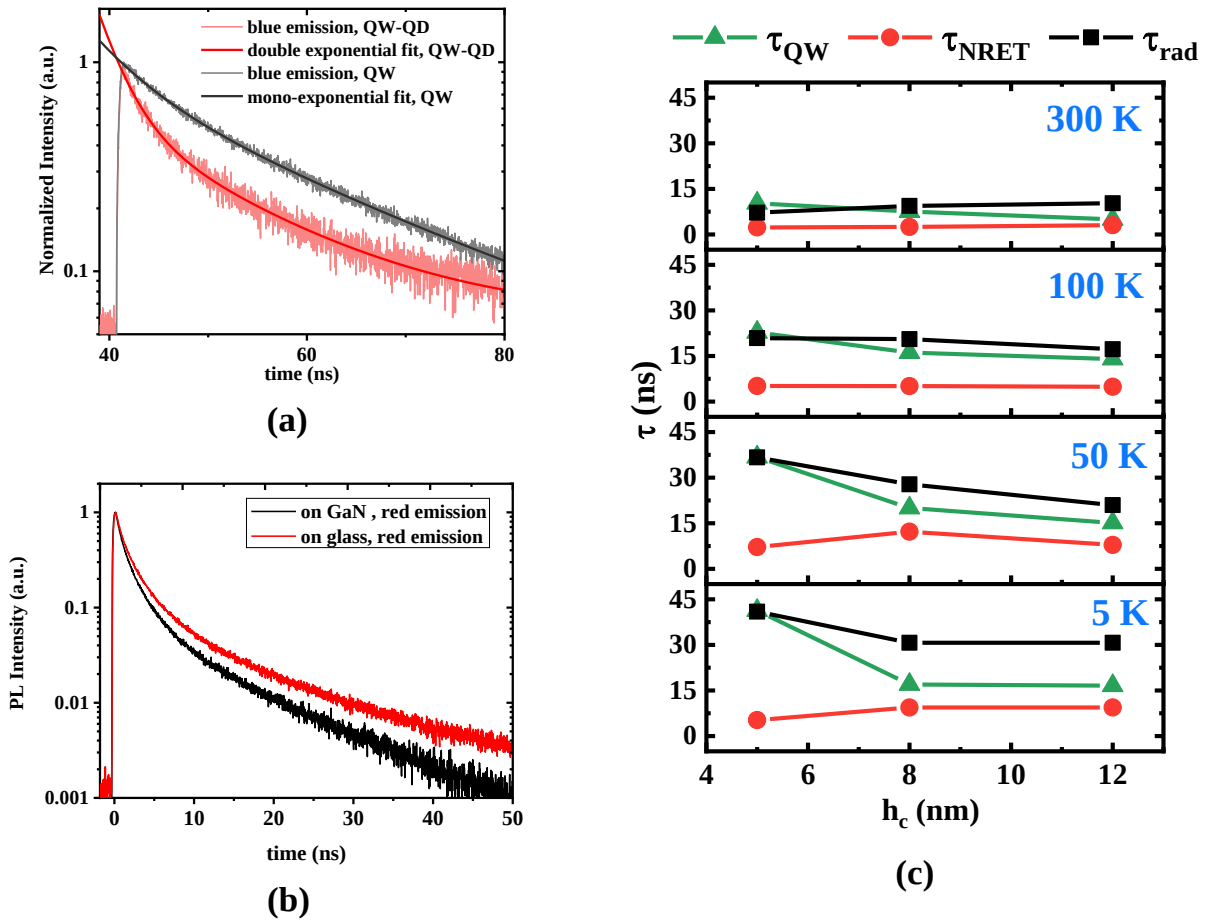

FIG. III.5. (a) From the time decay measurements in the blue range, the addition of the QD layer (red curve lower than the black one) leads to a faster decay[167],[174],[64]. The double-exponential fit of the red curve indicates the existence of two coupling mechanisms: The radiative and the non-radiative. The sample has h_c=8 nm and the measurement takes place at 460 nm at 55 μW excitation power at room temperature. (b) the TRPL measurement of the red emission on the InGaN/GaN samples and on glass. (c) The extracted lifetimes from the bi exponential and mono-exponential fit versus the cap layer thickness for the QW-QD coupling and the bare QW respectively.

III.4.2.2 Long range coupling (QW-spacer-QD)

Moving on to the long range coupling, the curves were once again successfully fitted with a double exponential and the lifetime values versus the coupling distance are presented in the graph that follows. This was an important step in this work as this type of fit was not evident for the long-range interaction. The remarks are similar to those of the short-range values that indicates a converging behavior. All the lifetime values are presented in the Appendix along with their uncertainties in table A.2.

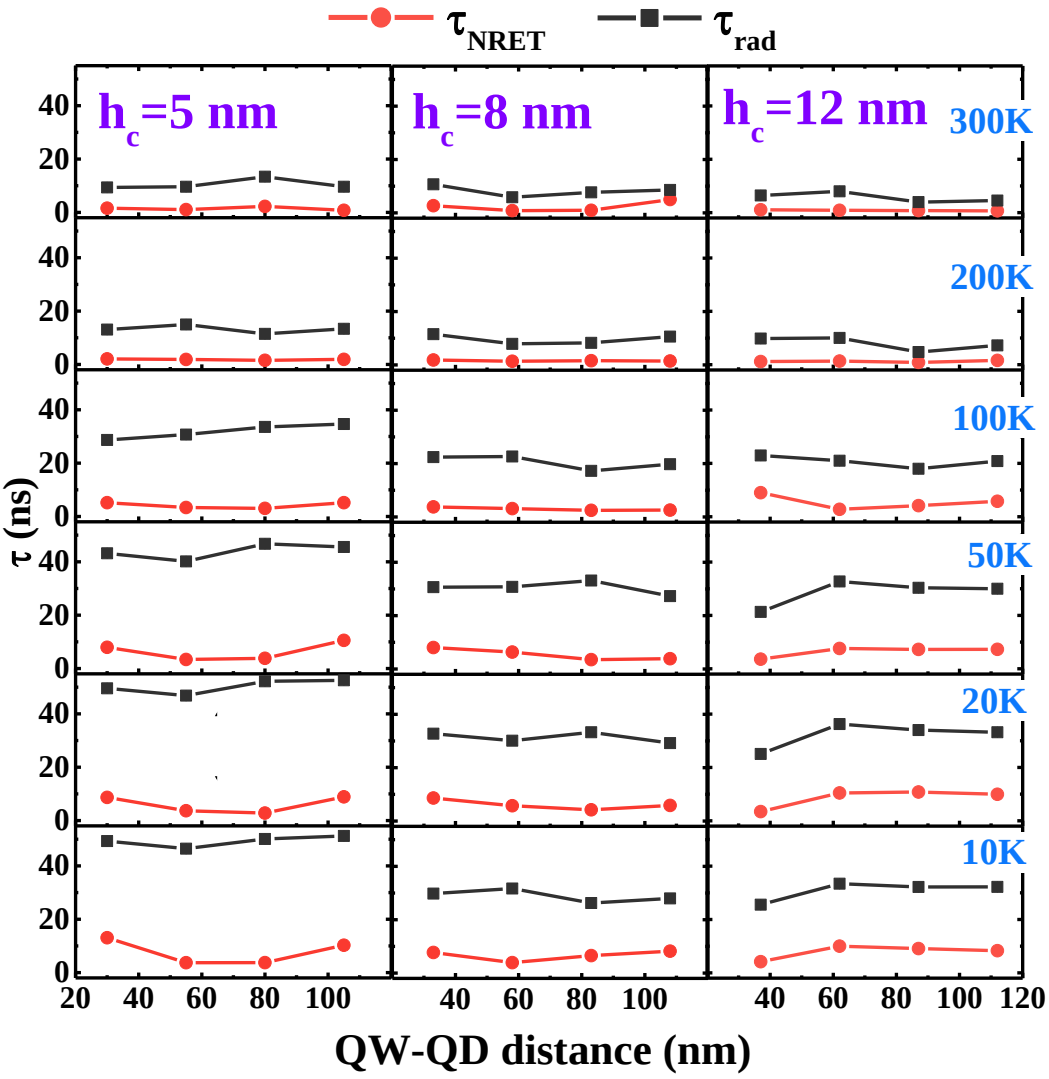

FIG. III.6. The radiative and NRET lifetimes as they were calculated by the bi-exponential fit versus the QW-QD distance. More specifically, at these graphs, the τ_{NRET} and the τ_{rad} are presented for each cap layer thickness at temperatures varying from 10 to 300 K at 13.75 μW.

Now, the lifetime extraction is the basis for the understanding of the coupling mechanisms between the QW and the QDs, but other than that it is difficult to conclude only based on this representation. For that purpose, it is necessary to evaluate the NRET efficiency.

III.4.3 Long range NRET coupling efficiency

The NRET efficiency can be estimated using the following relation[170]:

$$\eta_{NRET} = \frac{\tau_{NRET}^{-1}}{\tau_{NRET}^{-1}+\tau_{rad}^{-1}} \quad \text{(III.1)}$$

On top of that, the fitting coefficients of the bi-exponential of the NRET efficiency A_{rad} and A_{NRET} can also give an additional insight to the quantification of the QW-QD interaction.

The results of the efficiency calculation and the ratio of the fitting coefficients are presented in FIG. III.7 and III.8 respectively. The ultimate goal of this study is to understand under what circumstances and conditions such a system exhibits a highly efficient NRET.

The NRET efficiencies vary between 71 and 93%. In FIG. III.7 we clearly see the influence of the three cap layer thicknesses considered in our study, especially at low temperature, between 10 and 50 K. Among the three configurations, the structures with the 5 nm cap layer show a much more effective NRET coupling in a longer range than those of the 8 and the 12 nm, whose NRET efficiencies are generally lower, and peak when the QDs are placed closer to the QW. More precisely, the 5 nm cap layer leads to a NRET efficiency in high levels for QW-QD distances between 55 and 80 nm. This range is smaller for the 8 nm and the 12 nm cap layer as they only show one main peak in lower efficiency values. The 8 nm case presents its peak value when the QDs are either at 58 or at 83 nm distance, while the 12 nm obtains its peak value when the QW-QD distance is the shortest, at 37 nm. This means that there is a “high NRET efficiency window” for each cap layer for specific QD-QW distances that moves towards smaller values as the cap layer becomes bigger. Therefore, the smallest cap layer thickness seems to create the most suitable environment for an energy transfer coupling at long distance. More generally, there is always an optimal distance at which the η_{NRET} attains its maximal value for each cap layer thickness and temperature.

Concerning the higher temperatures of 200 and 300 K, it appears that the efficiencies are in the same range; that translates to a similar coupling behavior among the different cap layers regardless the QW-QD distance.

Another way to correlate the energy transfer with the radiative emission is the interplay of the fitting coefficients of the bi-exponential decay, which is presented in FIG. III.8. When the ratio is smaller than one, the energy transfer is the more pronounced contribution on the coupling.

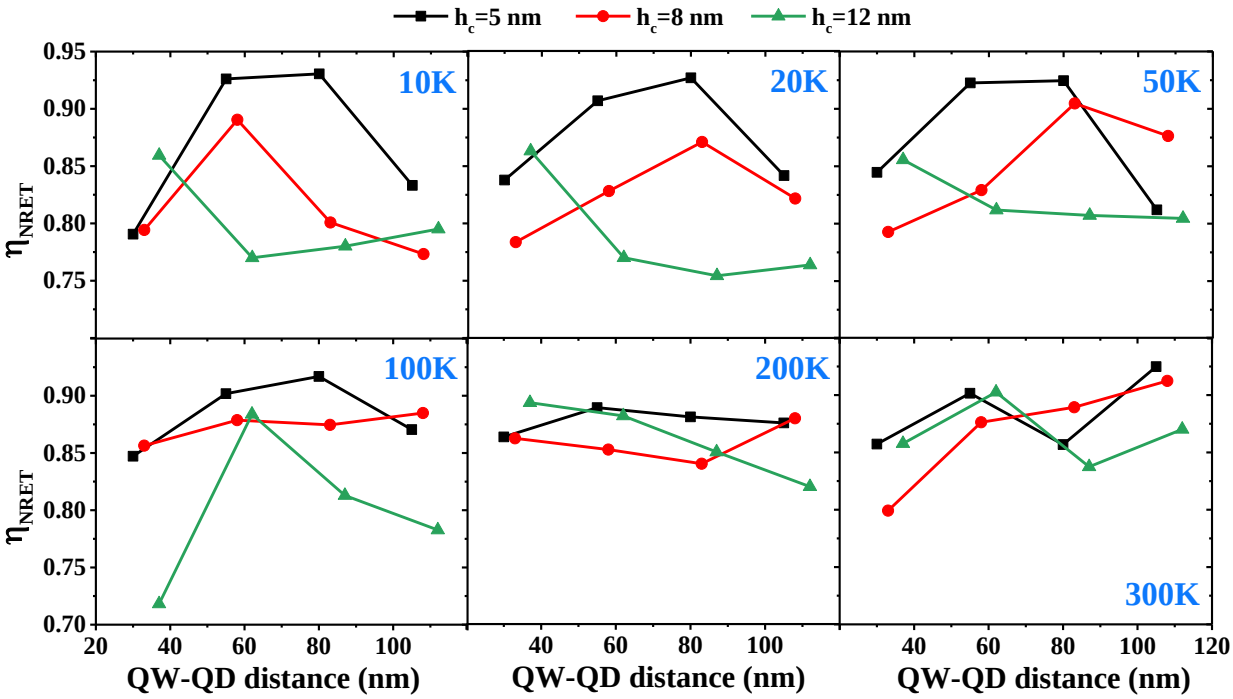

FIG. III.7. The NRET efficiency versus the QW-QD distance for the long-range coupling is presented in this graph. This calculation is originated from the lifetimes that presented in FIG. III.6 that were measured at 13.75 μW laser power. The impact of the temperature and the cap layer thickness can be noticed.

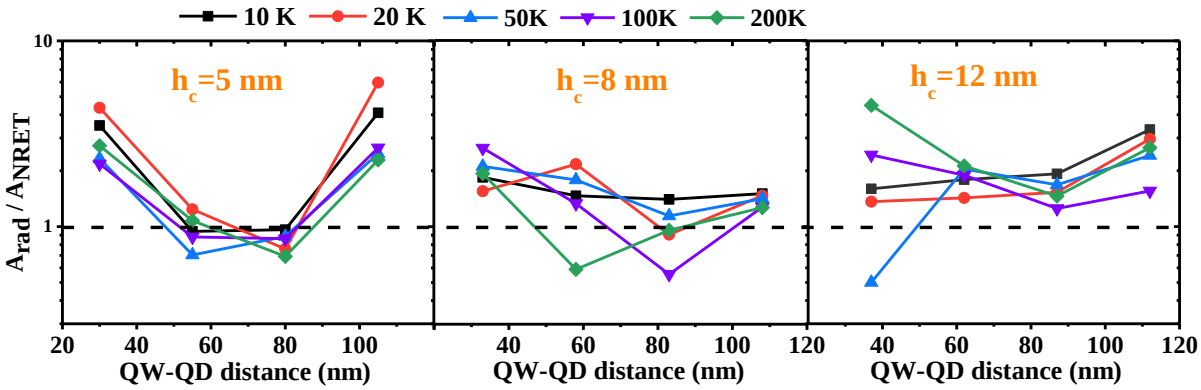

FIG. III.8. The fitting coefficients ratios of the radiative and the non-radiative component for the long-range coupling are depicted versus the QW-QD distance.

We can read the results by comparing the equivalent points to the efficiency in FIG. III.7. The NRET contribution appears more pronounced when the cap layer is the smallest and it concerns the QW-QD distance where the NRET efficiency was calculated to be the highest. On the other hand, it seems that for 5 and the 8 nm cap layers when the QW-QD separation

increases with the implementation of the 25 and the 100 nm spacer, the coupling takes place mostly through the radiative channel, which explains the lower NRET efficiency. Indeed, for 8 and 12 nm cap layers, the coupling takes place mostly through the radiative channel, specifically for temperatures up to 50 K.

Therefore, it seems that we have three different situations here. First, a highly NRET efficient coupling (higher than 90%) when the cap layer is 5 nm in a range only between 60-80 QW-QD distance and for shorter or longer distances the radiative process is more pronounced and the efficiency diminishes. Second, a less efficient NRET coupling (below 90%) for a smaller QW-QD distance window with an 8 nm cap layer. At the end, a much less efficient NRET coupling when the cap layer is 12 nm (below 80%) when the SiO_2 spacer of 50-100 nm is used, except when the latter is 25 nm, the NRET efficiency rises above 80% and it is the highest among the three cap layers for this distance.

III.5 Discussion

It is the interplay between the PL outcome with the results of the coupling efficiency that point out the existence-or not- of the long-range NRET coupling. Concerning the 5 nm cap layer, the NRET efficiency obtains its highest value at 10-200 K for a total QW-QD distance of 80 nm. This perfectly agrees with the results of the PL measurement (see FIG. III.4). This means that in this case, this sample exhibits an increase of the QD emission with a simultaneous decrease of the QW emission only when h_s=75 nm. The PL blue emission for the 8 and the 12 nm is weak and thus, it is more difficult to describe any connection between the PL and the NRET efficiency. The SiO_2 spacer layer was assumed to form non-quenching interface. In a similar study[161] that addressed PV applications and used materials very different from ours, they observed similar results with the use of a spacer, with the PL signal still effectively quenched by the donor for spacer layers up to 35 nm (i.e., the thickest spacer used in their study). As a last point, the influence of the temperature was not specifically analyzed. It is important though to note, that the theoretical calculated Förster radius and the electronic properties of the donor in general are temperature dependent[175]. With this in mind, a more in-depth analysis of our results should be planned in the future.

III.6 Conclusion

According to our time resolved and photoluminescence experimental results, the long-range NRET coupling was studied in an InGaN-QD configuration where the donor-acceptor

separation can reach up to 112 nm with the deposition of a SiO_2 spacer on top of the cap layer. Considering both the PL and TRPL measurements, lead to clear indication of NRET coupling. In this sense, the decreased donor-acceptor distance, along with the fact of a high binding energy in the QW that keeps the carriers well confined, it is reasonable to suggest that the emission from the QW is mostly coupled to the QDs rather than being recombined at the interface. Then, the cap layer thickness's variation with the temperature in the range of 10-300 K was evaluated as a potential parameter that can affect the NRET efficiency. It was found that the thinnest cap layer of 5 nm favors the most efficient long-range NRET coupling when the QW-QD distance becomes 80 nm regardless the temperature. Moreover, the thinner the cap layer, the longer the range for which a highly efficient coupling can take place. With all this in mind, the near-field electromagnetic coupling is a process that could play an important role in the design of highly efficient and compact devices. Thus, we believe that this fundamental study is a first step towards the comprehension of the NRET mechanism that could be possibly applied to an actual InGaN based multicolor LED device which uses QDs for the light down-conversion.

Chapter IV - Impact of the LDOS on the NRET: photonic crystal & QD blend

IV.1 Introduction

In chapter II and III, we investigated the impact that the dipole orientation and the donor-acceptor distance have on the NRET. Here, the focus is shifted to the capability of the local density of optical states (LDOS) to enable a more substantial control of the energy transfer between a donor and an acceptor active media (QW-QD or QD-QD).

According to the classical NRET theory, the LDOS is of prime importance as one of the parameters controlling the emission rate of the donor. For this purpose, we choose to investigate the energy transfer between green (donor) and red (acceptor) quantum dots (QDs) considering their photonic environment. We chose to work only with QDs for this first study as it was a relatively simple way to work with donors and acceptors in close proximity, and to integrate them onto a transparent and technologically feasible photonic crystal. Integration of acceptor QDs with donor QWs integrated within a GaN based photonic crystal is a more complex approach that proved to be technologically challenging, thus will be considered as an outlook of our work (see Chapter V).

The photonic environment is characterized by the LDOS, which counts the number of photon modes available for emission. In this work, we propose the use of photonic crystal (PC) structures as a means to control the LDOS at the vicinity and operating wavelengths of the donor and acceptor respectively.

However, proving that the NRET rate depends on the local photonic mode density or not is a challenging topic that has been an open discussion for many years. Considering this controversy, our protocol targets a full study of the interactions between the green and the red QDs in the NRET frame taking into account the PC elements. Depending on the case, the goal of the photonic structures is to support high or low LDOS (or both) in order to control the emission at the donor or the acceptor wavelengths (or at both).

In this chapter we will describe the design, fabrication and characterization of the samples dedicated to QD-QD coupling with the implemented PCs. Eventually, angle resolved and time resolved photoluminescence will be used to evaluate the coupling.

IV.2 Photonic nano-patterning for controlling the LDOS

Patterning surfaces and thin layers at the optical wavelength scale gives us the option to tailor the photonic environment and therefore the LDOS. Hence, it has been considered a key approach so as to manipulate the non-radiative energy transfer[106]. Several examples of

photonic bandgap engineering have been used to inhibit the radiative emission from the donor to the acceptor and at the same time have observed enhancement in the NRET including dielectric[107] and porous silicon[176], photonic crystals but also hyperbolic metamaterial comprised of an array of gold nanorods[109] etc. These geometries show great potential in the development of energy transfer-based applications such as biomedical imaging, organic solar cells, and light-emitting sources.

IV.3 Conception of the photonic system

The purpose of our photonic configuration is the enhancement of the NRET between two different types of CdSe QDs, a green donor and a red acceptor. In order to do that, we implement a TiO_2 square photonic crystal with holes, which we subsequently fill with a solution of green and red QDs mixed in equal quantity. The structure is described in the schematic of FIG. IV.1. Therefore, at first there is the possibility of NRET between the QDs that occurs spontaneously, even without the PC. Secondly there is the coupling between the QD emission and the PC that depends on the engineered LDOS. In this case, the resonance will trap the light at the desired wavelengths and thus increase the lifetime of the photons at the vicinity of the QDs which will promote the absorption/emission and at the same time, increase the coupling probability.

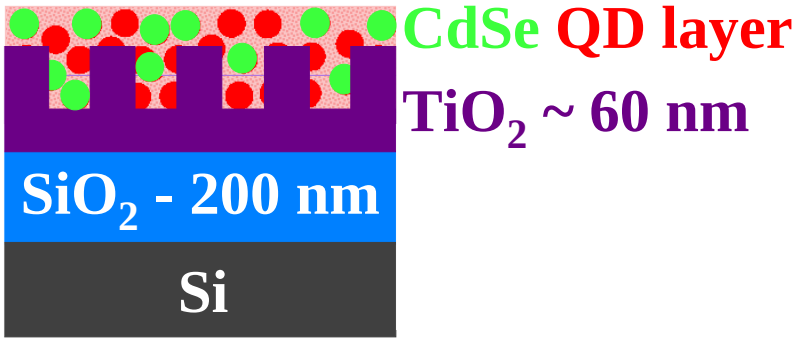

FIG. IV.1. A 2D schematic of the studied structure.

IV.3.1 Proposed protocol

We will consider all the possible situations that may impact in a different way the energy transfer: a resonance (or high LDOS) in the green and low LDOS (or no resonance) in the red, low LDOS in the green and high LDOS in the red, low LDOS at both wavelength ranges and high LDOS for both red and green.

It is essential to realise in what way the enhancement or inhibition of the PC emission in the green and/or in the red affects the energy transfer. The goal of the aforementioned protocol is to evaluate and extract conclusions about the interaction of the photonic modes with the emission of the donor and the acceptor QDs.

IV.3.2 Materials

IV.3.1.1 TiO_2 PC

TiO_2 was a suitable choice for the photonic crystal and it was selected for its advantageous optical properties. First and foremost, the TiO_2 is transparent in the visible spectrum, where our QDs emit. Secondly, its refractive index (n) is relatively high, around 2.4 for the wavelengths of interest. The refractive index of the QD-PMMA layer, around 1.5, leads to a high refractive index contrast enabling a good light confinement.

Then, the TiO_2 has similar refractive index to that of GaN. This means that the observations could be applied to a GaN structure as well, as this is the material that will be finally used in a micro-LED.

IV.3.1.2 CdSe QD

It is well known, that the QDs can exhibit highly efficient exciton transport, as a result of strong quantum confinement and excellent optical properties. In the frame of energy transfer studies, the results showed that the dipole approximation works rather well for spherical CdSe QDs, as NRET in close-packed CdSe quantum-dot solids arises from dipole-dipole interdot interactions between dots in close proximity[177],[178],[179].

In our case, red and green colloidal CdSe QDs that are prepared in separate solutions with solvents and PMMA polymer (the formulation is confidential) were manipulated. For our experiments we used a blend that contained an equal amount of each, in order to obtain a homogeneous solution. The quantum yield was measured to be around 0.74 for both red and green QDs. A solution containing only red QDs was also prepared, in order to realise reference layers.

IV.4 Design of the photonic structures

We performed 3-D Rigorous Coupled Wave Analysis (RCWA) simulations, in order to predict the spectral behavior of our structures. As mentioned above, the photonic crystal is a square pattern with holes. The goal is to obtain the parameters of the design (period of PC pattern, diameter of the holes, TiO_2 slab thickness and depth of the holes) that can exhibit sharp resonance peaks at 530 nm (in the green) or/and at 630 nm (in the red) according to the already defined protocol.

The refractive index of the materials was adjusted depending on the respective wavelengths where the PC operates; therefore, at 530 nm the considered indices were 2.54 and 1.46 and at 630 nm 2.47 and 1.46 for TiO_2 and SiO_2 respectively. The optical properties of the CdSe/ pmma thin film of 6% QD volume ratio provided by the Bruggeman's effective medium approximation[180] was calculated to be 1.56 and 1.55 at 530 and 630 nm respectively. Additionally, the media are considered transparent. According to our simulations, the thickness of the PC should be less than 100 nm in order to sustain only one guided mode in the wavelength range of interest.

In the simulations, the optical resonance corresponds to a peak in the reflectance spectrum of the photonic crystal, known as Fano resonance[181],[182]. We have observed high reflectivity for several pairs of values of period and diameter in the range of 290-410 nm and 130–280 nm respectively. In FIG. IV.2, an example of the reflection peaks for a PC of 60 nm thickness (fully etched pattern) and a QD layer of 100 nm are presented for a 340 (FIG. IV.2.(a) and 410 nm (FIG. IV.2.(b)) period. By varying the diameter, we can select the appropriate geometry, so as to obtain a resonance at 530 and 630 nm respectively.

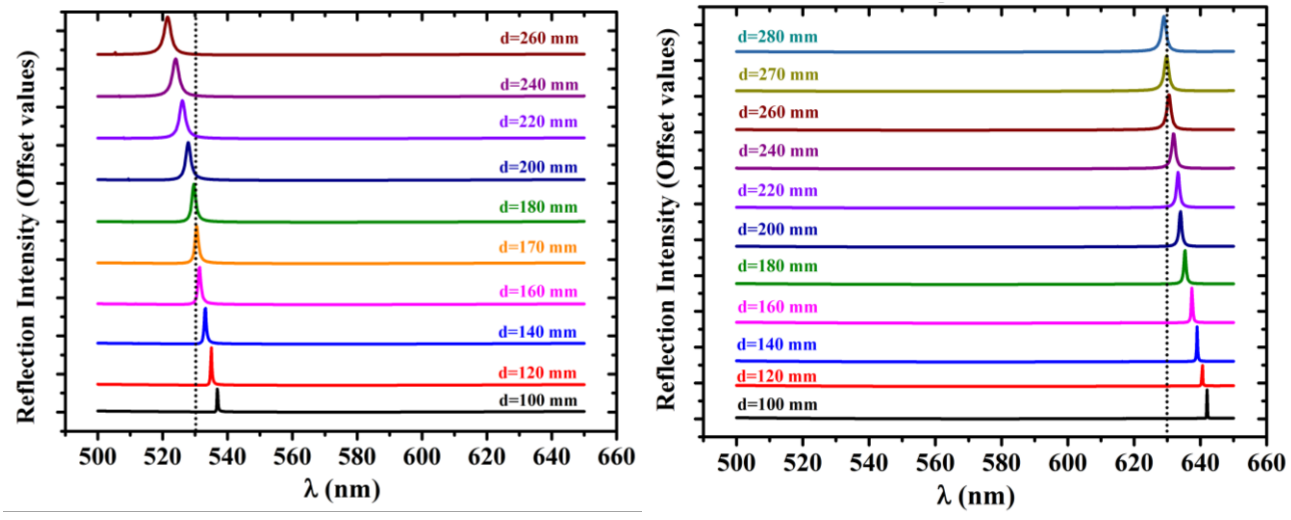

(a) **(b)**

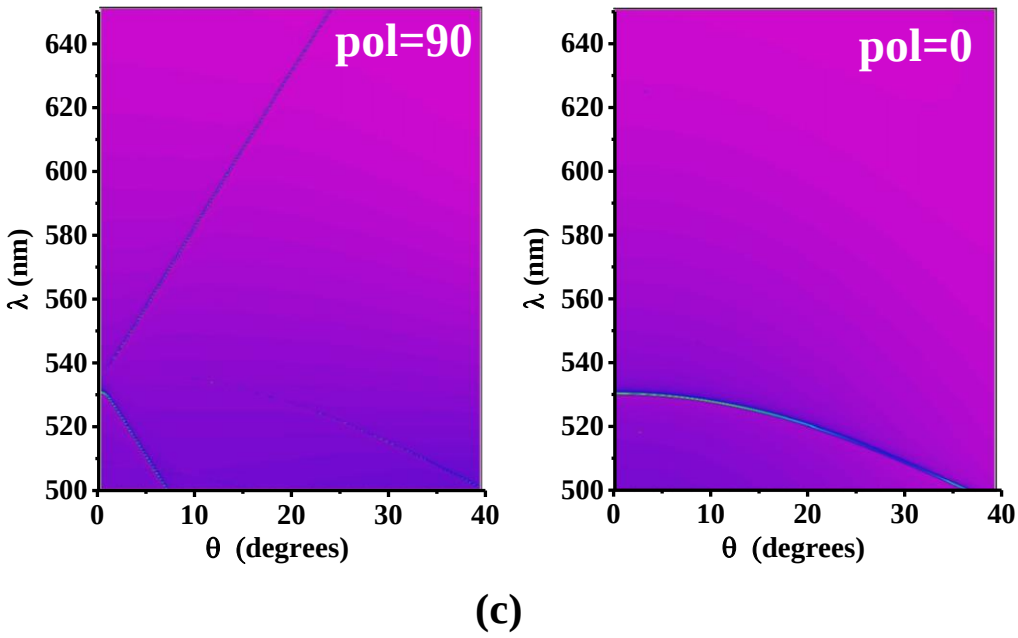

FIG. IV.2. The simulated optical resonances of a TiO_2 PC of 60 nm thickness (totally etched pattern) and 100 nm QD layer for period of (a) 340 nm design for the enhancement in the green and (b) 410 nm design for the enhancement in the red respectively, at the Γ point of the band dispersion. In (c) an example of the simulated resonances in the two polarizations: design at 530 nm.

More specifically, the type of resonance that we target is a slow light mode (flat band) at the Γ point of the photonic band dispersion diagram (corresponding to normal incidence), see FIG. IV.2.(c). Using such a low group velocity mode will make it possible to trap the incoming photons and thus increase the probability of the NRET coupling.

IV.5 Fabrication Process

The procedure to obtain the final design can be divided into two main parts: the fabrication of the PC and the deposition of the QD mix. Concerning the PC, its realization included the following steps of a standard process: deposition of the TiO_2 layer by sputtering, e-beam lithography (EBL) and reactive ion etching (RIE). The second step was the spin coating of the QD solution on the PC. The whole process is depicted in FIG. IV.3 and analytically described in the next sections.

IV.5.1 Fabrication of the TiO2 photonic crystal

The first step was the deposition of TiO_2 on a SiO_2/Si substrate of 200 nm SiO_2 as we can see at FIG. IV.3.(a). Before the deposition, the samples were cut in approximately 2 cm^2 samples and then cleaned with DI water.

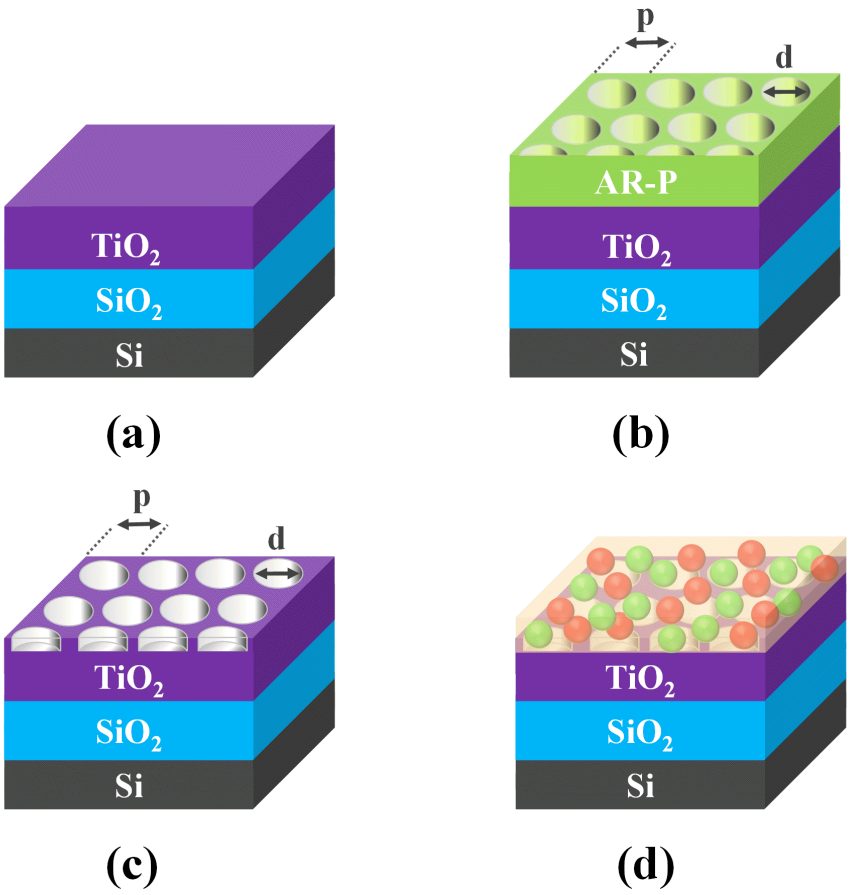

FIG.IV.3. A schematic of the four fabrication steps: (a) sputtering deposition of a TiO_2 thin film on top of a SiO_2/Si substrate, (b) e-beam lithography for the PC holes patterning on the AR-P resist and then development, (c) reactive ion etching in order to transfer the PC pattern to the TiO_2 and (c) spin coating of the QD mix on the sample.

We used the AC450 magnetron sputtering machine. The layer was deposited in reactive mode from a Ti target. The target condition (poisoning effect) was characterized by monitoring of plasma, using optical emission spectroscopy (OES) and target voltage measurements. The TiO_2 deposition parameters were Ar/O_2 flows = 80/4 sccm, pressure = $2x10^{-3}$ mbar, RF power = 370W, target bias = 320 V at room temperature. The thickness obtained was around 90-95 nm after 45 min and the structural characterization (X-Ray diffraction analysis) showed that the thin layer was weakly crystallized.

The second step of the PC fabrication process was the EBL, see schematic (b) in FIG. IV.3.

The preparation of the sample involved the spin coating of the positive resist AR-P 6200.04. The parameters of the spin coating were the following: 4000 rpm, 3000 rpm/s for 60 s. After that, post baking for 60 s at 150 °C took place. The thickness of the resist was measured with photo-reflectometry to be around 90 nm, uniform across the sample. Then, the e-beam lithography is performed in order to pattern the resist (SEM Inspect F electron beam microscope from FEI, equipped with e-beam writing system Elphy Plus system from Raith). The surface of each design was chosen to be in the 40x40 to 50x50 μm^2 range. The resist is then developed in order to reveal the exposed patterns.

The third step, as we can see at FIG. IV.3.(c), was transferring the pattern to the TiO_2 by using the AR-P resist as a mask. This was achieved by reactive ion etching (Corial 200S). A substantial study regarding the patterning of TiO_2 took place (with the contribution of the fellow PhD student Dang Nguyen Ha My). Hence, several etching recipes were tested and the results in terms of etching rates are presented in the following table. It should be noted that the tests are indicative of the RIE as they were realized on an unpattern TiO_2 surface.

	Parameters		**Rates**	
Recipe	**Power (W)**	**Pressure (mT)**	**Resist (nm/min)**	**TiO_2 (nm/min)**
10SF_6 / 5Ar	150	50	15	15
100CHF_3	140		3	15
20CHF_3	140		22	20
50CHF_3 / 5SF_6	140		50	50

Table IV.1. Presentation of the RIE recipes for the (plain surface) TiO_2.

We selected the recipe that led to the highest etching selectivity (v), i.e., the highest ratio $v_{etch,TiO2}/v_{etch,\ resist}$: 100 sccm CHF_3, at pressure of 30 mT and a power of 140 W, for 500 s. The etching rates of all the other recipes were similar for both the resist and the TiO_2 leading to a low selectivity (~1). In the case of nanopatterned surfaces, the etch rates are modified, and the maximal value of TiO_2 etching depth that we could obtain was 60 nm, which corresponds to the situation where the whole resist layer is already removed.

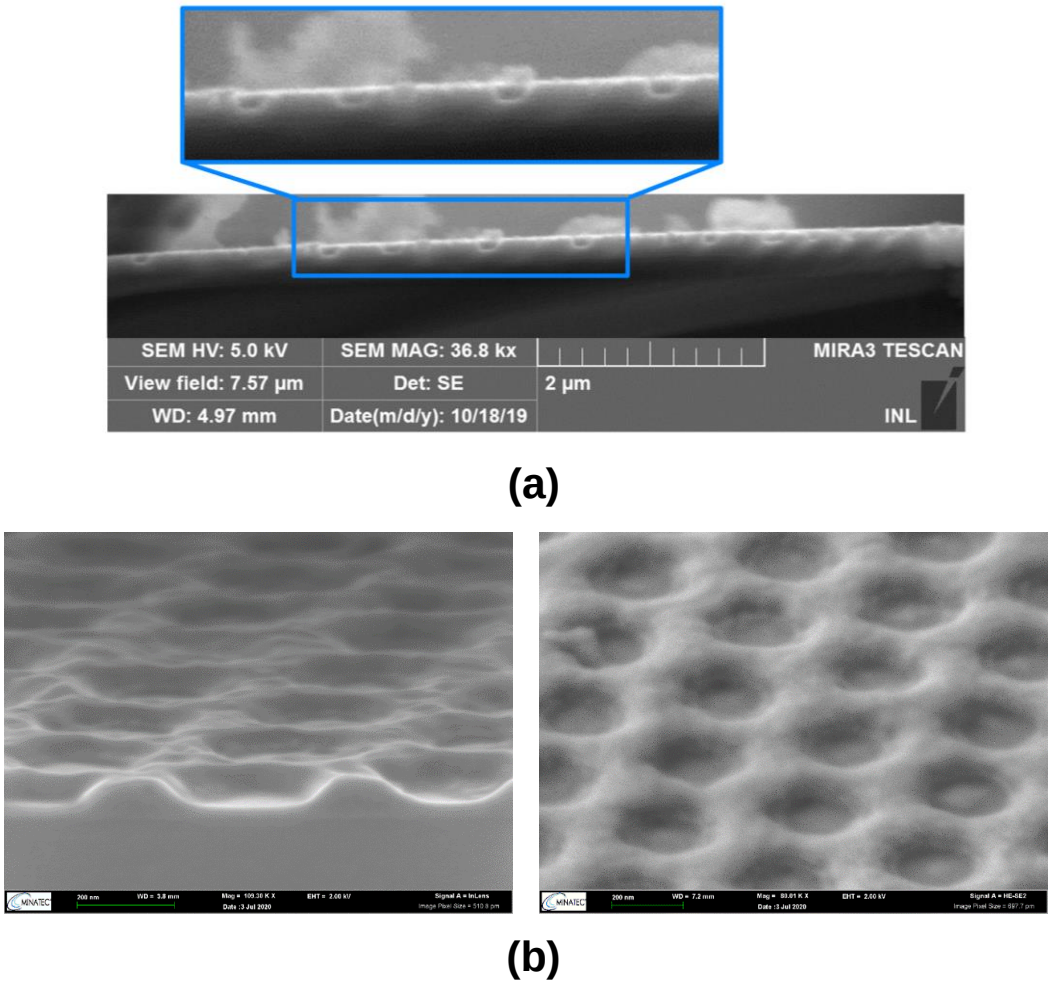

FIG. IV.4. The SEM cross section of the holes at (a) 0° and (b) tilted view. We can have a very good overview of the holes' imperfect formation.

To examine the shape and size of the PC holes, SEM cross sections were performed along with atomic force microscopy (AFM) as can be seen at FIG. IV.4 and FIG. IV.5. The top view SEM images show that the holes were circular, despite the grainy nature of the TiO_2. Indeed, the roughness of the sputtered TiO_2 is in the order 2 nm and the grain size of tens of nm. While hole diameters ranged from 90 to 340 nm could be obtained, the holes with diameter below 130 nm and above 300 nm did not exhibit a regular shape. For lower diameters the holes were not completely open after the RIE (FIG. IV.4, first row) and for the highest diameters, the holes merged, forming pillars. Moreover, as shown in FIG. IV.5 the sides of the holes exhibited a certain slope instead of being vertical (and form a cylinder). In addition, all the designs exhibit an etching depth of 60 nm regardless the diameter of the holes.

At this point, it is clear that a mismatch is expected between the experimentally obtained patterns do not exhibit the same geometry as the theoretically predicted designs.

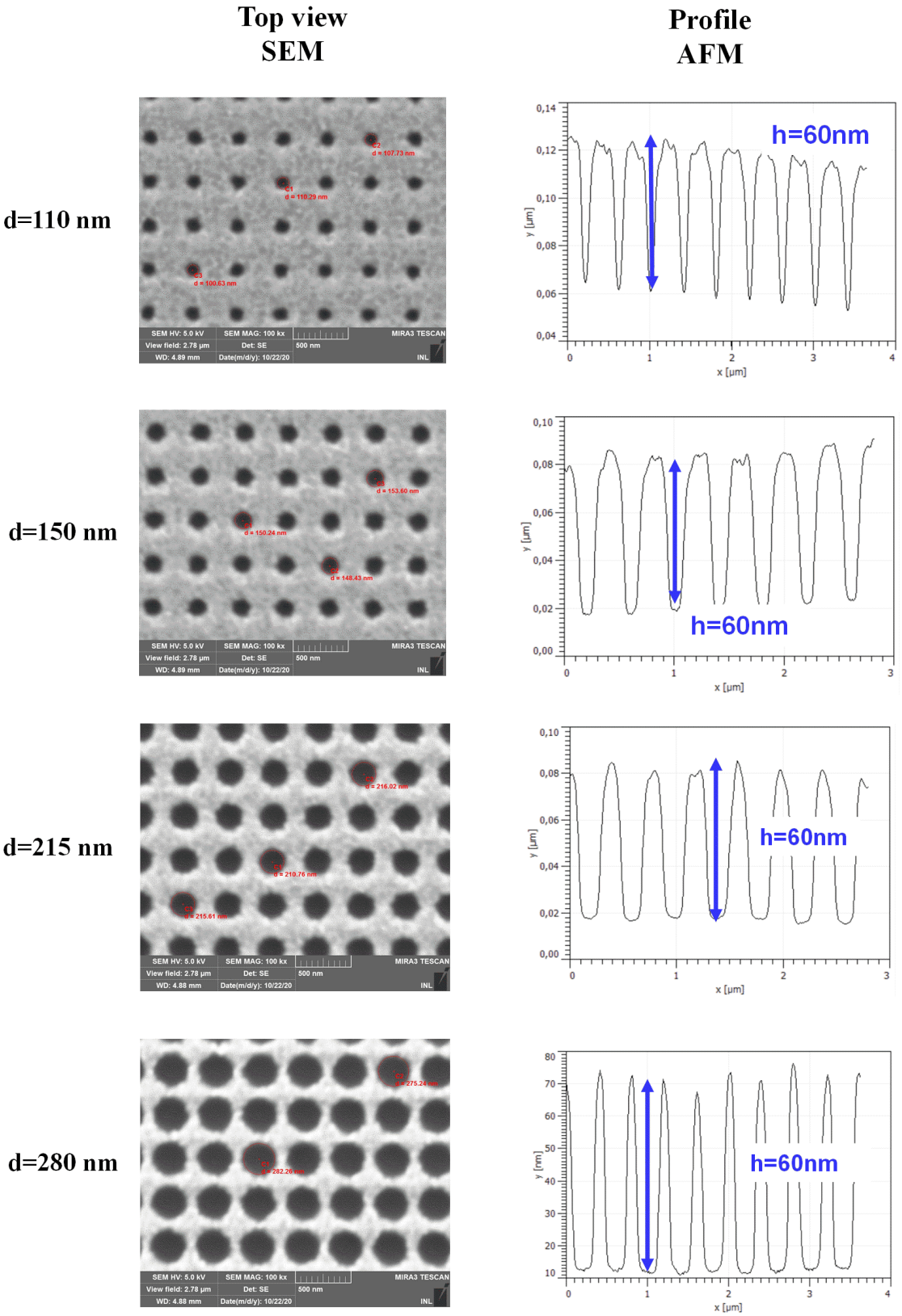

FIG. IV.5. On the left-hand side we can see the top view of a patterning with 400 nm period and varying diameter from 110 to 280 nm. On the right the corresponding AFM profiles.

Multiple designs were used, with periods from 290 to 410 nm. The diameters really achieved ranged from 90 to 340 nm. The table below shows the correspondence between the diameter of the e-beam pattern design and the final diameter of the holes as it was measured by SEM (top view).

d (nm)					
e-beam	**RIE**	**e-beam**	**RIE**	**e-beam**	**RIE**
130	90	220	170	310	280
140	100	230	180	320	285
150	110	240	190	330	300
160	115	250	210	340	320
170	125	260	215	350	340
180	130	270	230		
190	140	280	230		
200	150	290	250		
210	160	300	250		

Table IV.2. The values of the diameters of the holes of the e-beam patterning and compared to the obtained final diameter after the RIE.

IV.5.2 QD layer

The photoluminescence signal of the green and red QD blend and the solution with red QDs on plain surface is depicted at FIG. IV.6. Although the red QDs came from the same initial solution, the final solution that contains only red QDs is much more intense than the one of the blends. The reason behind that is that although the red QDs belong to the same initial solution, it was not possible to reproduce the exact same formulation as in the blend. The quantum dot emission bandwidth is 30-40 nm as we can see at the graph below.

The deposition of the polymer containing the QDs on the patterned surface was proven to be a demanding procedure for reasons related to the thickness of the expected layer. First, it is necessary to visualize and localize the patterned areas underneath, for their characterization. Second, a thick film would completely shunt the coupling to the PC modes as a large part of the QDs would stand outside the vertical mode extension. Therefore, the coating should be made so as to obtain a layer as thin and homogeneous as possible. The spin coating took place twice for each sample and the parameters of the deposition were: 1000 rpm, 2000 rpm/s for 10 s. However, it should be noted here, that the QD solution was not optimized for spin coating deposition in terms of viscosity.

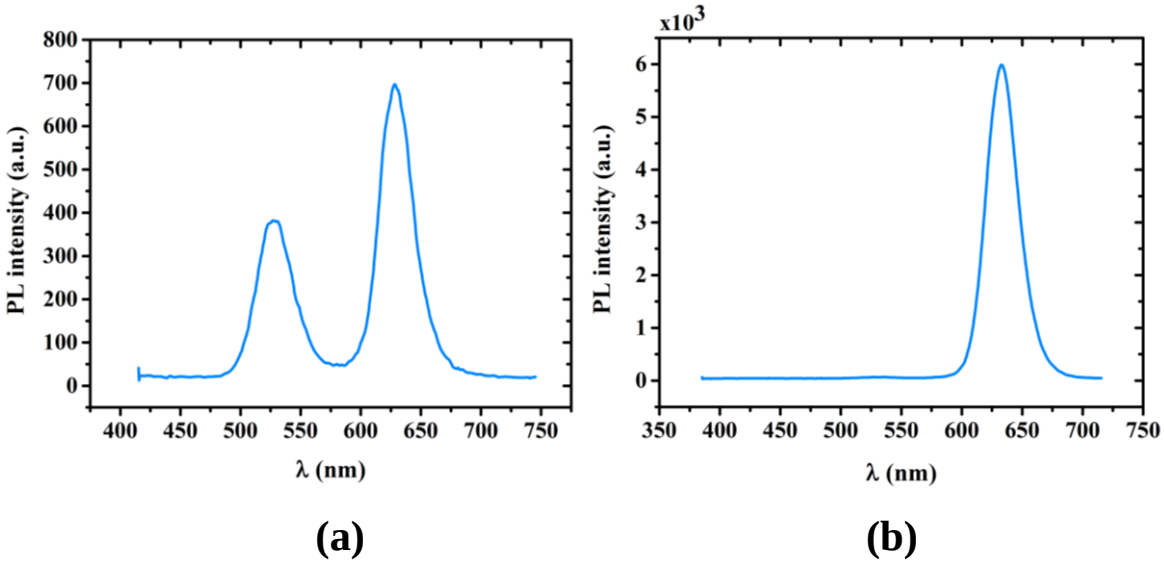

FIG. IV.6. The PL emission intensity on plain surface for the (a) green and red QD blend and (b) solution that contains only red QDs.

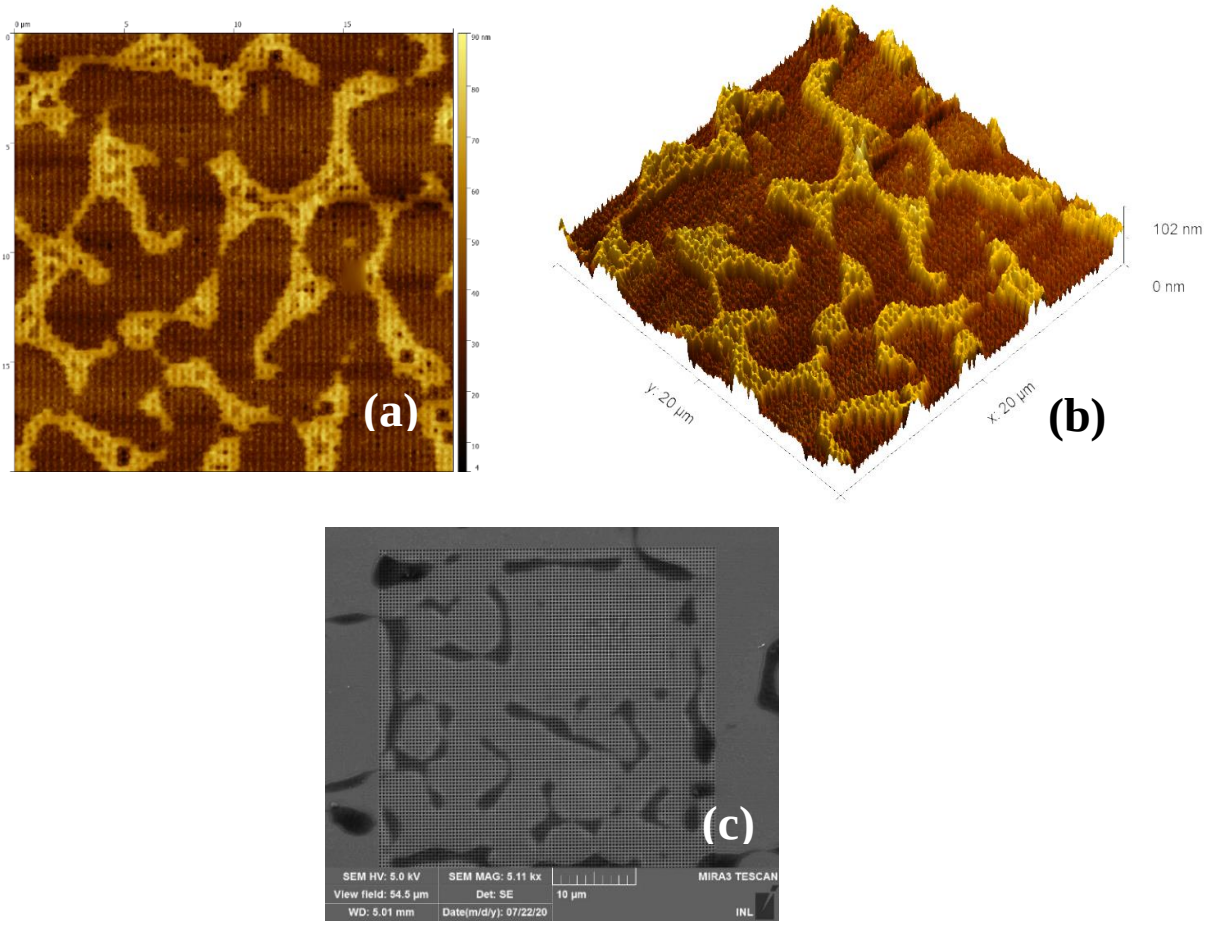

FIG.IV.7. An example of the AFM colloidal QD spin coating deposition in (a) top view and (b) 3-D tilted view. (c) The measurement with the SEM.

Moreover, patterns with different air filling factors (diameter/period) have been considered, as this is expected to have an impact on the amount of solution that can enter the holes and finally on the achieved geometry of the deposited layer.

To evaluate the deposition, we anew performed structural characterization. In FIG. IV.7.(a) and (b) the AFM images unravel that the QDs are aggregated and do not form a uniform layer, but areas in the range of a few 100 nm. As we can see, the deposited QD-in-polymer forms "islands", which is far from homogeneous in terms of surface but somehow uniform in terms of thickness (according to the color bar). It also appears that the whole surface of the PC got covered by the layer but it is remains uncertain if the QD blend completely filled the PC holes.

IV.6 Optical characterization

Overall, many photonic patterns were simulated, constructed and studied, but for the purpose of this thesis, the discussion will concern only the following: PC with periods of 300 and 380 nm, and with fabricated diameters that vary between 90 and 215 nm. According to the simulations, the objective of the series of patterns with the small period is the enhancement of the coupling between the PC and the emission rate of the donor QD, thus the impact of the LDOS in the form of an optical resonance in the green. The aim of the second series of patterns with a larger period is the enhancement of the acceptor's emission rate. That means that its band dispersion contains only one optical resonance in the red range. In order to compare these results with a reference, the same patterns but covered only by a thin film that contains only red QDs, were investigated.

For each PC-QD design we performed three different types of optical measurements: angle resolved-microreflectivity (ARμR), angle-resolved PL (ARPL) and time resolved PL (TRPL).

IV.6.1 Angle resolved measurements

In this section, we first describe the principle behind the angle resolved measurements along with the description of the set-up. We then present and discuss the ARμR and ARPL experimental results.

IV.6.1.1 Principle and set-up

The interplay between energy and momentum is at the heart of resonant dielectric structures such as is found in vertical microcavities or photonic crystals, dictating the light propagation,

emission and absorption. FIG. IV.8.(a) presents the scheme to obtain the dispersion characteristic in a single shot measurement and FIG. IV.8.(b) shows a detailed description of the set-up. More specifically, in our case we used the spectrometer microHR, Horiba and the 1024×256 CCD camera Syncerity, Horiba. The non-polarized diffracted light that originates from the light-matter interaction between the incoming light (from a halogen lamp for the ARμR or a 405 nm laser for the ARPL) and the nanostructures was collected with a microscope objective x20.

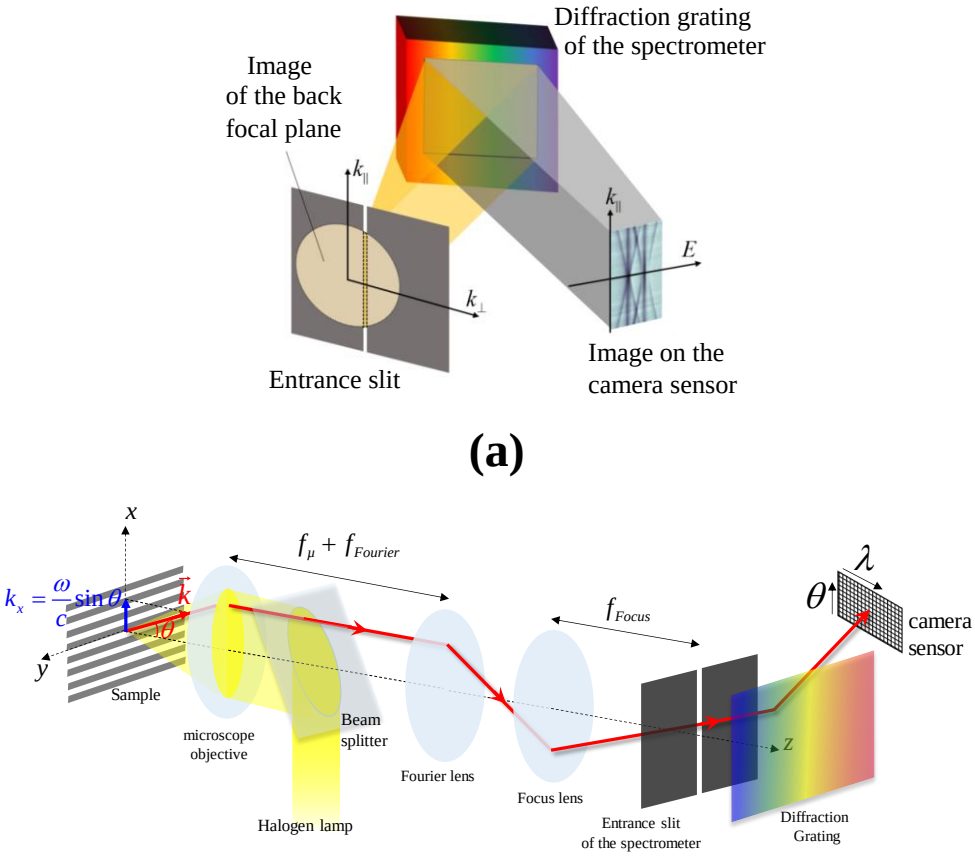

FIG.IV.8. (a) The scheme to obtain the dispersion characteristic and (b) the schematic description of our setup.

At first, the excitation light is focused onto the sample via the microscope objective. The emitted light is collected via the same objective, and its image in the Fourier space is projected onto the entrance slit of a spectrometer. In the case of a PC, the sample orientation is aligned so that the ΓX direction is along the entrance slit. In this scheme, the grating inside the spectrograph disperses the incoming signal along the energy axis. The output of the spectrometer is captured in the CCD camera located at the (output) plane of the spectrograph.

The resulting image obtained from the camera leads to the energy-momentum dispersion diagram along ΓX: the dispersion curves are revealed in the dips/peaks in reflectivity, or photo-luminescence.

IV.6.1.2 ARμR measurements

The first step was the ARμR characterization of the hybrid PC-QD blend enabling the direct measurement of the photonic band structure, thus the position of the slow light modes. The results are depicted in FIG. IV.9. Such measurements were performed for the whole set of PC-QD structures, with all the available period and obtained diameter values.

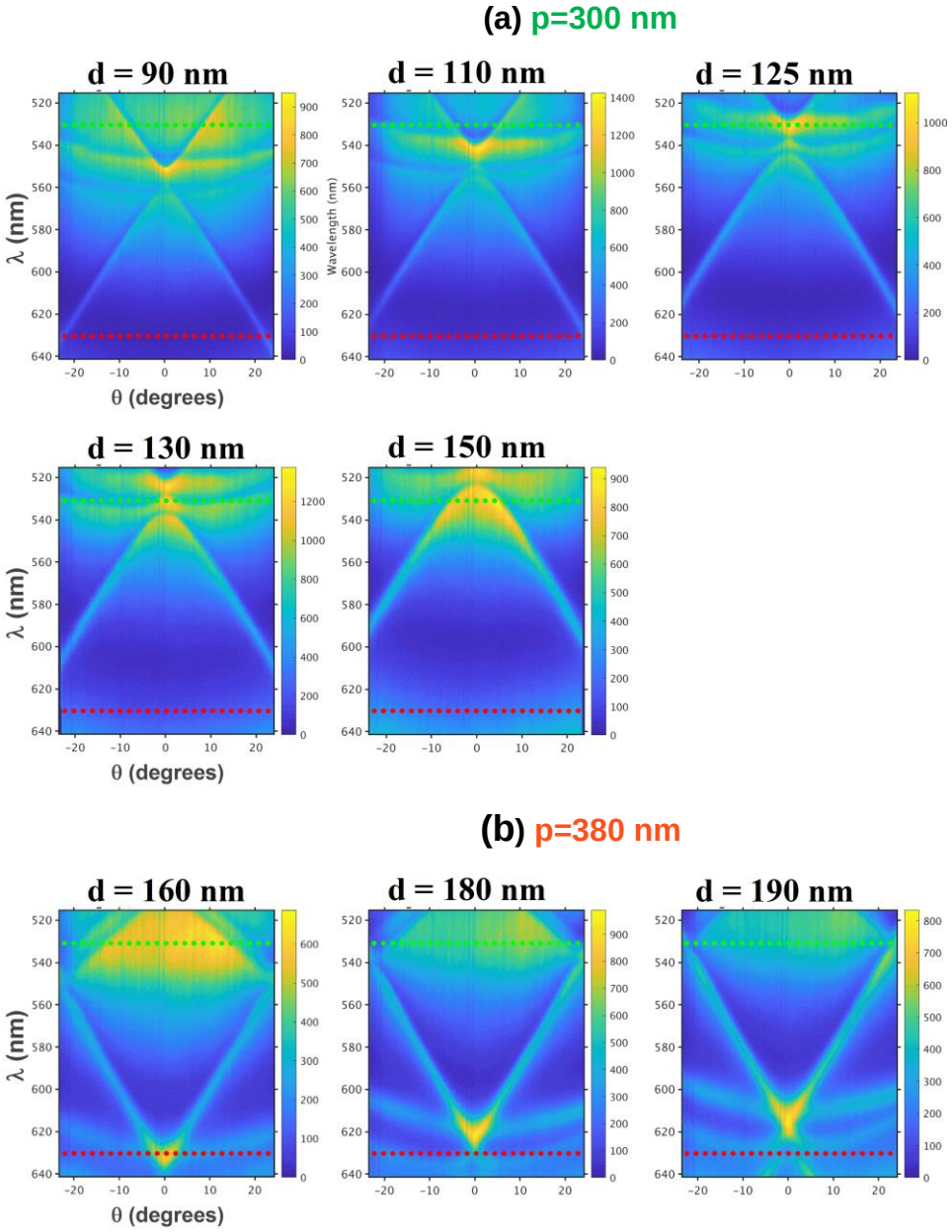

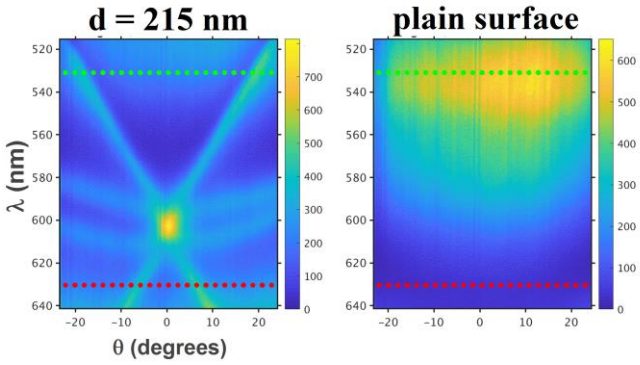

FIG.IV.9. The experimentally obtained band dispersions (non polarized light, 2 s acquisition time) for the period of (a) 300 and (b) 380 nm and for the unpatterned surface. The values of the diameters are exhibited above each graph.

In FIG. IV.8 we see that there are fast (large slope) and slow (flat) light modes in all our dispersion maps. In case (a), i.e., the 300 nm period, the modal density is high in the green range, whereas there are no modes whatsoever in the red range. In (b), for the 380 nm period, we have the exact inverse case where the modal volume in the red is high and with no modes in the green range for the larger diameters, and very low modal volume for the smaller ones but far from the Γ point. Then, as the diameter increases, the resonance shifts towards shorter wavelengths as expected.

Considering the difference in terms of etching depth and holes shape, we expected a substantial difference between the simulated and measured spectra, in particular in terms of resonant wavelengths. For this reason, we fabricated a larger set of structures, with more periods. Indeed, in the simulations (FIG. IV.2), the designs with p = 340 nm (and d = 170-180 nm) show a reflection peak in the green, while those with p=410 (and d= 260-270 nm) were calculated to create a resonance at 630 nm. Results presented above show that appropriate PC correspond to p=300 and d=125 nm for a resonance in the green and to p=380 and d=180 nm for a high modal volume in the red. This is why we have selected these periods for the investigated structures.

IV.6.1.3 ARPL measurements

In order to investigate the PC-QD coupling, we performed experiments to observe simultaneously the emission of both the green donor and the red acceptor and hence quantify their respective emission intensity. For our experiments, we used the set-up mentioned above

by replacing the halogen lamp with a UV laser in continuous wave mode (405 nm, 40 µm laser spot).

In this section, the ARPL for the PCs for which the band dispersions were presented above will be analysed for two cases: deposition of the green and red QD blend and the deposition of only the red QDs. In other words, we will first investigate the impact of the LDOS on the NRET with the deposition of the QD blend on the nanostructures. The objective of the second step of experiments with only red QDs to compare with a situation where no NRET is possible. Careful cleaning of the sample is performed between the first and the second set of experiments; the QDs are removed by sonication in toluene.

IV.6.1.3.1 ARPL blend of green and red QDs

The ARPL results for the blend are presented in FIG. IV.10 along with the angle- integrated intensity for each wavelength, in order to quantify the spectral emission. In FIG. IV.10.(b), are presented the designs for a 380 nm period aimed at tuning the emission wavelengths of the acceptor with an optical resonance as mentioned above. We can see that for 180 and 190 nm of obtained diameter the PC modes couples with the red emission from the QDs and as a result we obtain an enhanced emission in the red of equivalent intensity with the first case (a) but at the donor's wavelength.

In FIG. IV.10.(a) we can see that for a diameter of 125 nm, while the LDOS (flat band) is increased exactly at the position of the emission wavelength of the donor QD (also see FIG. IV.9), the integrated intensity in the red range around 630 nm increases to almost 60000, compared to the values below 40000 for other diameters, and although the red QD emission wavelength is not tuned with an optical resonance. Therefore, while we observe an emission increase in the green when the LDOS is high in the green, which is trivial, we also observe an emission increase in the red, although no optical resonance is observed in this wavelength range. This cannot be achieved if only the direct coupling between a QD and a mode is considered. This observation then tends to show that there is an energy coupling between the donor and the acceptor, promoted by the high LDOS at the donor wavelength.

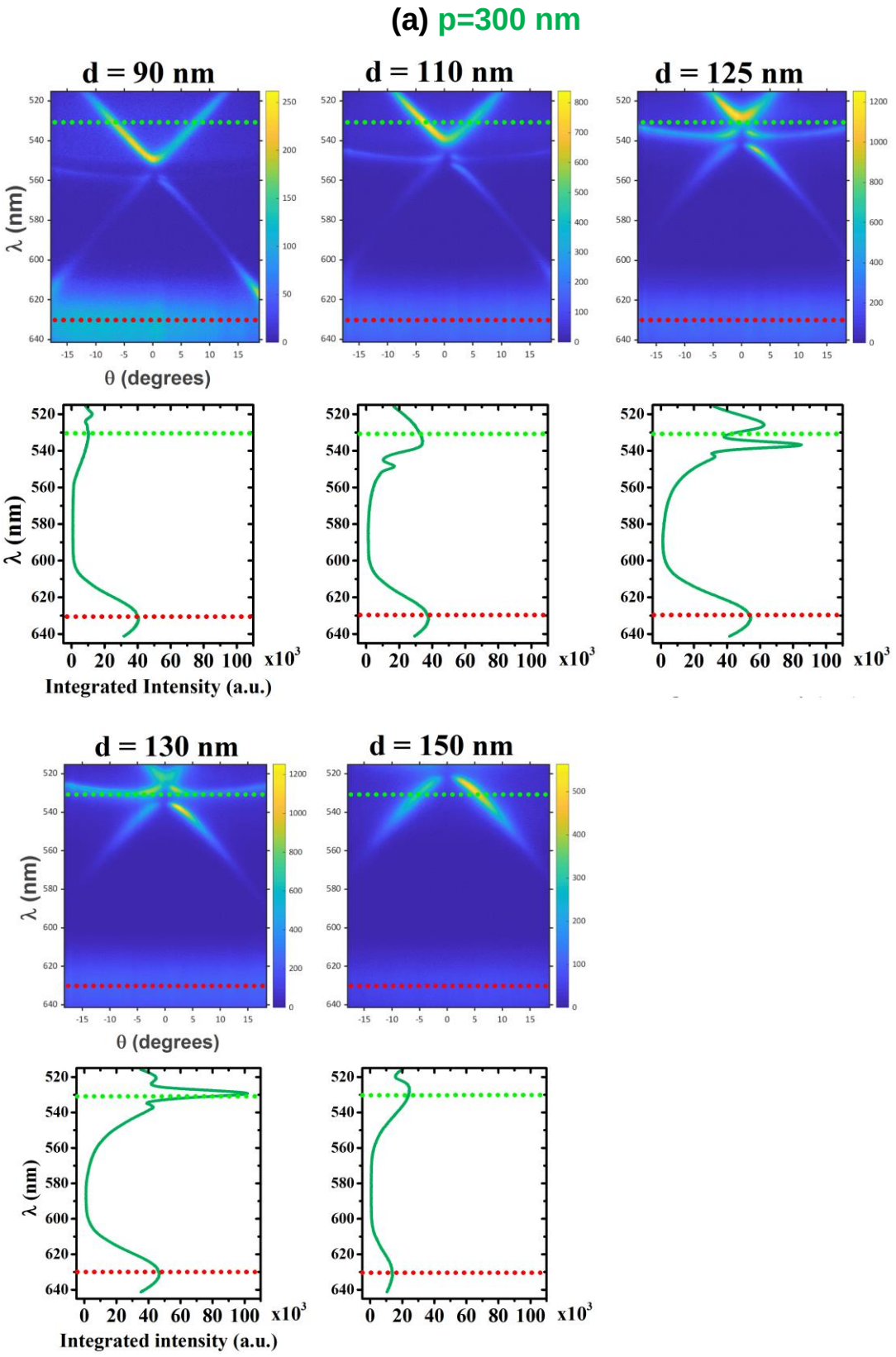
(a) p=300 nm
d = 90 nm
d = 110 nm
d = 125 nm
λ (nm)
θ (degrees)
Integrated Intensity (a.u.)
x10^3
d = 130 nm
d = 150 nm
Integrated intensity (a.u.)

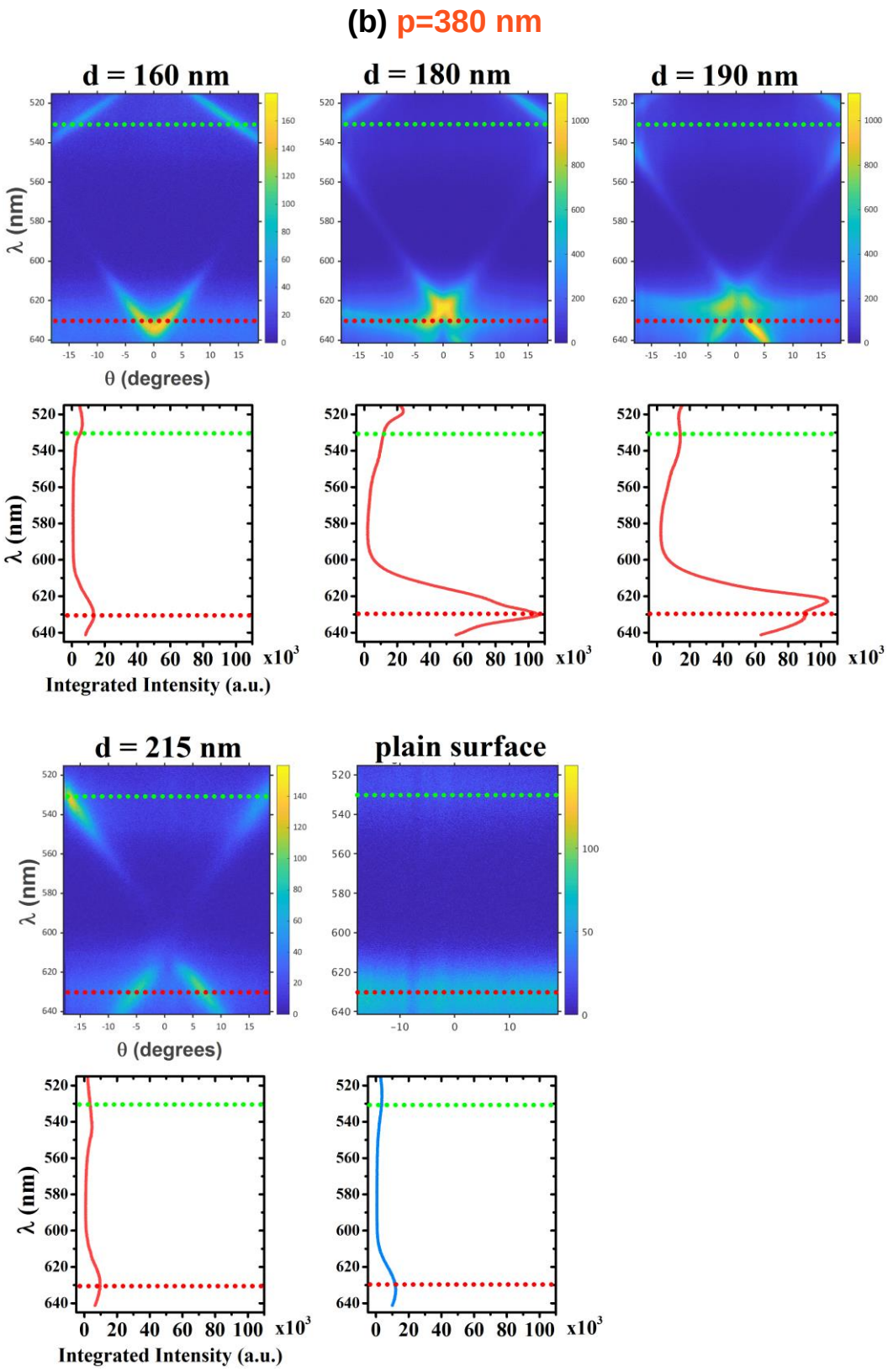

FIG. IV.10 The experimentally obtained ARPL results for designs that target the enhancement via the LDOS of (a) the donor's emission in the green and (b) the acceptor's emission in the red.

IV.6.1.3.2 ARPL only red QD

As explained above, the two QD solutions (blend and only red), although containing the same type of QD, were obtained by a different formulation. Nevertheless, even a qualitative comparison of the evolution of the emission in the red range with and without the donor QD is essential in the frame of our work.

ARPL has been performed on the same structures, for both periods, as presented FIG. IV.11. As expected, there is no emission in the green as there are no green QDs. For the period of 300 nm, the evolution in emission intensity is very limited. We can also distinguish the band dispersion of the PC, which here does not have an impact on the emission.

Not surprisingly, the integrated emission in the case of p=380 nm where the nanopatterning targets the enhancement at 630-635 nm is much sharper and higher compared to the case of p= 300 nm. Especially for 180 nm diameter where the optical resonance is exactly at the desired wavelength, the red emission gets from 250000 to 400000.

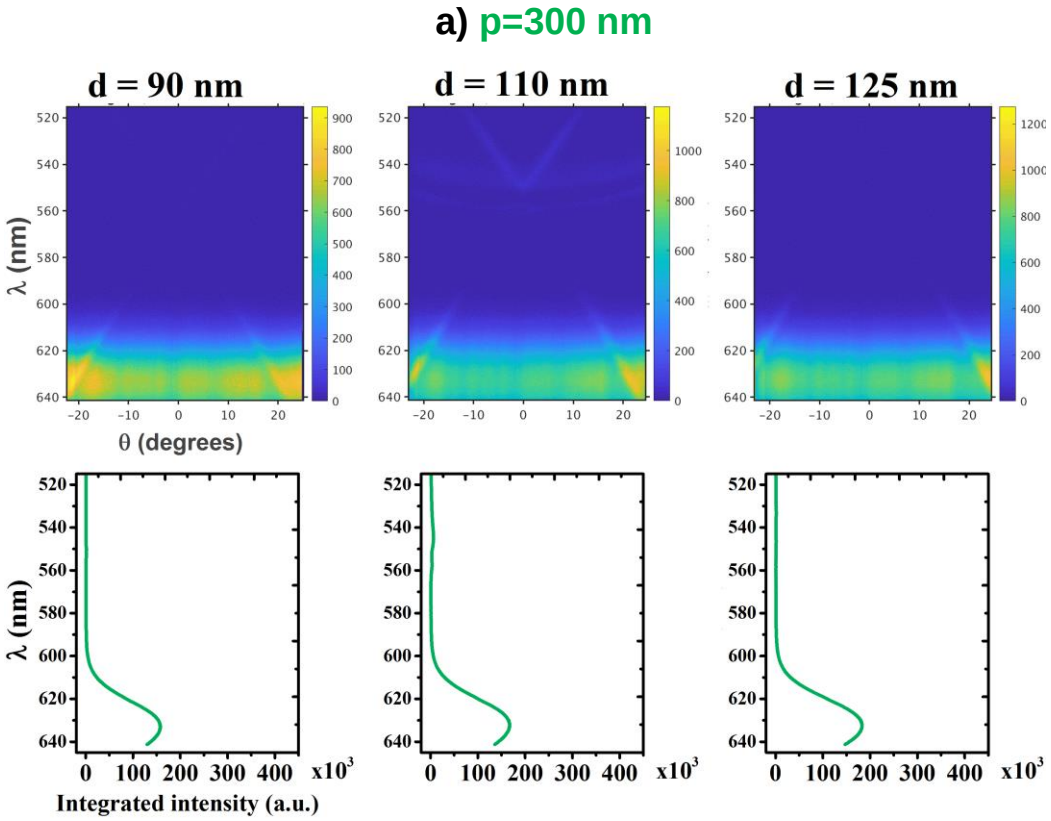

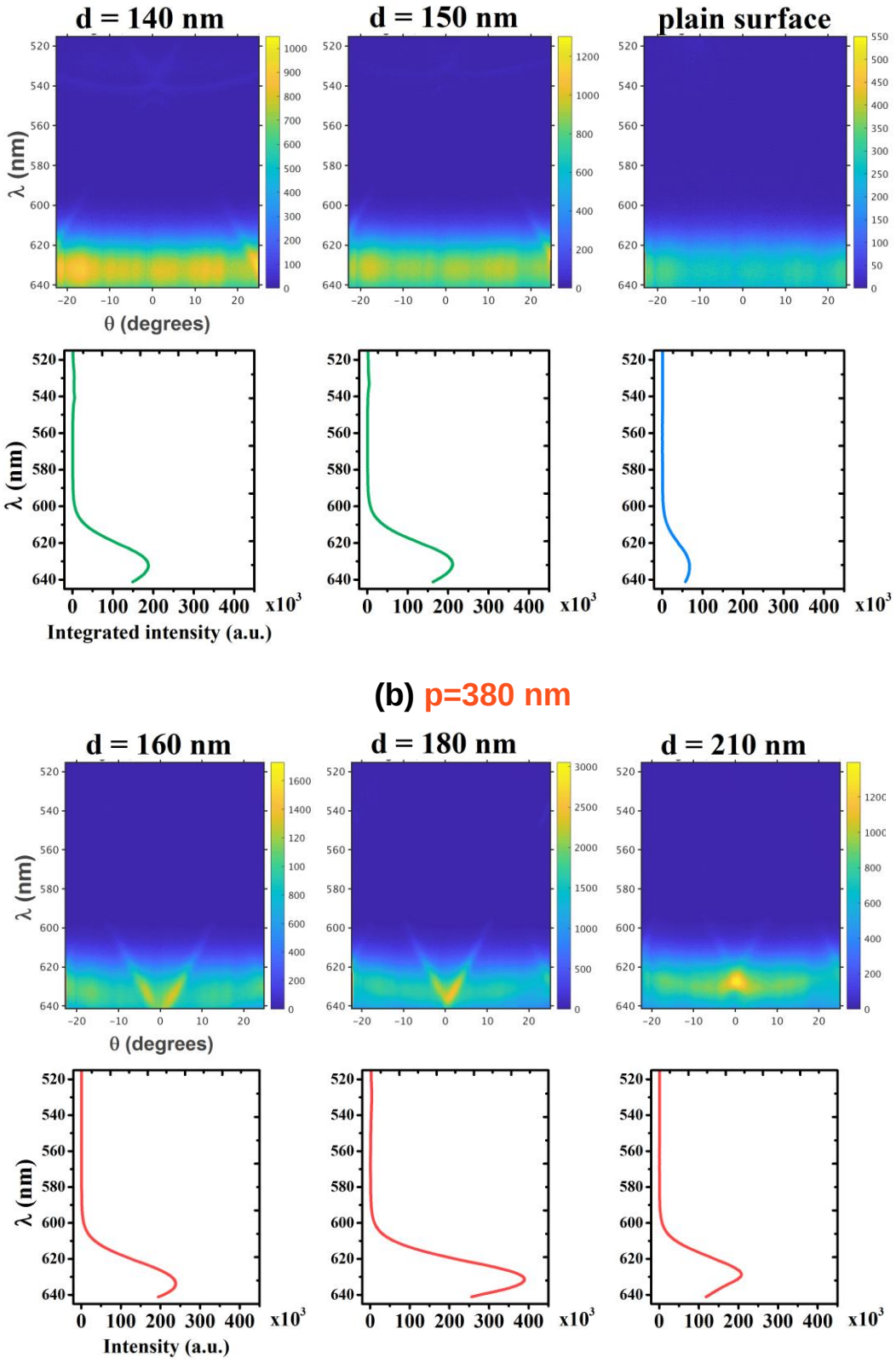

FIG. IV.11. The experimentally obtained ARPL results for the designs covered by only red QD.

IV.6.1.3.3 ARPL comparison

Finally, in the case of the PC with red QDs only, an almost 2-fold enhancement of the emission in the red is achieved when the resonance is tuned with the QD emission wavelength. Meanwhile, we do not have any specific enhancement when the mode is in the green.

Within the case of the the mixed QD layer, a 35% intensity increase is observed in the red when the mode is tuned with the green QDs (p=300nm, d=125nm). And more importantly, a 7-fold enhancement of the emission is achieved in the red when the mode is tuned with the red QD emission wavelength (p=380nm, d=180nm).

While the red emission, alone or mixed with green QDs, is increased in a substantial way when tuned with an optical resonance in the red (with a factor between 2 and 7, we do observe lower but yet clearly measurable emission increase for red QDs mixed with green QDs tuned with a resonance in the green. This tends to show that green QDs are mediator enabling a higher increase of the red emission. And it appears to be the case both for resonances in the red and in the green. At this stage, this can only be considered as an indication of the control of the coupling between QDs by the LDOS. TRPL experiments are needed to further investigate the radiative or non-radiative character of such coupling.

IV.6.2 Time resolved photoluminescence measurements

As a last step, in order to further investigate the coupling between the various elements of our system, we carried out time resolved measurements at the emission wavelengths of interest. We used the same set-up as in the previous chapters.

The TRPL signal along with the exponential decay fit is presented in FIG. IV.12. More specifically, in FIG. IV.12.(a) and (b) are depicted the time decays where the LDOS have been measured to be at the position of the emission wavelength of the donor (p=300) and the acceptor QDs (p=380 nm) respectively.

From the comparison of the two curves both the green and the red decay is much faster for the selected pairs of data. The TRPL curves were fit with a double exponential, which corresponds to a fast and a much longer contribution $y = y_0 + A_{long}e^{(-t/\tau_{long})} + A_{short}e^{(-t/\tau_{short})}$. An indication of the probability or the weight of each of the two coupling mechanisms is the coefficient of the respective exponentials ($A_{long}$and A_{short}). Therefore, the TRPL of both the green and red emission decays with a double exponential. In our configurations, this possibly means that the interaction between the red and green QDs takes

place either through the energy transfer or the radiative process. The coefficient ratio was once again (as in the previous chapter) calculated as a means to give a further insight to the results.

The time decay curves along with the extracted lifetimes and the fitting coefficient ratio are depicted in the graphs of FIG. IV.12 and FIG. IV.13 for the two cases of 300 and 380 nm period respectively. It should be herein noted that it was not possible to do the lifetime extraction from the unpattern surface because the signal was much too weak to enable an accurate fit.

IV.6.1.4 TRPL blend of green and red QDs

Analyzing the TRPL data, we notice a special case for p=300 nm and d=125 nm where the decay rate is enhanced. For this particular structure, according to the ARPL the emission rate of the donor is maximized. Therefore, when the mode is tuned with the green QDs, both for red and green QD emission and for both for radiative and non-radiative components we observe a decreased lifetime. Therefore, for the green emission this can be explained both a Purcell and possibly a NRET enhancement due to the high LDOS.

Now concerning the red emission, although there is no mode at this wavelength, it still shows a decreased lifetime, following the decrease of the green emission lifetime, although no Purcell effect can be expected at that wavelength. The reason for this decreased lifetime remains unclear at this stage.

A similar observation can be made in the case of the 380 nm period, for diameter 215 nm. In the same sense, as we can see in FIG.IV.13.(a) and (b), the TRPL shows a faster decay in the green and in the red emission. However, for such structure, slow light resonances are tuned with the red emission. A possible explanation of this behavior could be related to the presence of the fast modes tuned with the green QD emission, as shown in the ARPL measurements in FIG. IV.10.(b).

IV.6.1.5 TRPL only red QDs

The interaction of the same structures with only red QDs were then studied. The time decay was again a bi-exponential fit with two contributions. As we can see in FIG. IV.14, since there is no coupling, we only see the impact from the tuning of the red emission with the photonic modes. For the designs with 300 nm period that were fabricated to affect the LDOS in the green, there is no impact at all and thus, the lifetime remains the same.

On the other hand, in FIG. IV.14.(b), we can see the impact of the design with diameter of 180 nm, where the red emission is tuned with the LDOS as a decrease in the lifetime.

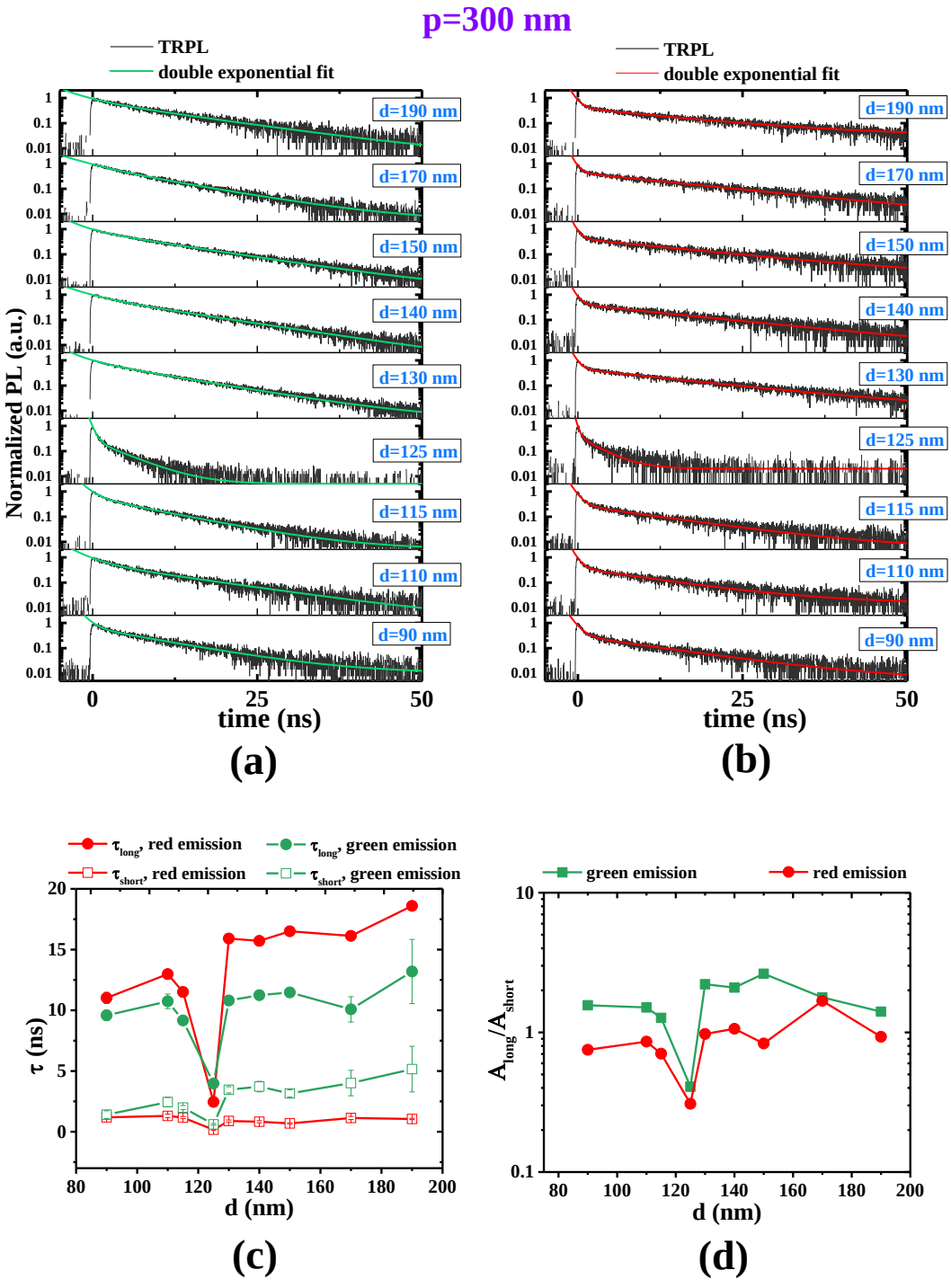

FIG. IV.12. The depiction of the measured lifetimes for the (a) green and the (b) red emission with varying the diameter for period of 300 nm for the QD blend. The extracted (c) lifetimes and (d) fitting coefficients ratio from the bi-exponential decays for the evaluation of the coupling.

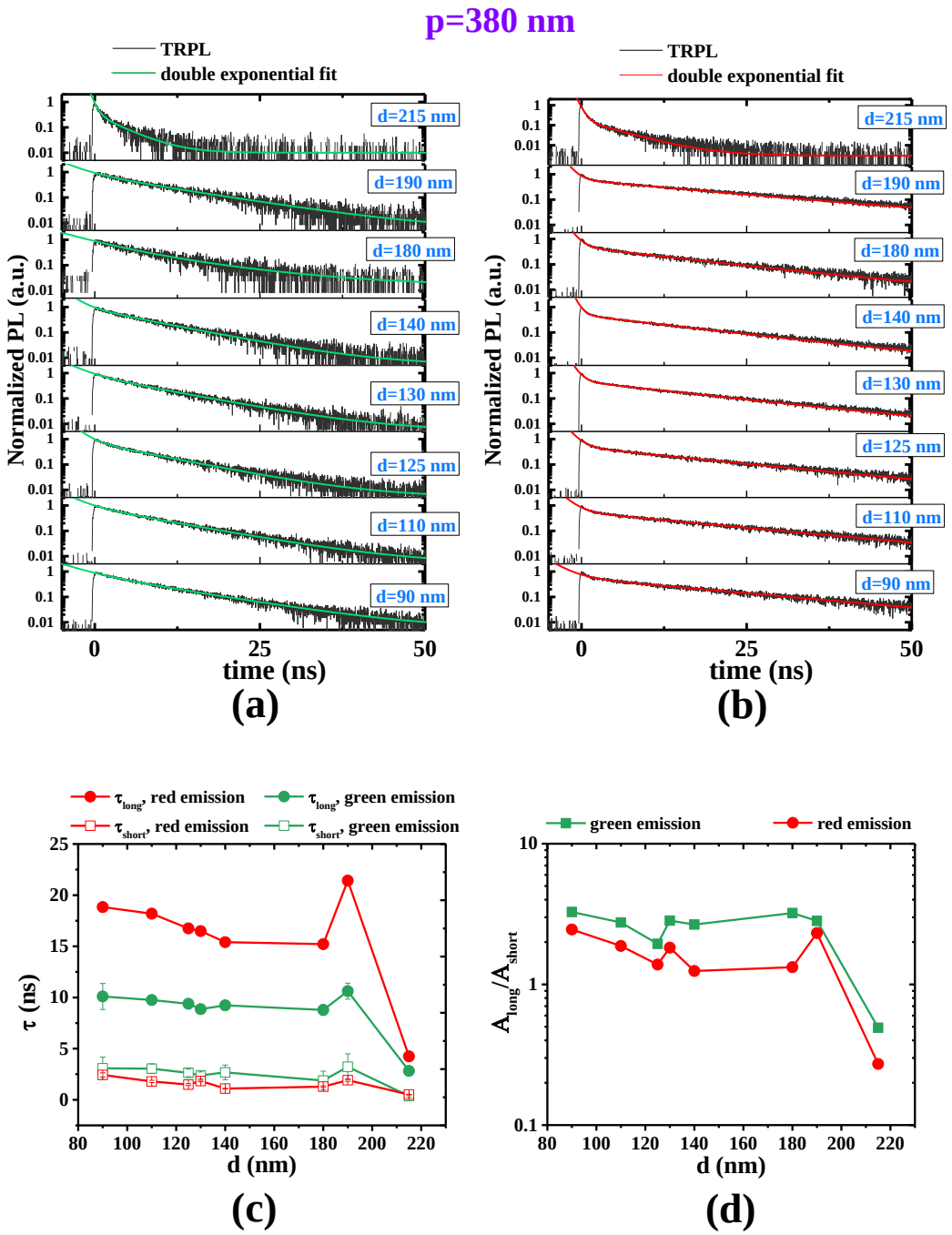

FIG .IV.13. The depiction of the measured lifetimes for the (a) green and the (b) red emission with varying the diameter for period of 380 nm for the QD blend. The extracted (c) lifetimes and (d) fitting coefficients ratio from the bi-exponential decays.

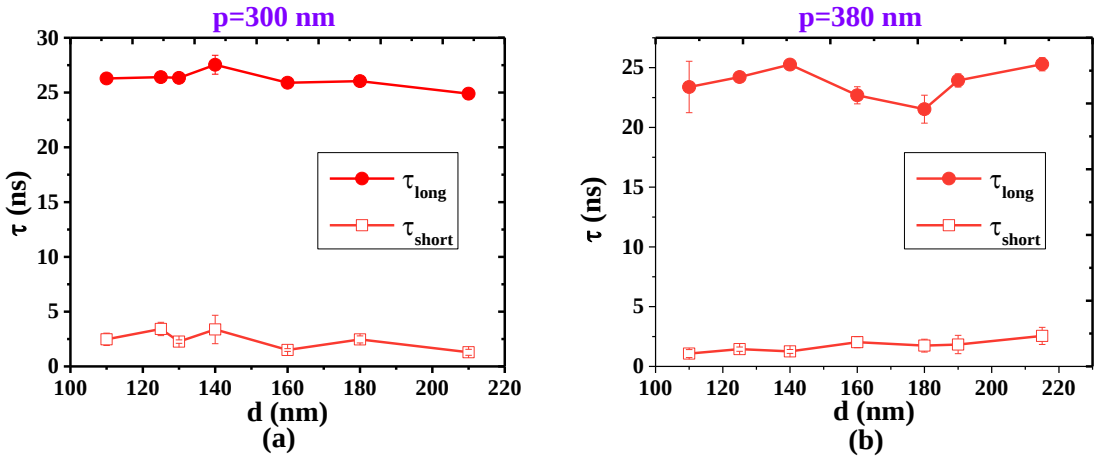

FIG. IV.14. The depiction of the measured lifetimes for the red emission of the structures covered with only red QDs with varying the diameter for period of (a) 300 nm and (b) 380 nm.

IV.7 Conclusion

The impact of the optical resonances that are supported by photonic crystal patterns on the energy transfer between green and red QDs was studied at the donor and the acceptor wavelength respectively. In this context, the fabrication of the PC patterns, although not perfect, led to slow light modes tuned with the red and green emission of the QDs depending on the design parameters. Then, ARμR, ARPL and TRPL measurements showed that these complex configurations include a lot of parameters to take into account and thus, the interpretation of the results is not straightforward. We can see the impact of the Purcell enhancement in the radiative contribution, and we have obtained possible indication of QD-QD energy transfer coupling. But at this stage, it is not yet possible to assess that the non-radiative transfer is represented well in this interaction scheme. A better understanding would be possible with additional experiments. In our case it was not possible to completely inhibit the radiative emission in the green in order to evaluate the existence of an additional coupling mechanism as we always had the contributions from the fast modes. In addition, one should bear in mind that the NRET is an excitonic process and thus trying to control more precisely the exciton flow from the donor to acceptor using their density of states could be the next step[183]. Still, with a view to the application, the PC are a powerful tool when it comes to wavelength selection for the control of the emission. Such an advantageous design could enable the optimization of each micro-LED-pixel separately by simultaneously enhancing or/and inhibiting the emission at specific frequencies depending on the displaying needs.

Chapter V - Impact of the LDOS on the NRET: circular grating & QDs

V.1 Introduction

In this chapter we investigate an alternative way to access the impact of the local density of optical states (LDOS) on the non-radiative energy transfer (NRET). For this purpose, we chose to perform a study on the coupling between a multi quantum well InGaN/GaN based concentric circular grating (CG) and red CdSe quantum dots (QDs). As the CG plays the role of a photonic nanocavity in charge of controlling the LDOS, the objective here is to investigate the impact on its coupling with the QDs. In the frame of this study, the CG structures were designed to strongly affect the emission of the donor QW or the acceptor QDs, by supporting resonant modes at the respective wavelengths or photonic bandgaps (PBG). Considering the complexity of the technological process, the fabrication and use of such CG is beyond the scope of this PhD thesis. Therefore, in this chapter we will only present the simulated designs and the fabrication method.

V.2 Circular grating

A concentric grating[184] or annular Bragg resonator, is a structure that can provide the low volume and high quality factor (QF) modes that we need in order to strongly localize the light and in this way observe the impact of LDOS on the NRET. Such kind of patterns are mainly useful for light extraction[185] and can even show lasing properties[186]. As we can see in FIG. V.1, the cylindrical designed structure is composed of periodic alternate layers that are interrupted with a radial defect in the middle. The light is vertically confined in the central pillar by radial Bragg reflection.

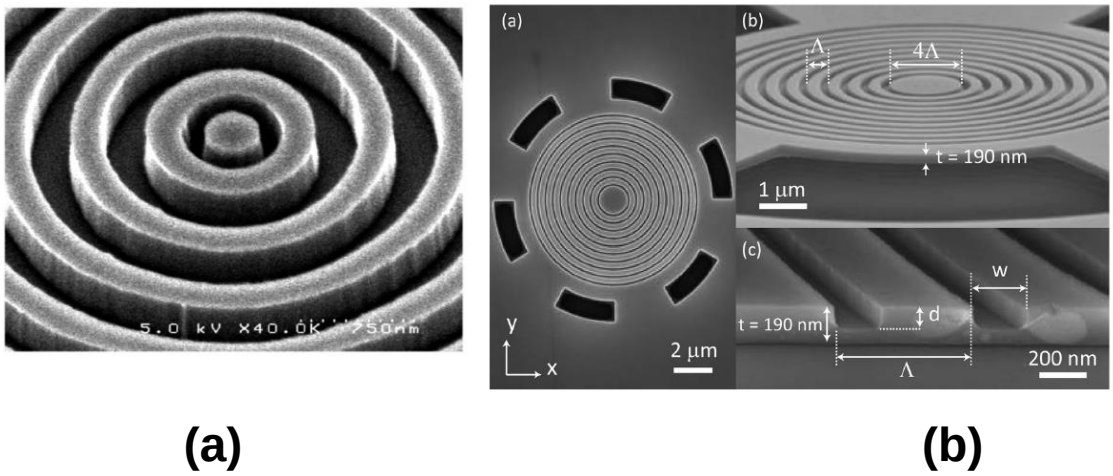

FIG. V.1. Examples of circular Bragg nanoresonators with a central pilar – cavity from the work of (a) Scheuer *et al*. [186] and (b) Davanço *et al*. [185].

V.3 Proposed protocol

In the frame of this study, we established a protocol that gives us the opportunity to separately investigate the impact of the LDOS on the emission of the donor and of the acceptor. Overall, three types of structures were designed that can support resonances at 460 nm, at 630 nm and no resonances whatsoever.

V.4 Design of the photonic configurations

GaN is a robust material that combined with the QD layer can provide us with an adequately high refractive index contrast. The refractive indexes of InGaN/GaN and PMMA layer including CdSe are: 2.46 and 1.56 at 460 nm wavelength, 2.39 and 1.55 at 630 nm respectively. Therefore, their contrast is adequate for the generation of resonant modes in the center of the CG. On top of that, GaN is the basic material for micro-LED fabrication, so any results could open a discussion towards the direction of this application. A schematic of the resonator is presented in FIG. V.2.

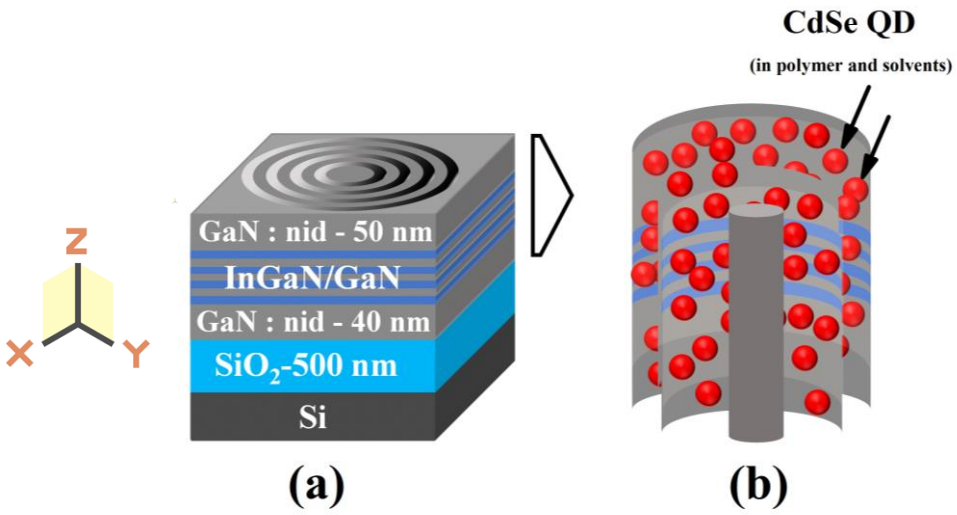

FIG. V.2. Schematics of (a) the final structure with the circular grating. The active area is composed of four (4) InGaN QW which is a standard fabrication for LED on a standard SiO_2/Si substrate. (b) a close-up of the alternating layers of the grating: the active area is fully etched and the QDs can enter.

The circular Bragg reflector is composed of an InGaN/GaN-QD multilayer periodic structure. The colloidal QDs are mixed with PMMA and solvents (the formulation is confidential). As described in FIG.IV.2.(b), the QD solution is expected to fill the fully etched CG. In this way, the QDs will be in close proximity to the QW in order to increase the

probability of a NRET coupling, as the energy transfer theory demands. This concept has been already used for the enhancement of the energy transfer in an InGaN-QD configuration by placing the QDs in holes etched through the MQW[69],[66].

FDTD (Finite-Difference Time-Domain) simulations (the software Lumerical was used for this purpose) were performed in the 3-D space in order to design such structures. The goal is to obtain the geometrical parameters (period, diameter of the cavity) that can support a cavity mode at 460 nm, at 630 nm wavelength and a band edge mode.

The concentric grating supports lateral (x-y plane) and vertical (z axis) electric (E_x, E_y, E_z) and magnetic (H_x, H_y, H_z) photonic modes and the QW can couple to both. The axis definition is included in FIG. V.2. Here, the design and classification of the modes in terms of geometrical characteristics was based on the H_z field[184],[187]. The finite grating is excited with an electric dipole source in the middle of the cavity. For example, by engineering the cavity mode in the blue (wavelength of 460 nm), the QW emission will then couple to the circular grating photonic modes E_x and E_y.

Our simulations showed that the thickness corresponding to single mode propagation in the semiconductor layer can be up to 110 nm and hence this is the value that was used. The high index cavity was preferred as a way for a better confinement of the modes. The calculated values of the period (p) and the cavity diameter (d_c) are presented in Table V.1 which is followed by the simulated emission intensity of the electromagnetic fields for the three cases of the established protocol in FIG. V.3, V.4 and V.5 respectively. For the light confinement, we proposed a circular grating of 14 periods which is less than 5 μm total diameter of the whole structure for all the designs. The air filling factor (d_c /p) was set to be 0.5 in all the cases.

p (nm)	**d_c (nm)**			**λ_{res} (nm)**	**PBG (nm)**
130	175	395	615	460	-
190	255	580	900	630	-
130	300	500	-	-	460
190	450	800	-	-	630

Table V.1. The values of the cavity diameters for the study of the impact of the LDOS on the NRET.

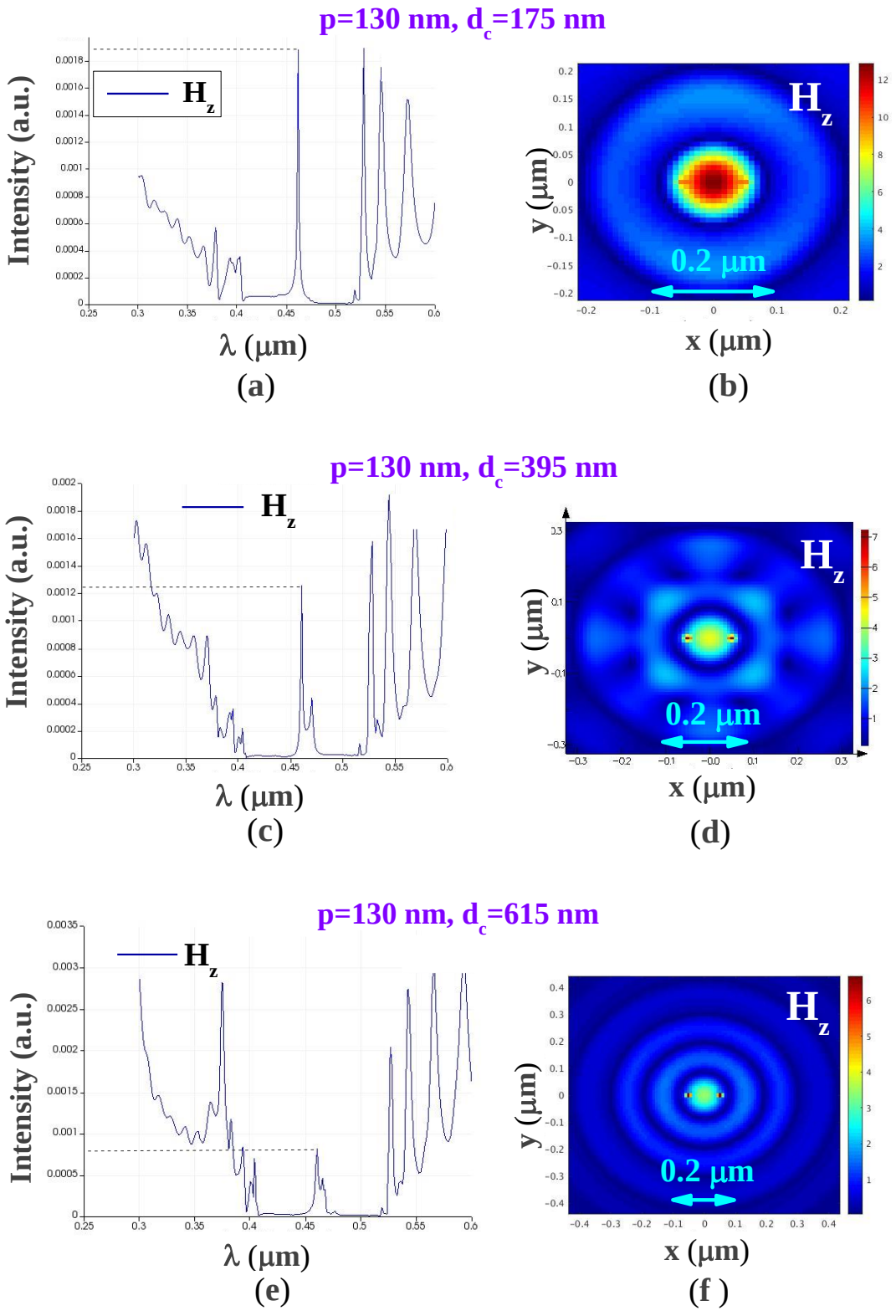

FIG. V.3. (a), (c), (e) The simulated optical resonances of the aforementioned circular grating at 460 nm (the emission wavelength of the donor). In (b), (c), (f) the maps of the Hz field emission that was used to classify the modes of the grating.

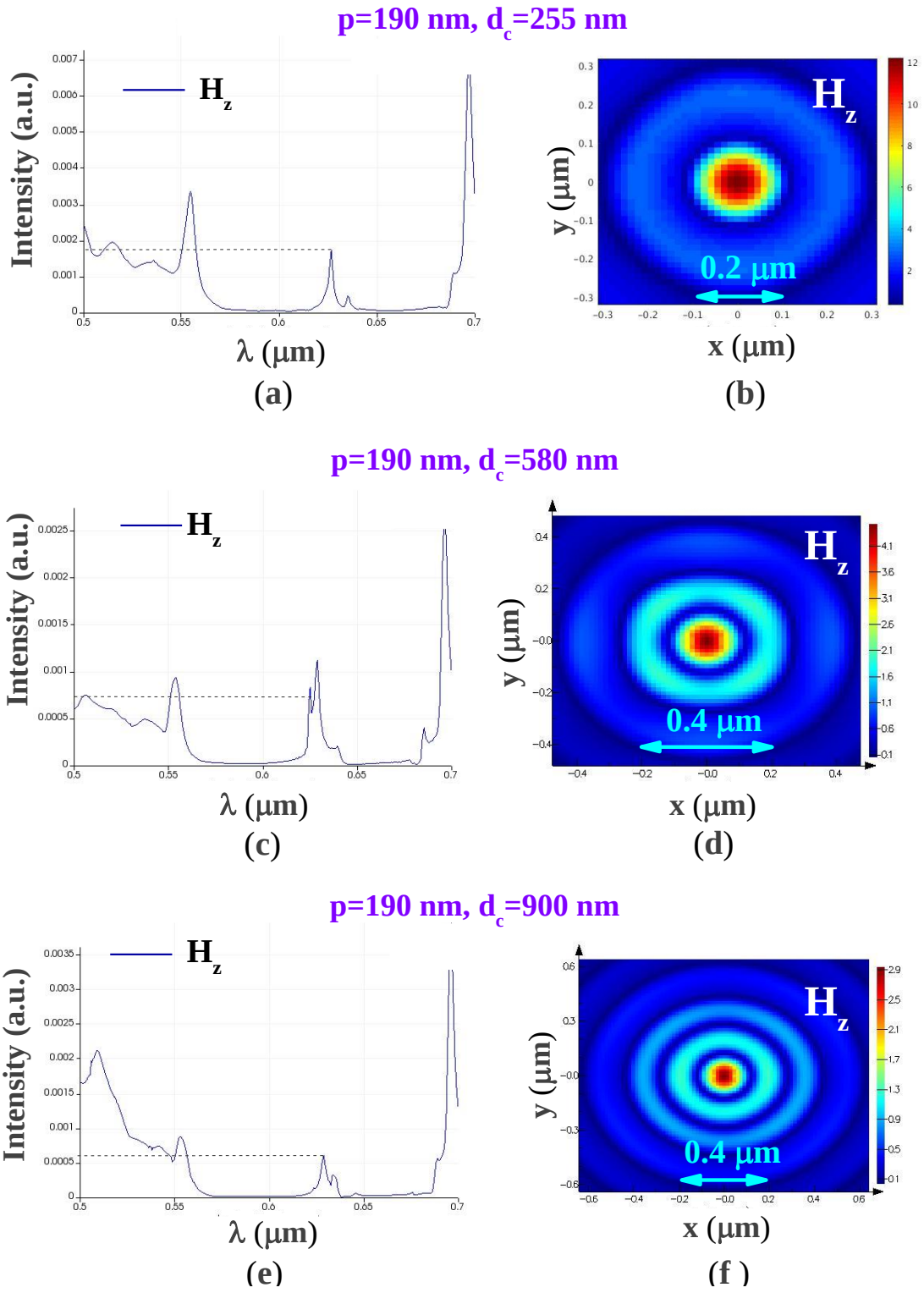

FIG. V.4. (a), (c), (e) The simulated optical resonances at 630 nm, at the emission wavelength of the acceptor, along with the maps of the Hz field depicted in (b), (c), (f).

From the above graphs, we can see that the modes are localized only at the surface of the defect for the smallest cavity diameter in the blue, FIG.V.3.(a), see inlet of the H_z field. The losses can be estimated by the QF, which is around 370. Therefore, this is the design that shows

the highest Purcell enhancement factor (QF/modal volume) with the highest mode intensity. However, for the rest of the designs in the blue and in the red, the modes are localized at a larger surface so we expect the Purcell enhancement to be weaker than the structure with p= 130 nm and d_c=175 nm. Moreover, this is the only configuration that supports a single mode cavity. As it becomes apparent in the FIG. V.3 and V.4, a second mode at longer wavelength begins to become important as the diameter increases, with the simultaneous decrease of the resonance at the desired wavelengths, for both the cases of the resonance in the blue and the red. In FIG. V.5, is shown an example of a structure that supports a photonic bandgap in the blue. The width of the PBG in all the four cases (in the blue and the red) was around 0.1 μm.

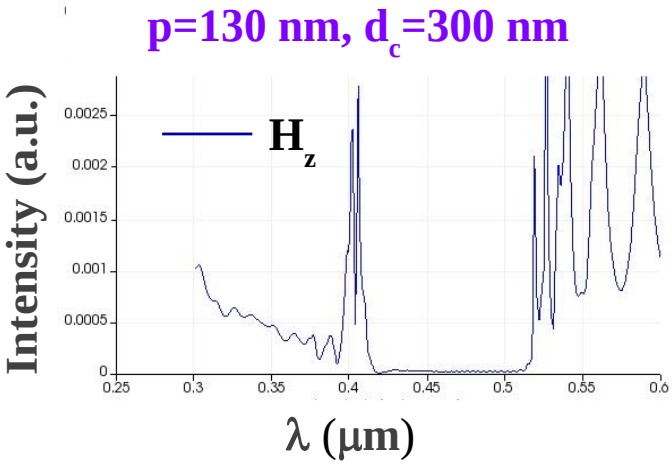

FIG. V.5. The spectra of the simulated band edge modes.

V.5 Fabrication of the photonic structures

The procedure to obtain the final design (carried out by CEA-Leti) involved several steps. At first was the metal organic chemical vapor deposition (MOCVD) in order to obtain the stack of FIG. V.2. This is the typical structure on sapphire for micro-LED applications. For characterisation purposes and in order to eliminate any guided modes and parasitic resonances that can strongly affect the modes in the grating, we opted for a structure on SiO2/Si. Since there was no possibility to grow the InGaN/GaN region on Si, we decided to flip the initial sample and bond it using Ti contact on the appropriate substrate. The next step was to remove the unnecessary layers by etching and then fully etch the desired pattern in order to obtain the circular grating.

As mentioned in an above section, the fabrication was not successful. In fact, it already presented an issue as the bow of the epitaxy sample was not allowing the bonding to the Si substrate. This induced strain resulted either in breaking the samples in pieces or in de-bonding

the wafer. In all the cases, it was not possible to pass to the next step (etching). So, at the end, it was the stacking on a low index layer that was problematic and for that reason we can propose an epi structure with a smaller bow to facilitate the bonding or try to stack it on another material.

V.6 Conclusion

In this chapter, we proposed a way to control the NRET between an InGaN/GaN structure and red CdSe QDs with the help of a circular grating resonator. The goal would have been to observe how the resonances that are supported by the photonic structure allow the impact of the energy transfer between the QW and the QDs at the emission wavelengths of the donor and the acceptor respectively. In a future work, it could be interesting for this fabrication process to be studied in order to eliminate the weak points. In all the cases, here we performed a full study whose realization could give an insight in the relation between the LDOS and the NRET rate.

General conclusion

In this PhD work we addressed the photonic properties of the near field coupling in the frame of LED applications. Based on the non-radiative energy transfer theory, we studied the parameters that affect this dipole-dipole interaction, including the dipole's orientation and the polarization of the donor's emission, the donor-acceptor's separation and the impact of the LDOS on the donor's and the acceptor's emission. Therefore, the thesis was divided in three main sections.

As a first step, the emission of a single InGaN QW located in nanometric distance from the top interface of the structure was analyzed. The extracted from TRPL measurements spontaneous lifetimes, along with analytical calculations based on the Maxwell's equations[54] and the use of a model allowed us to characterize the SQW dipole orientation[188]. The study of three samples with cap layer thicknesses of 5, 8 and 12 nm showed that there is a specific dipole alignment with respect to the substrate for each case. According to our results, this orientation phenomenon is inversely proportional to the QW distance from the interface as 69% of the dipoles are oriented perpendicularly for the 5 nm cap layer, 46% for the 8 nm and only 22% for the 12 nm. Therefore, the thickness of the cap layer can alter the photonic environment of the dipoles in the QW and modify their orientation. Then, as the dipole orientation cannot be directly accessed but only indirectly calculated, we also performed polarization measurements to support our arguments. Following the method of Masui[189], by using a confocal microscope we were able to characterize the polarization ratios based on the polarized photoluminescence of the three samples. For a stronger conclusion, we compared this to a standard (reference) multi QW InGaN/GaN structure, where the QW are buried at 300 nm depth below the top interface. The measurement and the extrapolation of the experimental data to zero excitation power revealed the very different behavior between the SQW and MQW structures[152]. The measurement of the reference sample returns the value obtained by Masui for the polarization ratio to around 90%, suggesting that the polarized emission is in plane with the QW. Moreover, this value does not change when the excitation energy decreases. On the other hand, the polarization ratios that correspond to the three SQW samples decrease from around 0.25 to 0.05 with decreasing excitation power and are inversely proportional to

the quantum barrier value at the spontaneous regime. This suggests that the polarization could be perpendicular in majority. From the results of this chapter, it appears that there is a strong impact of the nanometric interface proximity on the polarization ratio and consequently on the orientation of the emitting dipoles in an InGaN/GaN SQW that in extension, can affect the interaction with any other active medium placed on the top surface in the context of the NRET.

Secondly, we focused on the interaction between the QW and the QDs. The theoretical prediction of the energy transfer that the NRET efficiency scales with R^{-6} does not necessarily apply on our configuration as the environment for the dipole-dipole interaction is not isotropic because of the top interface. For that reason, we performed PL and TRPL results on InGaN-QD samples to determine how the cap layer thickness affects the short-range and long-range coupling. Afterwards, we added SiO_2 spacers in order to further shift the QDs up to 112 nm away from the QW. Overall, three (QW-QD) plus 12 (QW-spacer-QD) samples were studied. A double exponential fit showed that there are two contributions that mainly affect the coupling: one extremely short and one longer lifetime that correspond to the NRET mechanism and the radiative coupling respectively[170]. In low temperature (10-100K) the results showed that as the thinnest cap layer of 5 nm favors the most efficient long-range NRET coupling in a largest range comparing to the 8 and the 12 nm that presented weaker long-range coupling and when the acceptor is placed closer to the donor. In all the cases, this study showed the potential of the NRET coupling mechanism that should not be overlooked when it comes to the LED application.

The final part was devoted to the impact of the photonic density of states created by patterned photonic structures on the NRET between a donor and an acceptor. For that purpose, we conceived two different configurations to study separately the impact on the donor's and the acceptor's emission. The first one was composed by a photonic crystal and a blend of green and red QDs that were playing the role of the donor and the acceptor respectively. By constructing patterns of 300 and 380 nm period respectively we were able to tune the photonic mode density of the PC either with the green or the red emission. The fabricated PC were characterized and although the etching parameters were not optimized, ARPL measurements confirmed that the PC was able to support the photonic modes at the desired wavelengths. Then, although the deposition of the QDs was not homogeneous, we considered that we had obtained a well-mixed blend with equal amount of red and green QDs in close proximity with

each other as demanded by the NRET theory. Although the ARPL clearly showed the impact of the LDOS on the coupling, the coupling mechanisms can only be assessed by performing TRPL measurements. From these, while the impact of optical resonances on the radiative contribution is clear while the QDs are tuned with an optical resonance, it is more complex to assess he demonstration of a non-radiative energy transfer on the basis of the short/non-radiative contribution analysis. All in all, this complex configuration with several parameters to be considered at the same time need further investigation in order to draw clear conclusions.

The second configuration for the same study and goals was a circular grating resonator acting on the interaction between an InGaN SQW donor and red QD acceptor. FDTD simulations were performed and several designs were proposed for the enhancement and the inhibition of the blue and red emission. Nevertheless, the fabrication process presented several limitations that at the time being were not possible to be overcome. In all the cases, the designs exist and it would be an interesting alternative as it can completely inhibit the radiative emission at the donor's wavelength that it was difficult to be studied with the PC and at the same time allow at the NRET to take place.

In conclusion, we have performed a study that tackles all the parameters that can affect the energy transfer. A NRET based micro-LED could lead to an efficient and compact design applied for the enhancement of the color conversion efficiency in the sense of taking into consideration the electrical and optical properties of the QW-QD coupling, along with the interaction with their photonic environment.

References

[1] H. J. Jang, J. Y. Lee, J. Kim, J. Kwak, et J.-H. Park, « Progress of display performances: AR, VR, QLED, and OLED », *Journal of Information Display*, vol. 21, nº 1, p. 1-9, janv. 2020, doi: 10.1080/15980316.2020.1720835.

[2] « OSA | Fabrication, characterization and applications of flexible vertical InGaN micro-light emitting diode arrays ». https://www.osapublishing.org/oe/fulltext.cfm?uri=oe-24-1-699&id=335413 (consulté le 16 mars 2021).

[3] T. Wu *et al.*, « Mini-LED and Micro-LED: Promising Candidates for the Next Generation Display Technology », p. 17, 2018.

[4] J. Herrnsdorf *et al.*, « Active-Matrix GaN Micro Light-Emitting Diode Display With Unprecedented Brightness », *IEEE Transactions on Electron Devices*, vol. 62, nº 6, p. 1918-1925, juin 2015, doi: 10.1109/TED.2015.2416915.

[5] K. Zhang, D. Peng, K. M. Lau, et Z. Liu, « Fully-integrated active matrix programmable UV and blue micro-LED display system-on-panel (SoP) », *Journal of the Society for Information Display*, vol. 25, nº 4, p. 240-248, 2017, doi: https://doi.org/10.1002/jsid.550.

[6] Z. Wang, X. Shan, X. Cui, et P. Tian, « Characteristics and techniques of GaN-based micro-LEDs for application in next-generation display », *J. Semicond.*, vol. 41, nº 4, p. 041606, avr. 2020, doi: 10.1088/1674-4926/41/4/041606.

[7] R. and M. ltd, « Micro-LED Market by Application (Display (Smartwatch, NTE Device (AR HMD, VR HMD), Smartphone, Television, HUD, Digital Signage, Laptop and Monitor, Lighting (General, Automotive), Display Panel Size, Vertical, and Region - Global Forecast to 2026 ». https://www.researchandmarkets.com/reports/5067415/micro-led-market-by-application-display (consulté le 16 mars 2021).

[8] A. Paranjpe, J. Montgomery, S. M. Lee, et C. Morath, « 45-2: Invited Paper: Micro-LED Displays: Key Manufacturing Challenges and Solutions », *SID Symposium Digest of Technical Papers*, vol. 49, nº 1, p. 597-600, 2018, doi: https://doi.org/10.1002/sdtp.12414.

[9] Y. Huang, G. Tan, F. Gou, M.-C. Li, S.-L. Lee, et S.-T. Wu, « Prospects and challenges of mini-LED and micro-LED displays », *J Soc Inf Display*, vol. 27, nº 7, p. 387-401, juill. 2019, doi: 10.1002/jsid.760.

[10] J. Heber, « Nobel Prize 2014: Akasaki, Amano & Nakamura », *Nature Physics*, vol. 10, nº 11, Art. nº 11, nov. 2014, doi: 10.1038/nphys3147.

[11] S. X. Jin, J. Li, J. Z. Li, J. Y. Lin, et H. X. Jiang, « GaN microdisk light emitting diodes », *Appl. Phys. Lett.*, vol. 76, nº 5, p. 631-633, janv. 2000, doi: 10.1063/1.125841.

[12] H. X. Jiang, S. X. Jin, J. Li, J. Shakya, et J. Y. Lin, « III-nitride blue microdisplays », *Appl. Phys. Lett.*, vol. 78, nº 9, p. 1303-1305, févr. 2001, doi: 10.1063/1.1351521.

[13] X. Zhou *et al.*, « Growth, transfer printing and colour conversion techniques towards full-colour micro-LED display », *Progress in Quantum Electronics*, vol. 71, p. 100263, mai 2020, doi: 10.1016/j.pquantelec.2020.100263.

[14] L. Zhang, F. Ou, W. C. Chong, Y. Chen, et Q. Li, « Wafer-scale monolithic hybrid integration of Si-based IC and III–V epi-layers—A mass manufacturable approach for active matrix micro-LED micro-displays », *Journal of the Society for Information Display*, vol. 26, nº 3, p. 137-145, 2018, doi: https://doi.org/10.1002/jsid.649.

[15] C. A. Bower *et al.*, « Emissive displays with transfer-printed assemblies of 8 μm × 15 μm inorganic light-emitting diodes », *Photon. Res., PRJ*, vol. 5, nº 2, p. A23-A29, avr. 2017, doi: 10.1364/PRJ.5.000A23.
[16] Y. Wu, J. Ma, P. Su, L. Zhang, et B. Xia, « Full-Color Realization of Micro-LED Displays », *Nanomaterials*, vol. 10, nº 12, p. 2482, déc. 2020, doi: 10.3390/nano10122482.
[17] A. Even *et al.*, « Enhanced In incorporation in full InGaN heterostructure grown on relaxed InGaN pseudo-substrate », *Appl. Phys. Lett.*, vol. 110, nº 26, p. 262103, juin 2017, doi: 10.1063/1.4989998.
[18] A. Connie, H. Nguyen, S. Sadaf, I. Shih, et Z. Mi, « Engineering the color rendering index of phosphor-free InGaN/(Al)GaN nanowire white light emitting diodes grown by molecular beam epitaxy », *Journal of Vacuum Science & Technology B: Microelectronics and Nanometer Structures*, vol. 32, p. 02C113-02C113, mars 2014, doi: 10.1116/1.4865914.
[19] H. S. El-Ghoroury, M. Yeh, J. C. Chen, X. Li, et C.-L. Chuang, « Growth of monolithic full-color GaN-based LED with intermediate carrier blocking layers », *AIP Advances*, vol. 6, nº 7, p. 075316, juill. 2016, doi: 10.1063/1.4959897.
[20] K. Chung, J. Sui, B. Demory, C.-H. Teng, et P.-C. Ku, « Monolithic integration of individually addressable light-emitting diode color pixels », *Appl. Phys. Lett.*, vol. 110, nº 11, p. 111103, mars 2017, doi: 10.1063/1.4978554.
[21] K. Chung, J. Sui, B. Demory, et P.-C. Ku, « Color mixing from monolithically integrated InGaN-based light-emitting diodes by local strain engineering », *Appl. Phys. Lett.*, vol. 111, nº 4, p. 041101, juill. 2017, doi: 10.1063/1.4995561.
[22] R. Wang, H. P. T. Nguyen, A. T. Connie, J. Lee, I. Shih, et Z. Mi, « Color-tunable, phosphor-free InGaN nanowire light-emitting diode arrays monolithically integrated on silicon », *Opt. Express, OE*, vol. 22, nº 107, p. A1768-A1775, déc. 2014, doi: 10.1364/OE.22.0A1768.
[23] K. Kishino, K. Nagashima, et K. Yamano, « Monolithic Integration of InGaN-Based Nanocolumn Light-Emitting Diodes with Different Emission Colors », *Appl. Phys. Express*, vol. 6, nº 1, p. 012101, déc. 2012, doi: 10.7567/APEX.6.012101.
[24] H. Q. T. Bui *et al.*, « Full-color InGaN/AlGaN nanowire micro light-emitting diodes grown by molecular beam epitaxy: A promising candidate for next generation micro displays », *Micromachines*, vol. 10, nº 8, p. 492, août 2019, doi: 10.3390/mi10080492.
[25] H.-M. Kim *et al.*, « High-Brightness Light Emitting Diodes Using Dislocation-Free Indium Gallium Nitride/Gallium Nitride Multiquantum-Well Nanorod Arrays », *Nano Lett.*, vol. 4, nº 6, p. 1059-1062, juin 2004, doi: 10.1021/nl049615a.
[26] M. B. de la Mora, O. Amelines-Sarria, B. M. Monroy, C. D. Hernández-Pérez, et J. E. Lugo, « Materials for downconversion in solar cells: Perspectives and challenges », *Solar Energy Materials and Solar Cells*, vol. 165, p. 59-71, juin 2017, doi: 10.1016/j.solmat.2017.02.016.
[27] L. Dumont *et al.*, « Down-shifting Si-based layer for Si solar applications », *Solar Energy Materials and Solar Cells*, vol. 169, p. 132-144, sept. 2017, doi: 10.1016/j.solmat.2017.05.011.
[28] J. K. Han *et al.*, « Phosphor Development and Integration for Near-UV LED Solid State Lighting », *ECS J. Solid State Sci. Technol.*, vol. 2, nº 2, p. R3138, déc. 2012, doi: 10.1149/2.014302jss.
[29] H. Mattoussi *et al.*, « Self-Assembly of CdSe−ZnS Quantum Dot Bioconjugates Using an Engineered Recombinant Protein », *J. Am. Chem. Soc.*, vol. 122, nº 49, p. 12142-12150, déc. 2000, doi: 10.1021/ja002535y.

[30] Y. Yin *et al.*, « Full-Color Micro-LED Display with CsPbBr3 Perovskite and CdSe Quantum Dots as Color Conversion Layers », *Advanced Materials Technologies*, vol. 5, nº 8, p. 2000251, 2020, doi: https://doi.org/10.1002/admt.202000251.
[31] R. S. Sanchez, M. S. de la Fuente, I. Suarez, G. Muñoz-Matutano, J. P. Martinez-Pastor, et I. Mora-Sero, « Tunable light emission by exciplex state formation between hybrid halide perovskite and core/shell quantum dots: Implications in advanced LEDs and photovoltaics », *Science Advances*, vol. 2, nº 1, p. e1501104, janv. 2016, doi: 10.1126/sciadv.1501104.
[32] J. McKittrick et L. E. Shea-Rohwer, « Review: Down Conversion Materials for Solid-State Lighting », *Journal of the American Ceramic Society*, vol. 97, nº 5, p. 1327-1352, 2014, doi: https://doi.org/10.1111/jace.12943.
[33] H. Chen *et al.*, « Exploring a particle-size-reduction strategy of YAG:Ce phosphor via a chemical breakdown method », *Journal of Rare Earths*, août 2020, doi: 10.1016/j.jre.2020.07.023.
[34] P. Pust *et al.*, « Narrow-band red-emitting Sr[LiAl 3 N 4]:Eu 2+ as a next-generation LED-phosphor material », *Nature Materials*, vol. 13, nº 9, Art. nº 9, sept. 2014, doi: 10.1038/nmat4012.
[35] Y. Shirasaki, G. J. Supran, M. G. Bawendi, et V. Bulović, « Emergence of colloidal quantum-dot light-emitting technologies », *Nature Photon*, vol. 7, nº 1, p. 13-23, janv. 2013, doi: 10.1038/nphoton.2012.328.
[36] H. Li *et al.*, « Broadband full-color monolithic InGaN light-emitting diodes by self-assembled InGaN quantum dots », *Scientific Reports*, vol. 6, nº 1, Art. nº 1, oct. 2016, doi: 10.1038/srep35217.
[37] D.-S. Kim, S.-Y. Kim, J.-H. Jung, et S.-Y. Shin, « High-quality Imaging Micro-LED Display based on Quantum Dot CSP Technology », *Electronic Imaging*, vol. 2018, nº 16, p. 185-1-185-5, janv. 2018, doi: 10.2352/ISSN.2470-1173.2018.16.COLOR-185.
[38] Z. Liu *et al.*, « Micro-light-emitting diodes with quantum dots in display technology », *Light Sci Appl*, vol. 9, nº 1, p. 83, déc. 2020, doi: 10.1038/s41377-020-0268-1.
[39] J. Zhao *et al.*, « Efficient CdSe/CdS quantum dot light-emitting diodes using a thermally polymerized hole transport layer », *Nano Lett*, vol. 6, nº 3, p. 463-467, mars 2006, doi: 10.1021/nl052417e.
[40] arno_gm, « A Study on Aerosol Jet Printing in LED Module Manufacturing — LED professional - LED Lighting Technology, Application Magazine ». https://www.led-professional.com/resources-1/articles/a-study-on-aerosol-jet-printing-in-led-module-manufacturing (consulté le 5 avril 2021).
[41] W. Mei *et al.*, « High-resolution, full-color quantum dot light-emitting diode display fabricated via photolithography approach », *Nano Res.*, vol. 13, nº 9, p. 2485-2491, sept. 2020, doi: 10.1007/s12274-020-2883-9.
[42] P. Yang, L. Zhang, D. J. Kang, R. Strahl, et T. Kraus, « High-Resolution Inkjet Printing of Quantum Dot Light-Emitting Microdiode Arrays », *Advanced Optical Materials*, vol. 8, nº 1, p. 1901429, 2020, doi: https://doi.org/10.1002/adom.201901429.
[43] J. G. Tait *et al.*, « Uniform Aerosol Jet printed polymer lines with 30µm width for 140ppi resolution RGB organic light emitting diodes », *Organic Electronics*, vol. 22, p. 40-43, juill. 2015, doi: 10.1016/j.orgel.2015.03.034.
[44] H.-Y. Lin *et al.*, « Optical cross-talk reduction in a quantum-dot-based full-color micro-light-emitting-diode display by a lithographic-fabricated photoresist mold », *Photon. Res.*, vol. 5, nº 5, p. 411, oct. 2017, doi: 10.1364/PRJ.5.000411.
[45] A. J. Trindade *et al.*, « Heterogeneous integration of gallium nitride light-emitting diodes on diamond and silica by transfer printing », *Opt. Express, OE*, vol. 23, nº 7, p. 9329-9338, avr. 2015, doi: 10.1364/OE.23.009329.

[46] Y. S. Y. Sato, N. T. N. Takahashi, et S. S. S. Sato, « Full-Color Fluorescent Display Devices Using a Near-UV Light-Emitting Diode », *Jpn. J. Appl. Phys.*, vol. 35, nº 7A, p. L838, juill. 1996, doi: 10.1143/JJAP.35.L838.
[47] B. H. Kim *et al.*, « Multilayer Transfer Printing for Pixelated, Multicolor Quantum Dot Light-Emitting Diodes », *ACS nano*, vol. 10, nº 5, p. 4920-4925, mai 2016, doi: 10.1021/acsnano.5b06387.
[48] S. Chanyawadee *et al.*, « Increased Color-Conversion Efficiency in Hybrid Light-Emitting Diodes utilizing Non-Radiative Energy Transfer », *Adv. Mater.*, vol. 22, nº 5, p. 602-606, févr. 2010, doi: 10.1002/adma.200902262.
[49] M. Achermann, M. A. Petruska, S. Kos, D. L. Smith, D. D. Koleske, et V. I. Klimov, « Energy-transfer pumping of semiconductor nanocrystals using an epitaxial quantum well », *Nature*, vol. 429, nº 6992, p. 642-646, juin 2004, doi: 10.1038/nature02571.
[50] S. Nizamoglu, E. Sari, J. Baek, I. Lee, et H. V. Demir, « Green/Yellow Solid-State Lighting via Radiative and Nonradiative Energy Transfer Involving Colloidal Semiconductor Nanocrystals », *IEEE Journal of Selected Topics in Quantum Electronics*, vol. 15, nº 4, p. 1163-1170, juill. 2009, doi: 10.1109/JSTQE.2009.2015680.
[51] S. Lu et A. Madhukar, « Nonradiative Resonant Excitation Transfer from Nanocrystal Quantum Dots to Adjacent Quantum Channels », *Nano Lett.*, vol. 7, nº 11, p. 3443-3451, nov. 2007, doi: 10.1021/nl0719731.
[52] R. R. Chance, A. Prock, et R. Silbey, « Comments on the classical theory of energy transfer. II. Extension to higher multipoles and anisotropic media », *The Journal of Chemical Physics*, vol. 65, nº 7, p. 2527-2531, oct. 1976, doi: 10.1063/1.433457.
[53] T. Förster, « Experimentelle und theoretische Untersuchung des zwischenmolekularen Übergangs von Elektronenanregungsenergie », *Zeitschrift für Naturforschung A*, vol. 4, nº 5, p. 321-327, mai 1949, doi: 10.1515/zna-1949-0501.
[54] L. Novotny et B. Hecht, *Principles of Nano-Optics*. Cambridge University Press, 2012.
[55] P. G. Wu et L. Brand, « Resonance Energy Transfer: Methods and Applications », *Analytical Biochemistry*, vol. 218, nº 1, p. 1-13, avr. 1994, doi: 10.1006/abio.1994.1134.
[56] J. J. Rindermann, G. Pozina, B. Monemar, L. Hultman, H. Amano, et P. G. Lagoudakis, « Dependence of Resonance Energy Transfer on Exciton Dimensionality », *Phys. Rev. Lett.*, vol. 107, nº 23, p. 236805, nov. 2011, doi: 10.1103/PhysRevLett.107.236805.
[57] P. L. Hernández-Martínez, A. O. Govorov, et H. V. Demir, « Förster-Type Nonradiative Energy Transfer for Assemblies of Arrayed Nanostructures: Confinement Dimension vs Stacking Dimension », *The Journal of Physical Chemistry C*, vol. 118, nº 9, p. 4951-4958, mars 2014, doi: 10.1021/jp409833b.
[58] A. Hillisch, M. Lorenz, et S. Diekmann, « Recent advances in FRET: distance determination in protein–DNA complexes », *Current Opinion in Structural Biology*, vol. 11, nº 2, p. 201-207, avr. 2001, doi: 10.1016/S0959-440X(00)00190-1.
[59] H. Chang, L. Tang, Y. Wang, J. Jiang, et J. Li, « Graphene Fluorescence Resonance Energy Transfer Aptasensor for the Thrombin Detection », *Analytical Chemistry*, vol. 82, nº 6, p. 2341-2346, mars 2010, doi: 10.1021/ac9025384.
[60] I. L. Medintz, A. R. Clapp, H. Mattoussi, E. R. Goldman, B. Fisher, et J. M. Mauro, « Self-assembled nanoscale biosensors based on quantum dot FRET donors », *Nature Materials*, vol. 2, nº 9, p. 630-638, sept. 2003, doi: 10.1038/nmat961.
[61] G. D. Scholes, C. Curutchet, B. Mennucci, R. Cammi, et J. Tomasi, « How Solvent Controls Electronic Energy Transfer and Light Harvesting », *The Journal of Physical Chemistry B*, vol. 111, nº 25, p. 6978-6982, juin 2007, doi: 10.1021/jp072540p.

[62] C. Curutchet, J. Kongsted, A. Muñoz-Losa, H. Hossein-Nejad, G. D. Scholes, et B. Mennucci, « Photosynthetic Light-Harvesting Is Tuned by the Heterogeneous Polarizable Environment of the Protein », *Journal of the American Chemical Society*, vol. 133, nº 9, p. 3078-3084, mars 2011, doi: 10.1021/ja110053y.
[63] X. Fan, T. Wu, B. Liu, R. Zhang, H.-C. Kuo, et Z. Chen, « Recent developments of quantum dot based micro-LED based on non-radiative energy transfer mechanism », p. 17, 2021.
[64] S. Chanyawadee *et al.*, « Increased Color-Conversion Efficiency in Hybrid Light-Emitting Diodes utilizing Non-Radiative Energy Transfer », *Advanced Materials*, vol. 22, nº 5, p. 602-606, doi: 10.1002/adma.200902262.
[65] X. Xu et H. Wang, « Resonant energy transfer between patterned InGaN/GaN quantum wells and CdSe/ZnS quantum dots », *Nanoscale*, vol. 8, nº 1, p. 342-347, déc. 2015, doi: 10.1039/C5NR05078B.
[66] Z. Zhuang *et al.*, « Improvement of color conversion and efficiency droop in hybrid light-emitting diodes utilizing an efficient non-radiative resonant energy transfer », *Applied Physics Letters*, vol. 109, nº 14, p. 141105, oct. 2016, doi: 10.1063/1.4964403.
[67] F. Zhang *et al.*, « Nonradiative energy transfer between colloidal quantum dot-phosphors and nanopillar nitride LEDs », *Opt. Express*, vol. 20, nº S2, p. A333, mars 2012, doi: 10.1364/OE.20.00A333.
[68] S.-W. H. Chen *et al.*, « Full-color monolithic hybrid quantum dot nanoring micro light-emitting diodes with improved efficiency using atomic layer deposition and nonradiative resonant energy transfer », p. 7.
[69] C. Krishnan *et al.*, « Hybrid photonic crystal light-emitting diode renders 123% color conversion effective quantum yield », *Optica*, vol. 3, nº 5, p. 503, mai 2016, doi: 10.1364/OPTICA.3.000503.
[70] E. M. Purcell, « Spontaneous Emission Probabilities at Radio Frequencies », in *Confined Electrons and Photons: New Physics and Applications*, E. Burstein et C. Weisbuch, Éd., in NATO ASI Series. Boston, MA: Springer US, 1995, p. 839-839. doi: 10.1007/978-1-4615-1963-8_40.
[71] K. H. Drexhage, « Influence of a dielectric interface on fluorescence decay time », *Journal of Luminescence*, vol. 1-2, p. 693-701, janv. 1970, doi: 10.1016/0022-2313(70)90082-7.
[72] W. L. Barnes, « Fluorescence near interfaces: The role of photonic mode density », *Journal of Modern Optics*, vol. 45, nº 4, p. 661-699, avr. 1998, doi: 10.1080/09500349808230614.
[73] P. Goy, J. M. Raimond, M. Gross, et S. Haroche, « Observation of Cavity-Enhanced Single-Atom Spontaneous Emission », *Phys. Rev. Lett.*, vol. 50, nº 24, p. 1903-1906, juin 1983, doi: 10.1103/PhysRevLett.50.1903.
[74] P. Lodahl *et al.*, « Controlling the dynamics of spontaneous emission from quantum dots by photonic crystals », *Nature*, vol. 430, nº 7000, Art. nº 7000, août 2004, doi: 10.1038/nature02772.
[75] L. Novotny et N. van Hulst, « Antennas for light », *Nature Photonics*, vol. 5, nº 2, Art. nº 2, févr. 2011, doi: 10.1038/nphoton.2010.237.
[76] A. Kinkhabwala, Z. Yu, S. Fan, Y. Avlasevich, K. Müllen, et W. E. Moerner, « Large single-molecule fluorescence enhancements produced by a bowtie nanoantenna », *Nature Photonics*, vol. 3, nº 11, Art. nº 11, nov. 2009, doi: 10.1038/nphoton.2009.187.
[77] M. Hopmeier, W. Guss, M. Deussen, E. O. Göbel, et R. F. Mahrt, « Enhanced Dipole-Dipole Interaction in a Polymer Microcavity », *Phys. Rev. Lett.*, vol. 82, nº 20, p. 4118-4121, mai 1999, doi: 10.1103/PhysRevLett.82.4118.

[78] P. Andrew et W. L. Barnes, « Förster energy transfer in an optical microcavity », *Science*, vol. 290, nº 5492, p. 785-788, oct. 2000.
[79] C. E. Finlayson, D. S. Ginger, et N. C. Greenham, « Enhanced Förster energy transfer in organic/inorganic bilayer optical microcavities », *Chemical Physics Letters*, vol. 338, nº 2, p. 83-87, avr. 2001, doi: 10.1016/S0009-2614(01)00247-0.
[80] T. Nakamura, M. Fujii, K. Imakita, et S. Hayashi, « Modification of energy transfer from Si nanocrystals to ${\mathrm{Er}}^{3+}$ near a Au thin film », *Phys. Rev. B*, vol. 72, nº 23, p. 235412, déc. 2005, doi: 10.1103/PhysRevB.72.235412.
[81] H. T. Dung, L. Knöll, et D.-G. Welsch, « Intermolecular energy transfer in the presence of dispersing and absorbing media », *Phys. Rev. A*, vol. 65, nº 4, p. 043813, avr. 2002, doi: 10.1103/PhysRevA.65.043813.
[82] V. Faessler *et al.*, « Accelerating fluorescence resonance energy transfer with plasmonic nanoresonators », *Chemical Physics Letters*, vol. 508, nº 1, p. 67-70, mai 2011, doi: 10.1016/j.cplett.2011.03.088.
[83] L. Zhao, T. Ming, L. Shao, H. Chen, et J. Wang, « Plasmon-Controlled Förster Resonance Energy Transfer », *J. Phys. Chem. C*, vol. 116, nº 14, p. 8287-8296, avr. 2012, doi: 10.1021/jp300916a.
[84] J. de Torres *et al.*, « Plasmonic Nanoantennas Enable Forbidden Förster Dipole–Dipole Energy Transfer and Enhance the FRET Efficiency », *Nano Lett.*, vol. 16, nº 10, p. 6222-6230, oct. 2016, doi: 10.1021/acs.nanolett.6b02470.
[85] P. Ghenuche *et al.*, « Matching Nanoantenna Field Confinement to FRET Distances Enhances Förster Energy Transfer Rates », *Nano Lett.*, vol. 15, nº 9, p. 6193-6201, sept. 2015, doi: 10.1021/acs.nanolett.5b02535.
[86] S. Bidault, A. Devilez, P. Ghenuche, B. Stout, N. Bonod, et J. Wenger, « Competition between Förster Resonance Energy Transfer and Donor Photodynamics in Plasmonic Dimer Nanoantennas », *ACS Photonics*, vol. 3, nº 5, p. 895-903, mai 2016, doi: 10.1021/acsphotonics.6b00148.
[87] « Förster Energy Transfer in an Optical Microcavity | Science ». http://science.sciencemag.org/content/290/5492/785 (consulté le 11 juin 2018).
[88] P. Ghenuche, J. de Torres, S. B. Moparthi, V. Grigoriev, et J. Wenger, « Nanophotonic Enhancement of the Förster Resonance Energy-Transfer Rate with Single Nanoapertures », *Nano Lett.*, vol. 14, nº 8, p. 4707-4714, août 2014, doi: 10.1021/nl5018145.
[89] J. de Torres, P. Ghenuche, S. B. Moparthi, V. Grigoriev, et J. Wenger, « FRET Enhancement in Aluminum Zero-Mode Waveguides », *ChemPhysChem*, vol. 16, nº 4, p. 782-788, 2015, doi: https://doi.org/10.1002/cphc.201402651.
[90] M. Lunz *et al.*, « Surface Plasmon Enhanced Energy Transfer between Donor and Acceptor CdTe Nanocrystal Quantum Dot Monolayers », *Nano Lett.*, vol. 11, nº 8, p. 3341-3345, août 2011, doi: 10.1021/nl201714y.
[91] X. Zhang *et al.*, « Experimental and theoretical investigation of the distance dependence of localized surface plasmon coupled Förster resonance energy transfer », *ACS Nano*, vol. 8, nº 2, p. 1273-1283, févr. 2014, doi: 10.1021/nn406530m.
[92] P. M. de Roque, N. F. van Hulst, et R. Sapienza, « Nanophotonic boost of intermolecular energy transfer », *New J. Phys.*, vol. 17, nº 11, p. 113052, nov. 2015, doi: 10.1088/1367-2630/17/11/113052.
[93] J. de Torres, P. Ferrand, G. Colas des Francs, et J. Wenger, « Coupling Emitters and Silver Nanowires to Achieve Long-Range Plasmon-Mediated Fluorescence Energy Transfer », *ACS Nano*, vol. 10, nº 4, p. 3968-3976, avr. 2016, doi: 10.1021/acsnano.6b00287.

[94] G. Colas des Francs, C. Girard, et O. J. F. Martin, « Fluorescence resonant energy transfer in the optical near field », *Phys. Rev. A*, vol. 67, nº 5, p. 053805, mai 2003, doi: 10.1103/PhysRevA.67.053805.
[95] A. O. Govorov, J. Lee, et N. A. Kotov, « Theory of plasmon-enhanced F\"orster energy transfer in optically excited semiconductor and metal nanoparticles », *Phys. Rev. B*, vol. 76, nº 12, p. 125308, sept. 2007, doi: 10.1103/PhysRevB.76.125308.
[96] C. A. Marocico, X. Zhang, et A. L. Bradley, « A theoretical investigation of the influence of gold nanosphere size on the decay and energy transfer rates and efficiencies of quantum emitters », *J. Chem. Phys.*, vol. 144, nº 2, p. 024108, janv. 2016, doi: 10.1063/1.4939206.
[97] R. Vincent et R. Carminati, « Magneto-optical control of F\"orster energy transfer », *Phys. Rev. B*, vol. 83, nº 16, p. 165426, avr. 2011, doi: 10.1103/PhysRevB.83.165426.
[98] A. Konrad, M. Metzger, A. M. Kern, M. Brecht, et A. J. Meixner, « Controlling the dynamics of Förster resonance energy transfer inside a tunable sub-wavelength Fabry–Pérot-resonator », *Nanoscale*, vol. 7, nº 22, p. 10204-10209, 2015, doi: 10.1039/C5NR02027A.
[99] F. Schleifenbaum, A. M. Kern, A. Konrad, et A. J. Meixner, « Dynamic control of Förster energy transfer in a photonic environment », *Physical Chemistry Chemical Physics*, vol. 16, nº 25, p. 12812-12817, 2014, doi: 10.1039/C4CP01306A.
[100] J. Enderlein, « Modification of Förster Resonance Energy Transfer Efficiencyat Interfaces », *International Journal of Molecular Sciences*, vol. 13, nº 11, Art. nº 11, nov. 2012, doi: 10.3390/ijms131115227.
[101] T. Nakamura, M. Fujii, S. Miura, M. Inui, et S. Hayashi, « Enhancement and suppression of energy transfer from Si nanocrystals to Er ions through a control of the photonic mode density », *Phys. Rev. B*, vol. 74, nº 4, p. 045302, juill. 2006, doi: 10.1103/PhysRevB.74.045302.
[102] C. Blum *et al.*, « Nanophotonic Control of the Förster Resonance Energy Transfer Efficiency », *Phys. Rev. Lett.*, vol. 109, nº 20, p. 203601, nov. 2012, doi: 10.1103/PhysRevLett.109.203601.
[103] M. Wubs et W. L. Vos, « Förster resonance energy transfer rate in any dielectric nanophotonic medium with weak dispersion », *New J. Phys.*, vol. 18, nº 5, p. 053037, mai 2016, doi: 10.1088/1367-2630/18/5/053037.
[104] M. J. A. de Dood, J. Knoester, A. Tip, et A. Polman, « Förster transfer and the local optical density of states in erbium-doped silica », *Phys. Rev. B*, vol. 71, nº 11, p. 115102, mars 2005, doi: 10.1103/PhysRevB.71.115102.
[105] F. T. Rabouw, S. A. den Hartog, T. Senden, et A. Meijerink, « Photonic effects on the Förster resonance energy transfer efficiency », *Nat Commun*, vol. 5, nº 1, p. 3610, mai 2014, doi: 10.1038/ncomms4610.
[106] R. Sprik, B. A. van Tiggelen, et A. Lagendijk, « Optical emission in periodic dielectrics », *Europhys. Lett.*, vol. 35, nº 4, p. 265-270, août 1996, doi: 10.1209/epl/i1996-00564-y.
[107] Z. Yang *et al.*, « Energy transfer between fluorescent dyes in photonic crystals », *Opt. Lett.*, vol. 33, nº 17, p. 1963, sept. 2008, doi: 10.1364/OL.33.001963.
[108] H. Zhang, J. Lv, et Z. Jia, « Efficient Fluorescence Resonance Energy Transfer between Quantum Dots and Gold Nanoparticles Based on Porous Silicon Photonic Crystal for DNA Detection », *Sensors*, vol. 17, nº 5, p. 1078, mai 2017, doi: 10.3390/s17051078.
[109] D. J. Roth *et al.*, « Förster Resonance Energy Transfer inside Hyperbolic Metamaterials », *ACS Photonics*, vol. 5, nº 11, p. 4594-4603, nov. 2018, doi: 10.1021/acsphotonics.8b01083.

[110] I. A. Sukhoivanov et I. V. Guryev, « Introduction to photonic crystals », *Springer Series in Optical Sciences*, vol. 152, p. 1-12, 2010, doi: 10.1007/978-3-642-02646-1_1.
[111] J. J. D. Joannopoulos, S. Johnson, J. N. J. Winn, et R. R. D. Meade, *Photonic crystals: molding the flow of light*. 2008. doi: 10.1063/1.1586781.
[112] V. E. Centrale et P. C. View, *Physics of Slow Bloch Modes and Their Applications Photonic Crystals : Physics and Technology*, nº January. 2016. doi: 10.1007/978-88-470-0844-1.
[113] T. Baba, « Slow light in photonic crystals », *Nature Photonics*, vol. 2, nº 8, p. 465-473, 2008, doi: 10.1038/nphoton.2008.146.
[114] L. Novotny, « Allowed and forbidden light in near-field optics II Interacting dipolar particles », *Journal of the Optical Society of America A*, vol. 14, nº 1, p. 105, janv. 1997, doi: 10.1364/JOSAA.14.000105.
[115] L. Novotny, « Allowed and forbidden light in near-field optics I A single dipolar light source », *Journal of the Optical Society of America A*, vol. 14, nº 1, p. 91, janv. 1997, doi: 10.1364/JOSAA.14.000091.
[116] L. Novotny et B. Hecht, *Principles of nano-optics*. Cambridge ; New York: Cambridge University Press, 2006.
[117] T. D. Schmidt *et al.*, « Evidence for non-isotropic emitter orientation in a red phosphorescent organic light-emitting diode and its implications for determining the emitter's radiative quantum efficiency », *Applied Physics Letters*, vol. 99, nº 16, p. 163302, oct. 2011, doi: 10.1063/1.3653475.
[118] M. Flämmich *et al.*, « Oriented phosphorescent emitters boost OLED efficiency », *Organic Electronics*, vol. 12, nº 10, p. 1663-1668, oct. 2011, doi: 10.1016/j.orgel.2011.06.011.
[119] H. Chen, H. Fu, Z. Lu, X. Huang, et Y. Zhao, « Optical properties of highly polarized InGaN light-emitting diodes modified by plasmonic metallic grating », *Optics Express*, vol. 24, nº 10, p. A856, mai 2016, doi: 10.1364/OE.24.00A856.
[120] Y. Kuo *et al.*, « Surface plasmon coupling with radiating dipole for enhancing the emission efficiency of a light-emitting diode », *Optics Express*, vol. 19, nº S4, p. A914, juill. 2011, doi: 10.1364/OE.19.00A914.
[121] M. Wang *et al.*, « Metasurface integrated high energy efficient and high linearly polarized InGaN/GaN light emitting diode », *Nanoscale*, vol. 9, nº 26, p. 9104-9111, 2017, doi: 10.1039/C7NR00539C.
[122] S.-Y. Kim *et al.*, « Organic Light-Emitting Diodes with 30% External Quantum Efficiency Based on a Horizontally Oriented Emitter », *Advanced Functional Materials*, vol. 23, nº 31, p. 3896-3900, 2013, doi: 10.1002/adfm.201300104.
[123] K.-M. Song *et al.*, « Characteristics of indium incorporation in InGaN/GaN multiple quantum wells grown on a-plane and c-plane GaN », *Applied Physics Letters*, vol. 100, nº 21, p. 212103, mai 2012, doi: 10.1063/1.4720507.
[124] H.-H. Huang et Y.-R. Wu, « Light emission polarization properties of semipolar InGaN/GaN quantum well », *Journal of Applied Physics*, vol. 107, nº 5, p. 053112, mars 2010, doi: 10.1063/1.3327794.
[125] H. Masui, H. Yamada, K. Iso, S. Nakamura, et S. P. DenBaars, « Optical polarization characteristics of *m* -oriented InGaN/GaN light-emitting diodes with various indium compositions in single-quantum-well structure », *Journal of Physics D: Applied Physics*, vol. 41, nº 22, p. 225104, nov. 2008, doi: 10.1088/0022-3727/41/22/225104.
[126] N. F. Gardner, J. C. Kim, J. J. Wierer, Y. C. Shen, et M. R. Krames, « Polarization anisotropy in the electroluminescence of m-plane InGaN–GaN multiple-quantum-well light-emitting diodes », *Applied Physics Letters*, vol. 86, nº 11, p. 111101, mars 2005, doi: 10.1063/1.1875765.

[127] K. Domen, K. Horino, A. Kuramata, et T. Tanahashi, « Analysis of polarization anisotropy along the c axis in the photoluminescence of wurtzite GaN », *Applied Physics Letters*, vol. 71, nº 14, p. 1996-1998, oct. 1997, doi: 10.1063/1.119766.
[128] Y. J. Sun, O. Brandt, M. Ramsteiner, H. T. Grahn, et K. H. Ploog, « Polarization anisotropy of the photoluminescence of M-plane (In,Ga)N/GaN multiple quantum wells », *Applied Physics Letters*, vol. 82, nº 22, p. 3850-3852, juin 2003, doi: 10.1063/1.1579563.
[129] W. Jhe, A. Anderson, E. A. Hinds, D. Meschede, L. Moi, et S. Haroche, « Suppression of spontaneous decay at optical frequencies: Test of vacuum-field anisotropy in confined space », *Physical Review Letters*, vol. 58, nº 7, p. 666-669, févr. 1987, doi: 10.1103/PhysRevLett.58.666.
[130] M. Pelton, « Modified spontaneous emission in nanophotonic structures. », *Nature Photonics*, vol. 9, nº 7, p. 427-427-435, juill. 2015, doi: 10.1038/nphoton.2015.103.
[131] E. Purcell, « Spontaneous emission probabilities at radio frequencies », in *Physical Review*, 1946, p. 681. Consulté le: 18 février 2019. [En ligne]. Disponible sur: http://prola.aps.org/pdf/PR/v69/i11-12/p674_2
[132] C.-Y. Cho et S.-J. Park, « Enhanced optical output and reduction of the quantum-confined Stark effect in surface plasmon-enhanced green light-emitting diodes with gold nanoparticles », *Optics Express*, vol. 24, nº 7, p. 7488, avr. 2016, doi: 10.1364/OE.24.007488.
[133] R. M. Amos et W. L. Barnes, « Modification of the spontaneous emission rate of Eu 3 + ions close to a thin metal mirror », *Physical Review B*, vol. 55, nº 11, p. 7249-7254, mars 1997, doi: 10.1103/PhysRevB.55.7249.
[134] P. Zhao et H. Zhao, « Analysis of light extraction efficiency enhancement for thin-film-flip-chip InGaN quantum wells light-emitting diodes with GaN micro-domes », *Optics Express*, vol. 20, nº S5, p. A765, sept. 2012, doi: 10.1364/OE.20.00A765.
[135] P. Lodahl *et al.*, « Controlling the dynamics of spontaneous emission from quantum dots by photonic crystals », *Nature*, vol. 430, nº 7000, p. 654-657, août 2004, doi: 10.1038/nature02772.
[136] Y. Yamamoto, S. Machida, Y. Horikoshi, K. Igeta, et G. Björk, « Enhanced and inhibited spontaneous emission of free excitons in GaAs quantum wells in a microcavity », *Optics Communications*, vol. 80, nº 5, p. 337-342, janv. 1991, doi: 10.1016/0030-4018(91)90419-E.
[137] J. Bleuse *et al.*, « Inhibition, Enhancement, and Control of Spontaneous Emission in Photonic Nanowires », *Phys. Rev. Lett.*, vol. 106, nº 10, p. 103601, mars 2011, doi: 10.1103/PhysRevLett.106.103601.
[138] E. Yablonovitch, « Inhibited Spontaneous Emission in Solid-State Physics and Electronics », *Physical Review Letters*, vol. 58, nº 20, p. 2059-2062, mai 1987, doi: 10.1103/PhysRevLett.58.2059.
[139] J. Claudon *et al.*, « A highly efficient single-photon source based on a quantum dot in a photonic nanowire », *Nature Photonics*, vol. 4, nº 3, p. 174-177, mars 2010, doi: 10.1038/nphoton.2009.287x.
[140] K. H. Drexhage, « Influence of a dielectric interface on fluorescence decay time », *Journal of Luminescence*, vol. 1-2, p. 693-701, janv. 1970, doi: 10.1016/0022-2313(70)90082-7.
[141] H. Benisty, R. Stanley, et M. Mayer, « Method of source terms for dipole emission modification in modes of arbitrary planar structures », *J. Opt. Soc. Am. A, JOSAA*, vol. 15, nº 5, p. 1192-1201, mai 1998, doi: 10.1364/JOSAA.15.001192.

[142] W. Lukosz, « Theory of optical-environment-dependent spontaneous-emission rates for emitters in thin layers », *Physical Review B*, vol. 22, nº 6, p. 3030-3038, sept. 1980, doi: 10.1103/PhysRevB.22.3030.
[143] W. Lukosz et R. E. Kunz, « Light emission by magnetic and electric dipoles close to a plane dielectric interface II Radiation patterns of perpendicular oriented dipoles », *Journal of the Optical Society of America*, vol. 67, nº 12, p. 1615, déc. 1977, doi: 10.1364/JOSA.67.001615.
[144] J. P. Dowling, « Dipole emission in finite photonic bandgap structures: an exactly solvable one-dimensional model », *Journal of Lightwave Technology*, vol. 17, nº 11, p. 2142-2151, nov. 1999, doi: 10.1109/50.803005.
[145] Y. Mazuz-Harpaz, K. Cohen, B. Laikhtman, R. Rapaport, K. West, et L. N. Pfeiffer, « Radiative lifetimes of dipolar excitons in double quantum wells », *Phys. Rev. B*, vol. 95, nº 15, p. 155302, avr. 2017, doi: 10.1103/PhysRevB.95.155302.
[146] F. A. Inam *et al.*, « Modification of spontaneous emission from nanodiamond colour centres on a structured surface », *New J. Phys.*, vol. 13, nº 7, p. 073012, juill. 2011, doi: 10.1088/1367-2630/13/7/073012.
[147] L. Penninck, F. Steinbacher, R. Krause, et K. Neyts, « Determining emissive dipole orientation in organic light emitting devices by decay time measurement », *ORGANIC ELECTRONICS*, vol. 13, nº 12, p. 3079-3084, 2012, doi: http://dx.doi.org/10.1016/j.orgel.2012.09.014.
[148] H. Masui, N. N. Fellows, S. Nakamura, et S. P. DenBaars, « Optical polarization characteristics of light emission from sidewalls of primary-color light-emitting diodes », *Semiconductor Science and Technology*, vol. 23, nº 7, p. 072001, juill. 2008, doi: 10.1088/0268-1242/23/7/072001.
[149] H. Tsujimura, S. Nakagawa, K. Okamoto, et H. Ohta, « Characteristics of Polarized Electroluminescence from *m* -plane InGaN-based Light Emitting Diodes », *Japanese Journal of Applied Physics*, vol. 46, nº No. 42, p. L1010-L1012, oct. 2007, doi: 10.1143/JJAP.46.L1010.
[150] S. Nakagawa, H. Tsujimura, K. Okamoto, M. Kubota, et H. Ohta, « Temperature dependence of polarized electroluminescence from nonpolar m-plane InGaN-based light emitting diodes », *Applied Physics Letters*, vol. 91, nº 17, p. 171110, oct. 2007, doi: 10.1063/1.2800817.
[151] H. Yamada *et al.*, « Effects of off-axis GaN substrates on optical properties of m-plane InGaN/GaN light-emitting diodes », *Journal of Crystal Growth*, vol. 310, nº 23, p. 4968-4971, nov. 2008, doi: 10.1016/j.jcrysgro.2008.06.079.
[152] E. Sarelli, J. C. Pillet, B. B. Bakir, et G. L. Blevennec, « Optical polarization of light emission from sidewalls of single quantum well near interface in spontaneous regime », *Semicond. Sci. Technol.*, vol. 36, nº 6, p. 065001, avr. 2021, doi: 10.1088/1361-6641/abeecc.
[153] W. L. Barnes, « Fluorescence near interfaces: The role of photonic mode density », *Journal of Modern Optics*, vol. 45, nº 4, p. 661-699, avr. 1998, doi: 10.1080/09500349808230614.
[154] A. I. Chizhik, J. Rother, I. Gregor, A. Janshoff, et J. Enderlein, « Metal-induced energy transfer for live cell nanoscopy », *Nature Photonics*, vol. 8, nº 2, p. 124-127, févr. 2014, doi: 10.1038/nphoton.2013.345.
[155] R. S. Swathi et K. L. Sebastian, « Long range resonance energy transfer from a dye molecule to graphene has (distance)−4 dependence », *The Journal of Chemical Physics*, vol. 130, nº 8, p. 086101, févr. 2009, doi: 10.1063/1.3077292.

[156] F. Prins, A. J. Goodman, et W. A. Tisdale, « Reduced Dielectric Screening and Enhanced Energy Transfer in Single- and Few-Layer MoS $_2$ », *Nano Letters*, vol. 14, n° 11, p. 6087-6091, nov. 2014, doi: 10.1021/nl5019386.
[157] A. Raja *et al.*, « Energy Transfer from Quantum Dots to Graphene and MoS $_2$: The Role of Absorption and Screening in Two-Dimensional Materials », *Nano Letters*, vol. 16, n° 4, p. 2328-2333, avr. 2016, doi: 10.1021/acs.nanolett.5b05012.
[158] M. Lunz, A. L. Bradley, W.-Y. Chen, et Y. K. Gun'ko, « Förster resonant energy transfer in quantum dot layers », *Superlattices and Microstructures*, vol. 47, n° 1, p. 98-102, janv. 2010, doi: 10.1016/j.spmi.2009.06.011.
[159] S. B. Brichkin, « Nonradiative resonance energy transfer in systems containing quantum dots and its application », *High Energy Chemistry*, vol. 47, n° 6, p. 277-285, nov. 2013, doi: 10.1134/S0018143913060027.
[160] C. R. Kagan, C. B. Murray, et M. G. Bawendi, « Long-range resonance transfer of electronic excitations in close-packed CdSe quantum-dot solids », *Physical Review B*, vol. 54, n° 12, p. 8633-8643, sept. 1996, doi: 10.1103/PhysRevB.54.8633.
[161] K. Cnops, B. P. Rand, D. Cheyns, B. Verreet, M. A. Empl, et P. Heremans, « 8.4% efficient fullerene-free organic solar cells exploiting long-range exciton energy transfer », *Nat Commun*, vol. 5, n° 1, p. 3406, mai 2014, doi: 10.1038/ncomms4406.
[162] S. Khatsevich et D. H. Rich, « The effects of crystallographic orientation and strain on the properties of excitonic emission from wurtzite InGaN/GaN quantum wells », *J. Phys.: Condens. Matter*, vol. 20, n° 21, p. 215223, avr. 2008, doi: 10.1088/0953-8984/20/21/215223.
[163] W. Chen *et al.*, « Free charges versus excitons: photoluminescence investigation of InGaN/GaN multiple quantum well nanorods and their planar counterparts », *Nanoscale*, vol. 10, n° 11, p. 5358-5365, 2018, doi: 10.1039/C7NR07567G.
[164] M. Achermann, M. A. Petruska, S. Kos, D. L. Smith, D. D. Koleske, et V. I. Klimov, « Energy-transfer pumping of semiconductor nanocrystals using an epitaxial quantum well », *Nature*, vol. 429, n° 6992, p. 642-646, juin 2004, doi: 10.1038/nature02571.
[165] S. Rohrmoser *et al.*, « Temperature dependence of exciton transfer in hybrid quantum well/nanocrystal heterostructures », *Applied Physics Letters*, vol. 91, n° 9, p. 092126, août 2007, doi: 10.1063/1.2776865.
[166] G. Heliotis, G. Itskos, R. Murray, M. D. Dawson, I. M. Watson, et D. D. C. Bradley, « Hybrid Inorganic/Organic Semiconductor Heterostructures with Efficient Non-Radiative Energy Transfer », *Adv. Mater.*, vol. 18, n° 3, p. 334-338, févr. 2006, doi: 10.1002/adma.200501949.
[167] S. Chanyawadee, P. G. Lagoudakis, R. T. Harley, D. G. Lidzey, et M. Henini, « Nonradiative exciton energy transfer in hybrid organic-inorganic heterostructures », *Physical Review B*, vol. 77, n° 19, mai 2008, doi: 10.1103/PhysRevB.77.193402.
[168] E. Jang, S. Jun, H. Jang, J. Lim, B. Kim, et Y. Kim, « White-Light-Emitting Diodes with Quantum Dot Color Converters for Display Backlights », *Adv. Mater.*, vol. 22, n° 28, p. 3076-3080, mai 2010, doi: 10.1002/adma.201000525.
[169] R. Smith, B. Liu, J. Bai, et T. Wang, « Hybrid III-Nitride/Organic Semiconductor Nanostructure with High Efficiency Nonradiative Energy Transfer for White Light Emitters », *Nano Lett.*, vol. 13, n° 7, p. 3042-3047, juill. 2013, doi: 10.1021/nl400597d.
[170] J. J. Rindermann, G. Pozina, B. Monemar, L. Hultman, H. Amano, et P. G. Lagoudakis, « Dependence of Resonance Energy Transfer on Exciton Dimensionality », *Physical Review Letters*, vol. 107, n° 23, nov. 2011, doi: 10.1103/PhysRevLett.107.236805.
[171] G. Itskos *et al.*, « Efficient dipole-dipole coupling of Mott-Wannier and Frenkel excitons in (Ga,In)N quantum well/polyfluorene semiconductor heterostructures », *Physical Review B*, vol. 76, n° 3, juill. 2007, doi: 10.1103/PhysRevB.76.035344.

[172] G. Itskos, A. Othonos, S. A. Choulis, et E. Iliopoulos, « Förster resonant energy transfer from an inorganic quantum well to a molecular material: Unexplored aspects, losses, and implications to applications », *J. Chem. Phys.*, vol. 143, nº 21, p. 214701, déc. 2015, doi: 10.1063/1.4935963.
[173] š. Kos, M. Achermann, V. I. Klimov, et D. L. Smith, « Different regimes of Förster-type energy transfer between an epitaxial quantum well and a proximal monolayer of semiconductor nanocrystals », *Physical Review B*, vol. 71, nº 20, mai 2005, doi: 10.1103/PhysRevB.71.205309.
[174] S. Ghataora, R. M. Smith, M. Athanasiou, et T. Wang, « Electrically Injected Hybrid Organic/Inorganic III-Nitride White Light-Emitting Diodes with Nonradiative Förster Resonance Energy Transfer », *ACS Photonics*, vol. 5, nº 2, p. 642-647, févr. 2018, doi: 10.1021/acsphotonics.7b01291.
[175] G. Heliotis, G. Itskos, R. Murray, M. D. Dawson, I. M. Watson, et D. D. C. Bradley, « Hybrid Inorganic/Organic Semiconductor Heterostructures with Efficient Non-Radiative Energy Transfer », *Advanced Materials*, vol. 18, nº 3, p. 334-338, févr. 2006, doi: 10.1002/adma.200501949.
[176] B. Kolaric, K. Baert, M. Van der Auweraer, R. A. L. Vallée, et K. Clays, « Controlling the Fluorescence Resonant Energy Transfer by Photonic Crystal Band Gap Engineering », *Chem. Mater.*, vol. 19, nº 23, p. 5547-5552, nov. 2007, doi: 10.1021/cm0713935.
[177] C. R. Kagan, C. B. Murray, et M. G. Bawendi, « Long-range resonance transfer of electronic excitations in close-packed CdSe quantum-dot solids », *Phys. Rev. B*, vol. 54, nº 12, p. 8633-8643, sept. 1996, doi: 10.1103/PhysRevB.54.8633.
[178] C. Curutchet, J. Kongsted, A. Muñoz-Losa, H. Hossein-Nejad, G. D. Scholes, et B. Mennucci, « Photosynthetic Light-Harvesting Is Tuned by the Heterogeneous Polarizable Environment of the Protein », *J. Am. Chem. Soc.*, vol. 133, nº 9, p. 3078-3084, mars 2011, doi: 10.1021/ja110053y.
[179] C. R. Kagan, C. B. Murray, M. Nirmal, et M. G. Bawendi, « Electronic Energy Transfer in CdSe Quantum Dot Solids », *PHYSICAL REVIEW LETTERS*, vol. 76, nº 9, p. 4, 1996.
[180] D. a. G. Bruggeman, « Berechnung verschiedener physikalischer Konstanten von heterogenen Substanzen. I. Dielektrizitätskonstanten und Leitfähigkeiten der Mischkörper aus isotropen Substanzen », *Annalen der Physik*, vol. 416, nº 7, p. 636-664, 1935, doi: https://doi.org/10.1002/andp.19354160705.
[181] V. N. Astratov *et al.*, « Photonic band-structure effects in the reflectivity of periodically patterned waveguides », *Phys. Rev. B*, vol. 60, nº 24, p. R16255-R16258, déc. 1999, doi: 10.1103/PhysRevB.60.R16255.
[182] F. Raineri *et al.*, « Nonlinear optical manipulation of Fano resonances in 2D photonic crystal slabs », in *Postconference Digest Quantum Electronics and Laser Science, 2003. QELS.*, juin 2003, p. 1 pp.-. doi: 10.1109/QELS.2003.238390.
[183] J. Yu, M. Sharma, A. Sharma, S. Delikanli, H. Volkan Demir, et C. Dang, « All-optical control of exciton flow in a colloidal quantum well complex », *Light Sci Appl*, vol. 9, nº 1, p. 27, déc. 2020, doi: 10.1038/s41377-020-0262-7.
[184] M. Ibanescu, « Cylindrical photonic crystals », Thesis, Massachusetts Institute of Technology, 2005. Consulté le: 11 juin 2018. [En ligne]. Disponible sur: http://dspace.mit.edu/handle/1721.1/32306
[185] M. Davanço, M. T. Rakher, D. Schuh, A. Badolato, et K. Srinivasan, « A circular dielectric grating for vertical extraction of single quantum dot emission », *Appl. Phys. Lett.*, vol. 99, nº 4, p. 041102, juill. 2011, doi: 10.1063/1.3615051.

[186] J. Scheuer, W. M. J. Green, G. A. DeRose, et A. Yariv, « Lasing from a circular Bragg nanocavity with an ultrasmall modal volume », *Appl. Phys. Lett.*, vol. 86, nº 25, p. 251101, juin 2005, doi: 10.1063/1.1947375.
[187] M. Ibanescu, « An All-Dielectric Coaxial Waveguide », *Science*, vol. 289, nº 5478, p. 415-419, juill. 2000, doi: 10.1126/science.289.5478.415.
[188] L. Penninck, F. Steinbacher, R. Krause, et K. Neyts, « Determining emissive dipole orientation in organic light emitting devices by decay time measurement », *Organic Electronics*, vol. 13, nº 12, p. 3079-3084, déc. 2012, doi: 10.1016/j.orgel.2012.09.014.
[189] H. Masui *et al.*, « Polarized Light Emission from Nonpolar InGaN Light-Emitting Diodes Grown on a Bulk *m* -Plane GaN Substrate », *Jpn. J. Appl. Phys.*, vol. 44, nº No. 43, p. L1329-L1332, oct. 2005, doi: 10.1143/JJAP.44.L1329.

Appendix

FIG. A.1

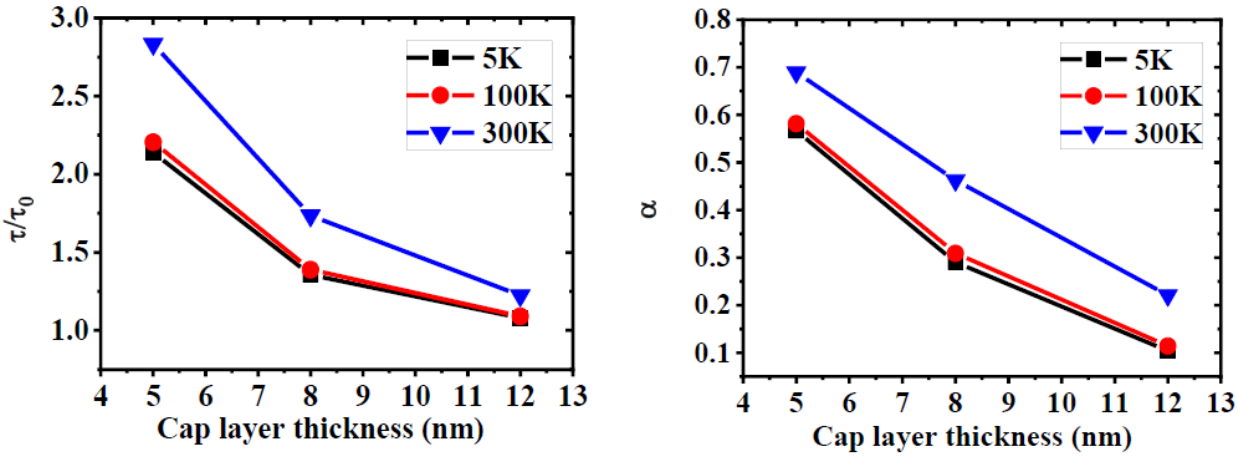

The comparison of the room with the low temperature measurements that show similar tendency but the values are lower.

FIG. A.2

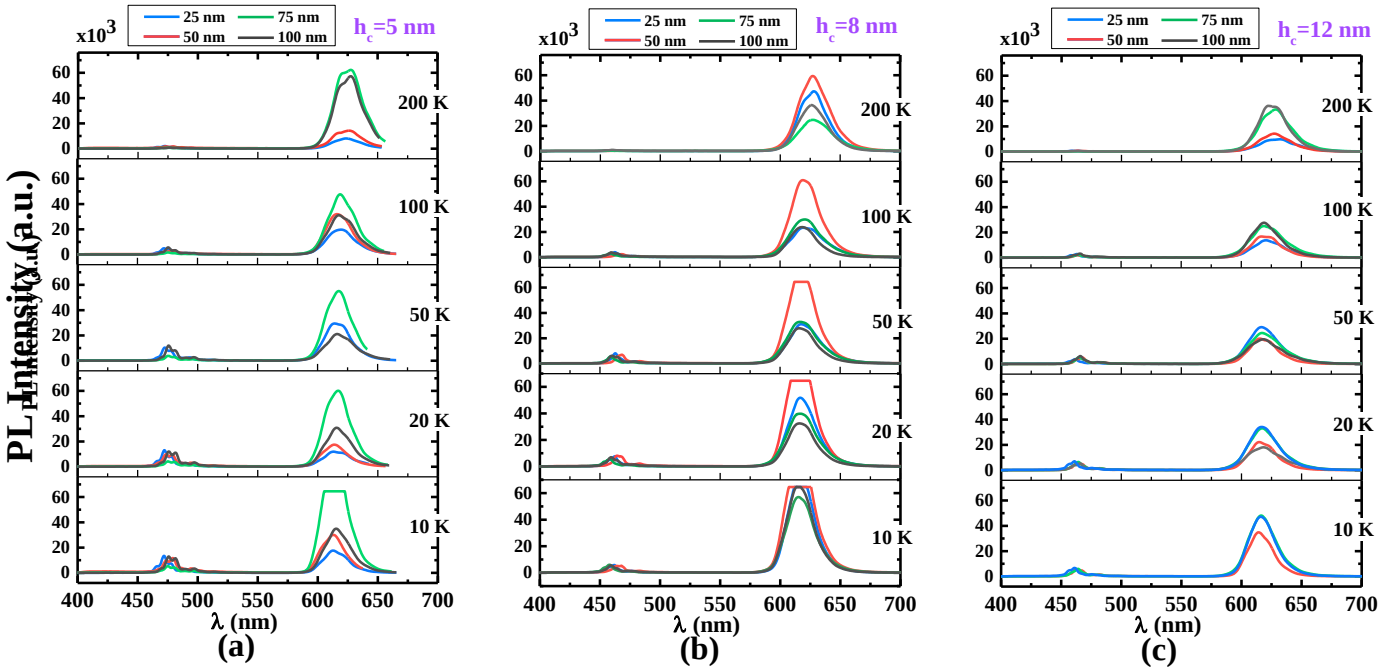

The PL measurements at excitation power of 5.5 μW.

Table. A.1

h_c=5nm						
T (K)	**τ_{QW} (ns)**	**$\delta\tau_{QW}$**	**τ_{NRET} (ns)**	**$\delta\tau_{NRET}$**	**τ_{rad} (ns)**	**$\delta\tau_{rad}$**
5	41.28295	0.07147	5.28039	0.22652	40.93998	0.15283
50	36.74735	0.06273	7.16351	0.18353	36.66726	0.19978
100	22.78048	0.03378	5.1584	0.11805	20.90254	0.13949
300	10.27106	0.03613	2.33227	0.28129	7.19467	0.13197

h_c=8nm						
T (K)	**τ_{QW} (ns)**	**$\delta\tau_{QW}$**	**τ_{NRET} (ns)**	**$\delta\tau_{NRET}$**	**τ_{rad} (ns)**	**$\delta\tau_{rad}$**
5	16.98305	0.01413	9.41116	0.40382	30.71313	1.01563
50	19.99683	0.02244	12.23068	0.26977	27.78595	0.53448
100	16.10935	0.02259	5.08995	0.27728	20.56281	0.08674
300	7.56655	0.02485	2.47626	0.16376	9.42806	0.07668

h_c=12nm						
T (K)	**τ_{QW} (ns)**	**$\delta\tau_{QW}$**	**τ_{NRET} (ns)**	**$\delta\tau_{NRET}$**	**τ_{rad} (ns)**	**$\delta\tau_{rad}$**
5	16.58973	0.02616	9.41116	0.40382	30.71313	1.01563
50	15.14061	0.01844	7.88028	0.08443	20.97749	0.13668
100	14.00111	0.02239	4.8869	0.07506	17.25992	0.05825
300	9.489	0.04724	3.08576	0.08397	10.28515	0.1028

TABLE. A.1. The values of the short-range coupling lifetimes.

Table. A.2

h_c=5nm, 10K

QW-QW (nm)	τ_{NRET} (ns)	$\delta\tau_{NRET}$	τ_{rad} (ns)	$\delta\tau_{rad}$
30	13.05535	0.7016	49.29597	0.37403
55	3.70314	0.06148	46.45509	0.19324
80	3.73741	0.12075	50.09453	0.34828
105	10.25504	0.62555	51.24117	0.30346

h_c=5nm, 20K

QW-QW (nm)	τ_{NRET} (ns)	$\delta\tau_{NRET}$	τ_{rad} (ns)	$\delta\tau_{rad}$
30	8.66949	0.54378	49.55876	0.25582
55	3.67813	0.0716	46.83986	0.16953
80	2.79015	0.07301	52.20485	0.42916
105	8.88553	0.73258	52.58491	0.27741

h_c=5nm, 50K

QW-QW (nm)	τ_{NRET} (ns)	$\delta\tau_{NRET}$	τ_{rad} (ns)	$\delta\tau_{rad}$
30	7.93566	0.27048	43.17328	0.28562
55	3.36757	0.06219	40.13131	0.2041
80	3.81341	0.12317	46.74542	0.41954
105	10.54529	0.3226	45.55472	0.26859

h_c=5nm, 100K

QW-QW (nm)	τ_{NRET} (ns)	$\delta\tau_{NRET}$	τ_{rad} (ns)	$\delta\tau_{rad}$
30	5.17288	0.27011	28.6794	0.28987
55	3.34017	0.07642	30.69655	0.16974
80	3.04126	0.09045	33.55119	0.24427
105	5.15652	0.15867	34.64417	0.13811

h_c=5nm, 200K

QW-QW (nm)	τ_{NRET} (ns)	$\delta\tau_{NRET}$	τ_{rad} (ns)	$\delta\tau_{rad}$
30	2.0664	0.20717	13.07613	0.14108
55	1.86618	0.06748	14.95998	0.1
80	1.54504	0.08255	11.44002	0.17252
105	1.8971	0.11753	13.36708	0.13114

h_c=5nm, 300K

QW-QW (nm)	τ_{NRET} (ns)	$\delta\tau_{NRET}$	τ_{rad} (ns)	$\delta\tau_{rad}$
30	1.55658	0.11472	9.35302	0.21837
55	1.04783	0.01206	9.60681	0.09316
80	2.23667	0.17122	13.39	0.09722
105	0.78244	0.03491	9.62343	0.13658

h_c=8nm, 10K

QW-QW (nm)	τ_{NRET} (ns)	$\delta\tau_{NRET}$	τ_{rad} (ns)	$\delta\tau_{rad}$
33	7.71298	0.30081	29.78935	0.31556
58	3.89805	0.08886	31.70474	0.1676
83	6.53042	0.21412	26.25117	0.26158
108	8.20327	0.19556	27.97785	0.22933

h_c=8nm, 20K

QW-QW (nm)	τ_{NRET} (ns)	$\delta\tau_{NRET}$	τ_{rad} (ns)	$\delta\tau_{rad}$
33	8.62417	0.27206	32.75308	0.33443
58	5.71071	0.16555	30.10529	0.16438
83	4.21165	0.12421	33.27288	0.31381
108	5.83676	0.13278	29.20165	0.18597

h_c=8nm, 50K

QW-QW (nm)	τ_{NRET} (ns)	$\delta\tau_{NRET}$	τ_{rad} (ns)	$\delta\tau_{rad}$
33	8.01927	0.29217	30.67812	0.25426
58	6.33988	0.15748	30.79181	0.1768
83	3.49362	0.11729	33.16704	0.26409
108	3.85085	0.06668	27.30788	0.12911

h_c=8nm, 100K

QW-QW (nm)	τ_{NRET} (ns)	$\delta\tau_{NRET}$	τ_{rad} (ns)	$\delta\tau_{rad}$
33	3.76026	0.17392	22.43269	0.12706
58	3.12844	0.10524	22.65613	0.1544
83	2.47594	0.08337	17.26393	0.29806
108	2.56785	0.04867	19.74898	0.08305

h_c=8nm, 200K

QW-QW (nm)	τ_{NRET} (ns)	$\delta\tau_{NRET}$	τ_{rad} (ns)	$\delta\tau_{rad}$
33	1.83902	0.20795	11.51127	0.14498
58	1.36499	0.08694	7.88728	0.25261
83	1.57652	0.09977	8.2798	0.18118
108	1.44913	0.0629	10.60566	0.08559

h_c=8nm, 300K

QW-QW (nm)	τ_{NRET} (ns)	$\delta\tau_{NRET}$	τ_{rad} (ns)	$\delta\tau_{rad}$
33	2.68935	0.05802	10.70433	0.08261
58	0.82284	0.02673	5.82969	0.14607
83	0.95411	0.02197	7.67297	0.10185
108	5	0.01087	8.59844	0.10374

h_c=12nm, 10K

QW-QW (nm)	τ_{NRET} (ns)	$\delta\tau_{NRET}$	τ_{rad} (ns)	$\delta\tau_{rad}$
37	4.18151	0.09592	25.55534	0.12737
62	9.98356	0.56831	33.42731	0.54383
87	9.07205	0.36981	32.18836	0.33132
112	8.30481	0.5216	32.23027	0.32484

h_c=12nm, 20K

QW-QW (nm)	τ_{NRET} (ns)	$\delta\tau_{NRET}$	τ_{rad} (ns)	$\delta\tau_{rad}$
37	3.45027	0.06801	25.0597	0.11179
62	10.42881	0.40582	36.26007	0.50405
87	10.77671	0.41776	33.98766	0.49825
112	9.93051	0.73788	33.19204	0.46905

h_c=12nm, 50K

QW-QW (nm)	τ_{NRET} (ns)	$\delta\tau_{NRET}$	τ_{rad} (ns)	$\delta\tau_{rad}$
37	3.59692	0.0645	21.31351	0.21525
62	7.57841	0.41208	32.70697	0.36841
87	7.25028	0.24068	30.35457	0.28812
112	7.28478	0.40052	29.98417	0.34901

h_c=12nm, 100K

QW-QW (nm)	τ_{NRET} (ns)	$\delta\tau_{NRET}$	τ_{rad} (ns)	$\delta\tau_{rad}$
37	9.01084	1.43179	22.95827	0.90327
62	2.75916	0.13002	20.9957	0.14958
87	4.13525	0.20214	17.96153	0.2922
112	5.78946	0.37614	20.85443	0.36214

h_c=12nm, 200K

QW-QW (nm)	τ_{NRET} (ns)	$\delta\tau_{NRET}$	τ_{rad} (ns)	$\delta\tau_{rad}$
37	1.16695	0.25184	9.78395	0.08837
62	1.34317	0.2987	10.02968	0.12945
87	0.83113	0.10562	4.72336	0.12737
112	1.58511	0.41863	7.22243	0.2015

h_c=12nm, 300K

QW-QW (nm)	τ_{NRET} (ns)	$\delta\tau_{NRET}$	τ_{rad} (ns)	$\delta\tau_{rad}$
37	1.06467	0.11815	6.41725	0.16874
62	0.85968	0.02709	7.96482	0.12198
87	0.76225	0.09081	3.92873	0.14634
112	0.67313	0.05529	4.51085	0.12266

TABLE. A.2. The values of the long-range coupling lifetimes.

Résumé en français

L'industrie des micro-LED (diodes électroluminescentes) ciblant une variété d'applications allant des produits portables tels que les casques de réalité augmentée (AR), virtuelle (VR) et mixte (MR) et les montres intelligentes, aux affichages et projecteurs automobiles tête haute (HUD) et tête montée (HMD), aux panneaux d'affichage extérieurs, etc. a déjà gagné une part importante du marché de la microélectronique. En ce qui concerne les applications de micro-affichage, les micro-LED à base de GaN sont actuellement au centre de l'attention car elles peuvent répondre à la demande d'une représentation de haute qualité avec un pas de pixel inférieur à 10 µm x 10 µm. Parallèlement, la technologie de synthèse des nanocristaux colloïdaux de semi-conducteurs arrive à maturité. Par conséquent, la conception de nanocristaux LED GaN est devenue un candidat prometteur, car elle permet un éclairage multicolore efficace grâce à la conversion des couleurs. Les puits quantiques InGaN/GaN combinés à des points quantiques (QD) constituent l'une des stratégies de base pour la réalisation d'un micro-affichage RVB.

Dans une telle configuration, il est essentiel de créer les conditions d'un couplage lumineux optimal entre le QW et les QDs. En tenant compte de l'épaisseur nanométrique du bleu des QWs émettant dans l'ultraviolet, leur couplage avec les QDs peut utiliser plus d'un canal, y compris le transfert d'énergie non radiatif (NRET). Ce dernier est une interaction dipôle-dipôle sans émission qui a lieu dans des conditions spécifiques. Cette interaction a fait l'objet d'un grand nombre d'articles, étudiant sa dépendance à la distance donneur-accepteur, à leur orientation dipolaire mutuelle et à l'environnement photonique du donneur sous la forme de la densité locale d'états (LDOS).

L'objectif principal de cette thèse de doctorat est de réaliser une étude approfondie des conditions qui affectent le NRET dans le contexte de l'interaction InGaN/GaN-QDs comme moyen d'améliorer l'efficacité de la conversion des couleurs pour les applications micro-LEDs RGB. Notre motivation est basée sur le fait que, malgré les connaissances récemment accumulées sur le sujet, la quantification des paramètres de base qui affectent le transfert d'énergie à travers une interface hétérogène reste peu explorée. Face à une situation non-classique, dans le sens d'une manière alternative de coupler la lumière, son étude est importante à la fois en termes de science fondamentale et afin d'optimiser l'efficacité des schémas d'excitation basés sur la NRET dans les dispositifs appliqués. Le travail de thèse se concentre

sur l'étude théorique et expérimentale des trois paramètres principaux qui affectent le taux de NRET: l'orientation dipolaire du donneur, l'espacement donneur-accepteur et le LDOS.

Dans le cas des LED pour les applications de micro-affichage, deux des principaux objectifs de la recherche en optoélectronique et en photonique sont l'amélioration du taux d'émission et le contrôle précis du front d'onde de la lumière émise. Le contrôle de la polarisation est un paramètre de première importance pour l'amélioration de l'efficacité des LED et, dans notre cas, nous pouvons y parvenir en tirant parti des propriétés de couplage NRET. Le transfert d'énergie non radiatif dans une configuration puits quantique (QW) InGaN/GaN - points quantiques (QDs) est une interaction dipôle-dipôle. Dans la théorie NRET, le QW et les QDs peuvent être décrits comme des dipôles donneurs et accepteurs respectivement. Bien que les QDs soient intrinsèquement non polarisés, leur polarisation est induite par le champ électrique du donneur[114]. Cela signifie que le QW est responsable des combinaisons de polarisation possibles entre le donneur et l'accepteur qui peuvent améliorer ou inhiber le couplage et donc le taux d'émission. Une orientation dipolaire uniforme dans le QW peut être la source d'une émission polarisée à partir des QDs et il est donc crucial de connaître et de contrôler l'orientation du dipôle dans le QW.

Dans le deuxième chapitre de cette thèse, nous étudions l'impact de la localisation d'un QW unique InGaN/GaN d'abord sur son orientation dipolaire et ensuite sur son émission polarisée. L'épaisseur de la couche supérieure de GaN (ou couche de recouvrement) a été choisie pour être de 5, 8 et 12 nm. Ce choix est basé sur la théorie du transfert d'énergie non radiatif, qui calcule que la distance optimale entre les dipôles du donneur et de l'accepteur est de 10 nm pour un taux d'émission NRET maximisé (au moins pour les milieux homogènes). Cela signifie que dans notre cas, le QW doit être localisé près de l'interface GaN/air.

Dans un premier temps, nous examinons l'orientation des dipôles dans le QW. Sur la base du calcul mathématique du taux de décroissance spontanée qui est dérivé des équations de Maxwell, en utilisant les calculs de Novotny[114],[115] et Hecht[116], nous pouvons décrire le rayonnement d'un dipôle orienté arbitrairement près d'une interface plane (ici une interface GaN/air).

Dans un deuxième temps, nous avons mesuré le temps de décroissance après excitation optique avec un laser pulsé. Les mesures de durée de vie ont été effectuées à l'aide d'une tête de diode laser picoseconde (série LDH, Picoquant). La longueur d'onde d'excitation était de 375 nm, la durée de l'impulsion était de 50 ps avec un taux de répétition de 5 MHz pour le fonctionnement pulsé. Les mesures ont été effectuées sur les trois échantillons (au même endroit sur chaque échantillon) à 295 K et à différentes valeurs de puissance d'excitation

optique. Ensuite, les données de photoluminescence résolues dans le temps ont été ajustées comme une décroissance mono-exponentielle à l'aide de la formule suivante: $I(t) = I_0 + e^{-t/\tau}$ où I correspond au nombre de photons, I_0 est une constante et τ la valeur de la durée de vie. Afin de comparer avec les simulations, l'étape suivante est l'extraction de la durée de vie spontanée, qui est essentiellement la valeur de la durée de vie à une puissance d'excitation nulle.

Afin de quantifier l'orientation dipolaire, nous avons utilisé la méthode de Penninck et al pour déterminer le degré d'orientation des émetteurs en mesurant le signal de décroissance luminescente[147]. Elle est basée sur la dépendance du taux de décroissance des excitons à l'environnement optique et à l'orientation du moment de transition du dipôle. En résumé, le taux de décroissance total Γ_{tot} des dipôles est la somme des taux de décroissance radiative et non radiative. Le taux de décroissance radiative est donné par la règle d'or de Fermi, qui dépend des opérateurs du moment dipolaire de transition et du champ électrique. Si nous décrivons la puissance émise par des antennes dipôles de différentes orientations dans une microcavité comme des ondes planes, il est possible d'extraire le pourcentage des dipôles qui sont alignés verticalement par rapport au substrat. La constante (Eq.II. 6) exprime le pourcentage de dipôles verticaux dans le QW en tenant compte des durées de vie extraites expérimentalement. Tous nos résultats, le calcul théorique, les points expérimentaux et le coefficient extrait sont résumés dans la FIG. II.5.

Il apparaît qu'il existe une orientation préférentielle des dipôles en fonction de la séparation entre le QW et l'interface et que ce phénomène d'orientation est inversement proportionnel à la distance du QW par rapport à l'interface. Ainsi, lorsque cette dernière est de 5 nm, la majorité des dipôles, avec un pourcentage de 69% à température ambiante, sont alignés verticalement par rapport au substrat. Ce pourcentage semble diminuer fortement avec l'augmentation de la profondeur du QW. A titre de comparaison, pour la couche de couverture de 12 nm, cette valeur tombe à 22%. D'après nos calculs, une couche de recouvrement supérieure à 7.5 nm implique que la majorité des dipôles dans le QW sont alignés horizontalement. En conclusion, dans la structure de la couche de recouvrement de 5 nm, la majorité des dipôles sont perpendiculaires au substrat, ce qui correspond à des durées de vie plus longues par rapport au cas de la couche de recouvrement de 12 nm ou même de 8 nm, où la majorité des dipôles sont alignés parallèlement avec des durées de vie beaucoup plus courtes. Les points expérimentaux de la FIG. II.5 montrent une tendance qui, au moins qualitativement, est décrite à la fois par des polarisations perpendiculaires et parallèles. Par conséquent, l'épaisseur de la couche de recouvrement peut altérer l'environnement photonique des dipôles dans le QW et modifier leur orientation. Cela signifie que l'augmentation de la durée de vie spontanée normalisée peut être

affectée par le nombre plus élevé de dipôles verticaux (par rapport aux dipôles horizontaux) dans le QW lorsque la couche de recouvrement est suffisamment fine. En résumé, nous avons montré qu'en utilisant un modèle simple basé sur des mesures de photoluminescence résolues dans le temps, nous pouvons estimer le pourcentage de dipôles ayant une orientation verticale par rapport au substrat pour les trois épaisseurs de couche de recouvrement, dans le régime d'émission spontanée.

Comme il n'est pas possible de mesurer directement l'orientation du dipôle dans le QW, l'observation de la polarisation de l'émission de la zone active peut donner un aperçu supplémentaire de cette question. En d'autres termes, l'objectif de la deuxième partie du premier chapitre était la caractérisation expérimentale de la lumière polarisée émise par un QW situé près de la surface supérieure d'une LED GaN. Dans notre travail récemment publié[152], nous avons étudié l'émission de lumière à partir des parois latérales de nos trois échantillons avec une couche de couverture GaN de 5, 8 et 12 nm en termes de polarisation.

En utilisant un polariseur rotatif et à l'aide d'un microscope confocal, nous sommes capables de mesurer l'émission perpendiculaire et dans le plan - par rapport au substrat - des QW et d'évaluer le rapport de polarisation dans le régime d'émission spontanée pour les trois épaisseurs de couche de recouvrement. En utilisant l'approche de Masui et al[148], nous avons obtenu des spectres complets pour chacun des quatre échantillons et la dépendance à l'orientation du polariseur pour une variété de puissances d'excitation. Nos résultats exprimés en rapports de polarisation montrent qu'à proximité de l'interface diélectrique, les rapports de polarisation sont inférieurs à 0.1 pour des excitations de faible puissance, ce qui signifie une polarisation quasi-isotrope des émetteurs. De plus, il semble que la proximité de la surface supérieure de la LED avec le SQW à quelques nanomètres affecte les rapports de polarisation de manière fondamentale. Pour renforcer cette conclusion, nous avons comparé cette structure à une structure standard (de référence) à plusieurs QW InGaN/GaN, où les QW sont enfouis à une profondeur de 300 nm sous l'interface supérieure. La mesure et l'extrapolation des données expérimentales à une puissance d'excitation nulle ont révélé le comportement très différent des structures SQW et MQW[152]. La mesure de l'échantillon de référence ramène la valeur obtenue par Masui pour le rapport de polarisation à environ 90%, ce qui suggère que l'émission polarisée est dans le plan du QW. De plus, cette valeur ne change pas lorsque l'énergie d'excitation diminue. D'autre part, les rapports de polarisation correspondant aux trois échantillons de SQW passent d'environ 0.25 à 0.05 lorsque la puissance d'excitation diminue et sont inversement proportionnels à la valeur de la barrière quantique dans le régime spontané. Cela suggère que la polarisation pourrait être majoritairement perpendiculaire.

Tant l'approche théorique que les mesures effectuées soulignent le fort impact de la proximité de l'interface nanométrique sur le rapport de polarisation et, par conséquent, sur l'orientation des dipôles émetteurs dans un SQW InGaN/GaN. L'épaisseur de la couche de recouvrement crée les conditions qui définissent la direction de la polarisation et forme un lien entre la durée de vie spontanée normalisée et l'alignement des dipôles dans le QW. Nos résultats suggèrent donc que la polarisation perpendiculaire des porteurs dans le QW peut être corrélée à l'orientation des dipôles de l'émetteur. Nous avons également démontré que ce phénomène d'orientation est inversement proportionnel à la distance du QW par rapport à l'interface. Ce résultat suggère que la position du QW près de l'interface peut fortement affecter le mécanisme de transfert d'énergie car elle modifie l'orientation du donneur - le rôle du QW InGaN dans le couplage en champ proche. Sachant que la polarisation du donneur induit le même type de polarisation au niveau de l'accepteur, nous avons deux cas de figure: les dipôles QW-QD sont soit parallèles, soit colinéaires l'un à l'autre, ce qui, selon la théorie NRET, peut influer sur leur distance de couplage. C'est un facteur qui doit être pris en compte lorsque le QW est placé près de la surface supérieure de la LED de conversion de couleur pour améliorer le transfert d'énergie non radiatif, car la configuration donneur-accepteur modifie profondément la polarisation de l'émission de lumière. Cela permet de conclure que la polarisation est un paramètre physique d'une grande importance qui devrait être pris en compte lors de la conception des dispositifs pouvant produire des micro-LED RGB à base d'InGaN à haute performance. Par extension, cet effet peut être considéré dans le cas de QWs interagissant avec tout autre support actif placé sur la surface supérieure et à proximité.

L'objectif du troisième chapitre est l'étude de l'interaction entre un QW InGaN/GaN unique et des points quantiques rouges colloïdaux dans le champ proche pour des applications de conversion de couleur. L'objectif final sera d'estimer la performance d'une LED à base de GaN, fabriquée pour fonctionner dans le champ proche, qui utilise des QDs comme couche de conversion de couleur.

Basé sur la théorie FRET (ou NRET) pour les milieux isotropes, nous essayons dans ce travail de déchiffrer la nature de ce type d'interaction en étudiant les limites du couplage en champ proche dans une configuration non-isotrope. Pour cette raison, le paramètre principal que nous considérons ici est la distance physique entre le donneur et l'accepteur. Tout d'abord, théoriquement, le taux de transfert d'énergie non radiatif décroît rapidement ($\sim R^6$) avec la distance donneur-accepteur. De plus, les calculs théoriques indiquent que la distance dite de Förster (R_0)de la paire donneur-accepteur, c'est-à-dire la distance à laquelle l'efficacité du transfert d'énergie est de 50 %, est de 10 nm pour les milieux homogènes. Pour cette raison,

nous avons initialement choisi une séparation QW-QD de 5, 8 et 12 nm en termes d'épaisseur de la couche de couverture GaN. Néanmoins, comme les milieux concernés sont inhomogènes et non isotropes, après la première série d'expériences, un espaceur SiO_2 (25, 50, 75 et 100 nm) a été déposé au-dessus de la couche de couverture GaN afin d'augmenter la distance entre le QW et les QDs. Par conséquent, parallèlement à la recherche de la distance optimale qui maximisera l'efficacité NRET, nous étudions simultanément la performance du transfert d'énergie dans le couplage à longue distance. L'efficacité NRET est calculée à partir de données expérimentales basées sur la puissance d'excitation de la photoluminescence et les mesures de décroissance temporelle.

Des études résolues en temps dans des hétérostructures de puits quantiques hybrides ont démontré l'effet d'un canal de décroissance supplémentaire dans l'émission du puits quantique (donneur) [164], [165], [166]. Cependant, comme il est souligné dans la référence [167], cela ne peut pas être considéré comme une preuve de transfert d'énergie vers les sites accepteurs car le dépôt d'une couche de recouvrement (dans notre cas, les QDs dans une couche de polymère), séparant les sites donneurs et accepteurs, pourrait conduire à une modification de ses états de surface, ce qui modifierait la dynamique de décroissance. Tout changement dans la décroissance de la photoluminescence d'un puits quantique dans une structure hybride ne peut être attribué de manière concluante au transfert d'énergie non radiatif vers le site accepteur que si l'effet du transfert d'énergie est également observé directement dans les propriétés d'émission de l'accepteur. Ainsi, l'évaluation d'une NRET efficace est réalisée en surveillant l'interaction entre l'intensité d'émission du donneur et de l'accepteur ou, plus précisément, l'intensité élevée de l'accepteur avec la diminution simultanée de l'émission du donneur. C'est l'interaction entre le résultat PL et les résultats de l'efficacité du couplage qui indique l'existence ou non du couplage NRET à longue distance.

Les mesures optiques ont été réalisées afin d'étudier le couplage QW-QD en considérant les deux cas de couplage de champ proche à courte distance (jusqu'à 12 nm) et de couplage à longue distance (jusqu'à 112 nm). Les spectres de tous nos échantillons présentent l'émission de lumière bleue du QW InGaN et l'émission rouge des QDs CdSe. Au total, les propriétés optiques de 15 échantillons ont été étudiées pour des températures variant entre 10 et 300 K à une puissance d'excitation de 13,5 µW. Les mesures PL et TRPL ont été effectuées au même endroit pour chaque échantillon, à partir de la partie supérieure de l'échantillon. Dans ce cas, le laser n'est pas totalement absorbé par le QW, de sorte que seule une partie de l'excitation conduit à la PL des QDs.

Le signal est plus clair pour l'échantillon avec h_c=5 nm. En examinant la FIG. III.4.(a), nous pouvons voir que le signal d'intensité de l'émission rouge (longueur d'onde de 630 nm) lorsque l'épaisseur de l'espaceur SiO_2 est h_s=75 nm obtient sa valeur la plus élevée à toutes les températures. C'est la diminution de l'intensité du QW et l'augmentation simultanée de l'émission du QD qui signifient que le NRET a lieu et qu'il est plus productif avec l'espaceur de 75 nm que dans les autres cas. Pour la couche de recouvrement de 5 nm, ce phénomène se produit à toutes les températures. Une comparaison claire entre les différents espaceurs peut être trouvée dans la FIG.III.4 (d). Dans le cas de la couche de recouvrement de 8 nm, le signal d'intensité PL à 630 nm est toujours plus élevé pour l'espaceur de 50 nm. Néanmoins, le signal QW est très faible et nous ne pouvons donc pas observer clairement l'augmentation/diminution simultanée du QD/QW dans l'intensité PL à 20 K (FIG. III.4.(e) comme dans le cas de l'espaceur de 5 nm. De même, l'intensité PL de la couche chapeau de 12 nm (FIG. III.4.(f) semble plus élevée lorsque l'espaceur est de 25 nm (principalement à 10-50 K). Mais encore une fois, il est difficile d'évaluer la situation car l'émission dans le bleu devient très faible. Bien que nous ne puissions pas commenter chaque cas séparément, il y a une forte indication de NRET. Des résultats similaires ont été obtenus dans les autres cas où la puissance d'excitation est comprise entre 5.5 et 55 µW.

Nous réalisons ensuite des expériences de PL résolue dans le temps (TRPL) dans le bleu (longueur d'onde d'émission du QW~460 nm). Comme nous l'avons vu dans le chapitre précédent, l'ajustement des courbes TRPL du QW InGaN seul est mono-exponentiel. Or, lorsque la couche de QD est ajoutée, la décroissance dans le bleu est plus rapide et la courbe peut être ajustée avec une double exponentielle. Par conséquent, les deux durées de vie correspondant au couplage radiatif et aux processus non radiatifs[170] peuvent être facilement extraites. À partir des temps de vie, nous pouvons alors extraire l'efficacité de la NRET. En ce qui concerne la couche de recouvrement de 5 nm, l'efficacité obtient sa valeur la plus élevée à 10-200 K pour une distance totale QW-QD de 80 nm. Ceci est parfaitement en accord avec les résultats de la mesure PL. Cela signifie que dans ce cas, cet échantillon présente une augmentation de l'émission du QD avec une diminution simultanée de l'émission du QW uniquement lorsque h_s=75 nm. L'émission bleue PL pour les 8 et 12 nm est faible et il est donc plus difficile de décrire un lien entre la PL et l'efficacité NRET. On a supposé que la couche intercalaire de SiO_2 formait une interface sans trempe. Dans une étude similaire[161] portant sur des applications photovoltaïques et utilisant des matériaux très différents des nôtres, ils ont observé des résultats similaires avec l'utilisation d'un espaceur, le signal PL étant toujours

efficacement éteint par le donneur pour des couches d'espaceur allant jusqu'à 35 nm (c'est-à-dire l'espaceur le plus épais utilisé dans leur étude).

En considérant à la fois les mesures PL et TRPL, on obtient une indication claire du couplage NRET. Dans ce sens, la diminution de la distance donneur-accepteur, ainsi que le fait d'une énergie de liaison élevée dans le QW qui maintient les porteurs bien confinés, il est raisonnable de suggérer que l'émission du QW est principalement couplée aux QDs plutôt que d'être recombinée à l'interface. Ensuite, la variation de l'épaisseur de la couche de recouvrement en fonction de la température dans la plage de 10-300 K a été évaluée en tant que paramètre potentiel pouvant affecter l'efficacité du NRET. Il a été constaté que la couche de recouvrement la plus fine de 5 nm favorise le couplage NRET à longue distance le plus efficace lorsque la distance QW-QD devient 80 nm, quelle que soit la température. En outre, plus la couche de recouvrement est fine, plus la plage pour laquelle un couplage très efficace peut avoir lieu est longue. Compte tenu de tous ces éléments, le couplage électromagnétique en champ proche est un processus qui pourrait jouer un rôle important dans la conception de dispositifs hautement efficaces et compacts. Ainsi, nous pensons que cette étude fondamentale est un premier pas vers la compréhension du mécanisme NRET qui pourrait éventuellement être appliqué à un dispositif LED multicolore basé sur l'InGaN qui utilise des QDs pour la conversion de la lumière vers le bas.

Dans les chapitres II et III, nous avons étudié l'impact de l'orientation du dipôle et de la distance donneur-accepteur sur la NRET. Ici, l'accent est mis sur la capacité de la densité locale d'états optiques (LDOS) à permettre un contrôle plus substantiel du transfert d'énergie entre un milieu actif donneur et un milieu actif accepteur.

Selon la théorie classique de la NRET, le LDOS est d'une importance primordiale en tant que paramètre contrôlant le taux d'émission du donneur. Le LDOS caractérise l'environnement photonique en comptant le nombre de modes de photons disponibles pour l'émission. Pour ce faire, nous avons choisi d'étudier le transfert d'énergie entre des points quantiques (QDs) verts (donneurs) et rouges (accepteurs) et nous proposons d'utiliser des structures de cristaux photoniques (PC) comme moyen de contrôler le LDOS: un PC carré TiO_2 avec des trous, que nous remplissons ensuite d'une solution de QDs verts et rouges mélangés en quantités égales. La structure est décrite dans le schéma de la FIG. IV.1.

Cependant, prouver que le taux de NRET dépend ou non de la densité des modes photoniques locaux est un sujet difficile qui fait l'objet d'une discussion ouverte depuis de nombreuses années. Compte tenu de cette controverse, notre protocole vise une étude complète des interactions entre les QDs verts et rouges dans le cadre de la NRET en tenant compte des

éléments du PC. Par conséquent, il y a d'abord la possibilité d'une NRET entre les QDs qui se produit spontanément, même sans le PC. Nous envisagerons toutes les situations possibles qui peuvent avoir un impact différent sur le transfert d'énergie: une résonance (ou un LDOS élevé) dans le vert et un LDOS faible (ou pas de résonance) dans le rouge, un LDOS faible dans le vert et un LDOS élevé dans le rouge, un LDOS faible dans les deux gammes de longueurs d'onde et un LDOS élevé pour le rouge et le vert. Il est essentiel de comprendre comment l'amélioration ou l'inhibition de l'émission de PC dans le vert et/ou dans le rouge affecte le transfert d'énergie. Le but du protocole susmentionné est d'évaluer et d'extraire des conclusions sur l'interaction des modes photoniques avec l'émission des QDs donneurs et accepteurs.

La procédure pour obtenir la conception finale peut être divisée en deux parties principales: la fabrication du PC et le dépôt du mélange de QDs. En ce qui concerne le PC, sa réalisation comprenait les étapes suivantes d'un processus standard: dépôt de la couche de TiO_2 par pulvérisation, lithographie par faisceaux d'électrons (EBL) et gravure ionique réactive (RIE). La deuxième étape a consisté à appliquer par centrifugation la solution de QD sur le PC. L'ensemble du processus est décrit dans la FIG. IV.3. Avant le dépôt de TiO_2 sur un substrat SiO_2/Si, les échantillons ont été découpés en échantillons d'environ 2 cm2 puis nettoyés avec de l'eau DI. Nous avons utilisé la machine de pulvérisation magnétron AC450, en mode réactif à partir d'une cible de Ti. Les paramètres de dépôt du TiO_2 étaient les suivants: flux Ar/O_2 = 80/4 sccm, pression = $2x10^{-3}$ mbar, puissance RF = 370W, polarisation de la cible = 320 V à température ambiante. L'épaisseur obtenue était d'environ 90-95 nm après 45 minutes. La deuxième étape du processus de fabrication du PC a été l'EBL afin de modeler la résine (SEM Inspect F electron beam microscope de FEI, équipé d'un système d'écriture e-beam Elphy Plus de Raith). La préparation de l'échantillon comprenait le revêtement par centrifugation de la résine positive AR-P 6200.04 (4000 rpm, 3000 rpm/s pendant 60 s) et la post-cuisson pendant 60 s à 150 °C. L'épaisseur de la résine a été mesurée par photoréflectométrie à environ 90 nm, de manière uniforme sur l'ensemble de l'échantillon. La résine est ensuite développée afin de révéler les motifs exposés.

La troisième étape a consisté à transférer le motif sur le TiO_2 en utilisant la résine AR-P comme masque. Cette opération a été réalisée par gravure ionique réactive (Corial 200S). La recette suivante a été sélectionnée: 100 sccm CHF3, à une pression de 30 mT et une puissance de 140 W, pendant 500 s. Dans le cas des surfaces à nanopatterns, la valeur maximale de la profondeur de gravure sur TiO_2 que nous avons pu obtenir était de 60 nm, ce qui correspond à la situation où toute la couche de résine est déjà enlevée.

Les images SEM et AFM en vue de dessus montrent que les trous étaient circulaires, malgré la nature granuleuse du TiO_2. Alors que des diamètres de trous compris entre 90 et 340 nm ont pu être obtenus, les trous d'un diamètre inférieur à 130 nm et supérieur à 300 nm ne présentaient pas une forme régulière. Pour les diamètres inférieurs, les trous n'étaient pas complètement ouverts après la RIE (FIG. IV.4, première ligne) et pour les diamètres les plus élevés, les trous fusionnaient, formant des piliers. En outre, comme le montre la FIG. IV.5, les côtés des trous présentent une certaine inclinaison. En outre, tous les modèles présentent une profondeur de gravure de 60 nm, quel que soit le diamètre des trous.

La déposition du polymère contenant les QDs sur la surface dessinée s'est avérée être une procédure exigeante pour des raisons liées à l'épaisseur de la couche attendue. Tout d'abord, il est nécessaire de visualiser et de localiser les zones dessinées en dessous, afin de les caractériser. Deuxièmement, un film épais court-circuiterait complètement le couplage avec les modes PC, car une grande partie des QDs se trouverait en dehors de l'extension du mode vertical. Par conséquent, le revêtement doit être effectué de manière à obtenir une couche aussi fine et homogène que possible. Le spin coating a été effectué deux fois pour chaque échantillon et les paramètres de dépôt étaient les suivants: 1000 rpm, 2000 rpm/s pendant 10 s. Cependant, il faut noter ici que la solution de QD n'a pas été optimisée pour le dépôt par spin coating en termes de viscosité.

Dans l'ensemble, de nombreux motifs photoniques ont été simulés, construits et étudiés, mais pour les besoins de cette thèse, la discussion ne porte que sur les suivants: PC avec des périodes de 300 et 380 nm, et avec des diamètres fabriqués qui varient entre 90 et 215 nm. L'objectif de la série de motifs à petite période est l'amélioration du couplage entre le PC et le taux d'émission du QD donneur, et donc l'impact du LDOS sous la forme d'une résonance optique dans le vert. L'objectif de la deuxième série de motifs avec une période plus grande est l'amélioration du taux d'émission de l'accepteur. Cela signifie que sa bande de dispersion ne contient qu'une seule résonance optique dans le rouge. Afin de comparer les résultats du mélange de QD avec une référence, les mêmes motifs ont été étudiés, mais recouverts d'une fine pellicule ne contenant que des QD rouges.

La fabrication des motifs PC, bien qu'imparfaite, a conduit à des modes de lumière lente accordés avec l'émission rouge et verte des QDs en fonction des paramètres de conception. Pour chaque conception de PC-QD, nous avons effectué trois types de mesures optiques différentes: microréflectivité résolue en angle (ARμR), PL résolue en angle (ARPL) et PL résolue en temps (TRPL).

La microréflectivité et la PL résolue en angle (spectromètre microHR, Horiba et caméra CCD 1024×256 Syncerity) fournissent l'image de la lumière dans l'espace de Fourier. Dans ce schéma, le réseau à l'intérieur du spectrographe disperse le signal entrant le long de l'axe d'énergie. L'image obtenue par la caméra conduit au diagramme de dispersion du moment énergétique le long de ΓX: les courbes de dispersion sont révélées par les creux/pics de réflectivité ou de photo-luminescence. Nous avons utilisé une lampe halogène pour l'ARμR et un laser 405 nm pour l'ARPL.

Les résultats de l'ARPL pour le mélange sont présentés dans la FIG. IV.10 avec l'intensité intégrée à l'angle pour chaque longueur d'onde. Dans la FIG. IV.10.(b), nous pouvons voir que pour 180 et 190 nm de diamètre obtenu, les modes PC se couplent avec l'émission rouge des QDs et par conséquent nous obtenons une émission accrue dans le rouge. Dans la FIG. IV.10.(a), nous pouvons voir que pour un diamètre de 125 nm, alors que le LDOS (bande plate) est augmenté exactement à la position de la longueur d'onde d'émission du QD donneur (voir également la FIG. IV.9), l'intensité intégrée dans la gamme rouge autour de 630 nm augmente à près de 60000, par rapport aux valeurs inférieures à 40000 pour d'autres diamètres, et bien que la longueur d'onde d'émission du QD rouge ne soit pas accordée avec une résonance optique. Par conséquent, si nous observons une augmentation de l'émission dans le vert lorsque le LDOS est élevé dans le vert, ce qui est trivial, nous observons également une augmentation de l'émission dans le rouge, bien qu'aucune résonance optique ne soit observée dans cette gamme de longueurs d'onde. Ceci n'est pas possible si l'on ne considère que le couplage direct entre un QD et un mode. Cette observation tend donc à montrer qu'il existe un couplage énergétique entre le donneur et l'accepteur, favorisé par la LDOS élevée à la longueur d'onde du donneur. En ce qui concerne la deuxième série d'expériences avec seulement des QDs rouges déposés sur le même échantillon, comme prévu, il n'y a pas d'émission dans le vert puisqu'il n'y a pas de QDs verts. Sans surprise, l'émission intégrée dans le cas de p=380 nm et pour un diamètre de 180 nm où la résonance optique est exactement à la longueur d'onde désirée, l'émission rouge passe de 250000 à 400000. En revanche, nous n'avons pas d'amélioration spécifique lorsque le mode est dans le vert. Alors que l'émission rouge, seule ou mélangée avec des QDs verts, est augmentée de manière substantielle lorsqu'elle est accordée avec une résonance optique dans le rouge (avec un facteur entre 2 et 7), nous observons une augmentation de l'émission plus faible mais néanmoins clairement mesurable pour les QDs rouges mélangés avec des QDs verts accordés avec une résonance dans le vert. Cela tend à montrer que les QDs verts sont des médiateurs permettant une augmentation plus importante

de l'émission rouge. Et cela semble être le cas à la fois pour les résonances dans le rouge et dans le vert.

En analysant maintenant les courbes TRPL bi-exponentielles, nous remarquons un cas spécial pour p=300 nm et d=125 nm où le taux de désintégration est augmenté. Pour cette structure particulière, selon l'ARPL, le taux d'émission du donneur est maximisé. Par conséquent, lorsque le mode est accordé avec les QDs verts, nous observons une diminution de la durée de vie à la fois pour l'émission des QDs rouges et verts et pour les composantes radiatives et non radiatives. Par conséquent, pour l'émission verte, cela peut s'expliquer à la fois par un Purcell et éventuellement par une amélioration du NRET en raison de la LDOS élevée. En ce qui concerne l'émission rouge, bien qu'il n'y ait pas de mode à cette longueur d'onde, on observe une diminution de la durée de vie, qui suit la diminution de la durée de vie de l'émission verte, bien qu'aucun effet Purcell ne soit attendu à cette longueur d'onde. La raison de cette diminution de la durée de vie n'est pas encore claire à ce stade. Une observation similaire peut être faite dans le cas de la période de 380 nm, pour un diamètre de 215 nm. Dans le même sens, comme nous pouvons le voir dans la FIG.IV.13.(a) et (b), la TRPL montre une décroissance plus rapide dans l'émission verte et dans l'émission rouge. Cependant, pour une telle structure, les résonances de lumière lente sont accordées avec l'émission rouge. Une explication possible de ce comportement pourrait être liée à la présence de modes rapides accordés avec l'émission verte du QD, comme le montrent les mesures ARPL de la FIG. IV.10.(b). L'interaction des mêmes structures avec seulement des QDs rouges a ensuite été étudiée. La décroissance temporelle était à nouveau un ajustement bi-exponentiel avec deux contributions. Comme nous pouvons le voir dans la FIG. IV.14, puisqu'il n'y a pas de couplage, nous ne voyons que l'impact de l'accord de l'émission rouge avec les modes photoniques. Pour les modèles avec une période de 300 nm qui ont été fabriqués pour affecter le LDOS dans le vert, il n'y a pas d'impact du tout et donc, la durée de vie reste la même. D'autre part, dans la FIG. IV.14.(b), nous pouvons voir l'impact de la conception avec un diamètre de 180 nm, où l'émission rouge est accordée avec le LDOS comme une diminution de la durée de vie.

Il apparaît que ces configurations complexes incluent un grand nombre de paramètres à prendre en compte et que l'interprétation des résultats n'est donc pas évidente. Nous pouvons voir l'impact du renforcement de Purcell dans la contribution radiative, et nous avons obtenu une indication possible du couplage de transfert d'énergie QD-QD. Mais à ce stade, il n'est pas encore possible d'évaluer si le transfert non radiatif est bien représenté dans ce schéma d'interaction. Des expériences supplémentaires permettraient de mieux comprendre la situation. Dans notre cas, il n'a pas été possible d'inhiber complètement l'émission radiative dans le vert

afin d'évaluer l'existence d'un mécanisme de couplage supplémentaire, car nous avions toujours les contributions des modes rapides. Néanmoins, en vue de l'application, le PC est un outil puissant lorsqu'il s'agit de sélectionner la longueur d'onde pour le contrôle de l'émission. Une telle conception avantageuse pourrait permettre d'optimiser chaque pixel micro-LED séparément en améliorant ou/et en inhibant simultanément l'émission à des fréquences spécifiques en fonction des besoins d'affichage.

Dans le cinquième chapitre, nous étudions une autre façon d'accéder à l'impact de la densité locale d'états optiques (LDOS) sur le transfert d'énergie non radiatif (NRET). À cette fin, nous avons choisi d'étudier le couplage entre un réseau circulaire concentrique à puits quantiques multiples basé sur InGaN/GaN et des points quantiques rouges de CdSe (QDs). Le réflecteur circulaire de Bragg est composé d'une structure périodique multicouche InGaN/GaN-QD et la solution de QD devrait remplir le CG entièrement gravé. Comme le CG joue le rôle d'une nanocavité photonique chargée de contrôler le LDOS, l'objectif est ici d'étudier l'impact sur son couplage avec les QDs. Dans le cadre de cette étude, les structures CG ont été conçues pour affecter fortement l'émission du QW donneur (à 460 nm) ou des QDs accepteurs (à 630 nm), en supportant des modes résonnants aux longueurs d'onde respectives ou des bandes interdites photoniques (PBG).

À cette fin, des simulations FDTD (Finite-Difference Time-Domain) (le logiciel Lumerical a été utilisé à cette fin) ont été réalisées dans l'espace 3D. L'objectif était d'obtenir les paramètres géométriques (période, diamètre de la cavité) qui peuvent supporter un mode de cavité à 460 nm, à 630 nm de longueur d'onde et un mode de bord de bande (sans aucune résonance). Pour le confinement de la lumière, nous avons proposé un réseau circulaire de 14 périodes, ce qui représente un diamètre total de moins de 5 µm pour l'ensemble de la structure pour tous les modèles limités à une épaisseur de 110 nm correspondant à la propagation d'un mode unique dans la couche semi-conductrice. Les champs électromagnétiques simulés montrent que les modes sont localisés uniquement à la surface du défaut pour le plus petit diamètre de cavité dans le bleu. Les pertes peuvent être estimées par le QF, qui est d'environ 370.

Malheureusement, le processus de fabrication a présenté plusieurs limitations qu'il n'a pas été possible de surmonter pour le moment. Dans tous les cas, les conceptions existent et seraient une alternative intéressante car elles peuvent complètement inhiber l'émission radiative à la longueur d'onde du donneur qu'il était difficile d'étudier avec le PC et en même temps permettre à la NRET d'avoir lieu.

En conclusion générale, dans ce travail de thèse, nous avons abordé les propriétés photoniques du couplage en champ proche dans le cadre des applications LED. En nous basant sur la théorie du transfert d'énergie non radiatif, nous avons étudié les paramètres qui affectent cette interaction dipôle-dipôle, y compris l'orientation du dipôle et la polarisation de l'émission du donneur, la séparation donneur-accepteur et l'impact du LDOS sur l'émission du donneur et de l'accepteur. Une micro-LED basée sur le NRET pourrait conduire à une conception efficace et compacte appliquée à l'amélioration de l'efficacité de la conversion des couleurs dans le sens de la prise en compte des propriétés électriques et optiques du couplage QW-QD, ainsi que de l'interaction avec leur environnement photonique.